Bhattacharya *et al.*
Journal of Genetic Engineering and Biotechnology (2022) 20:43
https://doi.org/10.1186/s43141-022-00314-7

Journal of Genetic Engineering and Biotechnology

RESEARCH

Open Access

In silico discovery of 3 novel quercetin derivatives against papain-like protease, spike protein, and 3C-like protease of SARS-CoV-2

Kunal Bhattacharya[1*], Ripunjoy Bordoloi[1,2], Nongmaithem Randhoni Chanu[3], Ramen Kalita[1], Bhargab Jyoti Sahariah[1] and Atanu Bhattacharjee[4]

Abstract

Background: The derivatives of quercetin is known for their immune-modulating antiviral, anti-blood clotting, antioxidant, and also for its anti-inflammatory efficacy. The current study was therefore conducted to examine the noted novel derivatives of quercetin present in plant sources as an immune modulator and as an antiviral molecule in the COVID-19 disease and also to study their affinity of binding with potential three targets reported for coronavirus, i.e., papain-like protease, spike protein receptor-binding domain, and 3C-like protease.

Based on the high-positive drug-likeness score, the reported derivatives of quercetin obtained from an open-source database were further filtered. Compounds with positive and high drug-likeness scores were further predicted for their potential targets using DIGEP-Pred software, and STRING was used to evaluate the interaction between modulated proteins. The associated pathways were recorded based on the Kyoto Encyclopedia of Genes and Genomes pathway database. Docking was performed finally using PyRx having AutoDock Vina to identify the efficacy of binding between quercetin derivatives with papain-like protease, spike protein receptor-binding domain, and 3C-like protease. The ligand that scored minimum binding energy was chosen to visualize the interaction between protein and ligand. Normal mode analysis in internal coordinates was done with normal mode analysis to evaluate the physical movement and stability of the best protein-ligand complexes using the iMODS server.

Results: Forty bioactive compounds with the highest positive drug-likeness scores were identified. These 40 bioactives were responsible for regulating different pathways associated with antiviral activity and modulation of immunity. Finally, three lead molecules were identified based on the molecular docking and dynamics simulation studies with the highest anti-COVID-19 and immunomodulatory potentials. Standard antiviral drug remdesivir on docking showed a binding affinity of − 5.8 kcal/mol with PLpro, − 6.4 kcal/mol with 3CLpro, and − 8.6 kcal/mol with spike protein receptor-binding domain of SARS-CoV-2, the discovered hit molecules quercetin 3-O-arabinoside 7-O-rhamnoside showed binding affinity of − 8.2 kcal/mol with PLpro, whereas quercetin 3-[rhamnosyl-(1- > 2)-alpha-L-arabinopyranoside] and quercetin-3-neohesperidoside-7-rhamnoside was predicted to have a binding affinity of − 8.5 kcal/mol and − 8.8 kcal/mol with spike protein receptor-binding domain and 3CLpro respectively

Conclusion: Docking study revealed quercetin 3-O-arabinoside 7-O-rhamnoside to possess the highest binding affinity with papain-like protease, quercetin 3-[rhamnosyl-(1- > 2)-alpha-L-arabinopyranoside] with spike protein receptor-binding domain, and quercetin-3-neohesperidoside-7-rhamnoside with 3C-like protease and all the protein-ligand complexes were found to be stable after performing the normal mode analysis of the complexes in internal coordinates.

*Correspondence: kunal22101994@gmail.com
[1] NETES Institute of Pharmaceutical Science, Mirza, Guwahati, Assam 781125, India
Full list of author information is available at the end of the article

Keywords: 3CLpro, PLpro, Spike protein, Quercetin derivatives, SARS-CoV-2

Graphical Abstract

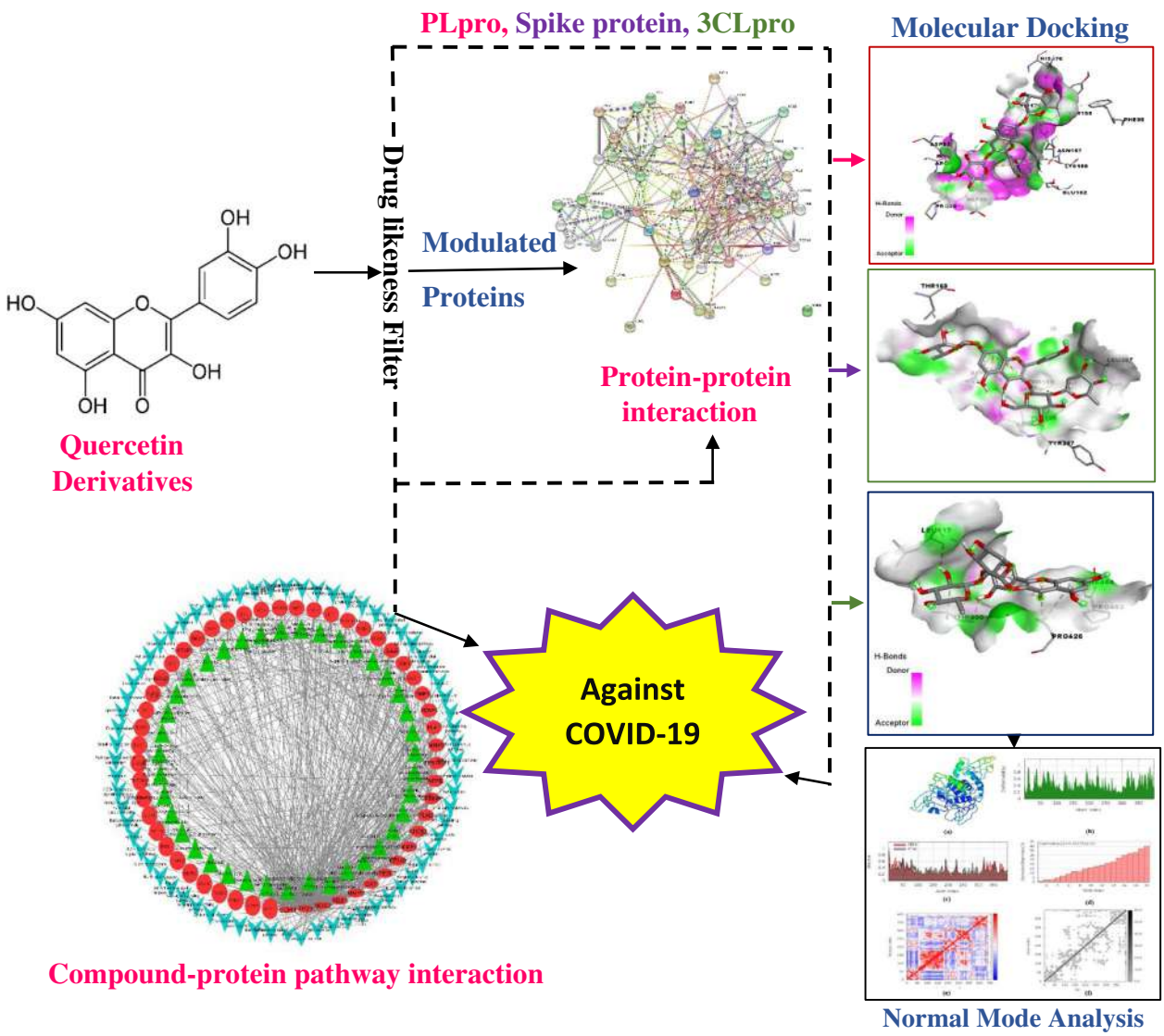

Background

Starting from 2019 December, now COVID-19 infection caused by the SARS-CoV-2 virus has been the reason for millions of deaths worldwide [1]. People already suffering from different non-infectious and infectious diseases and populations falling under geriatrics and pediatrics having low immunity are at higher risk of getting infected with SARS-CoV-2 induced COVID-19 disease [2]. Different methods such as social distancing and hygiene maintenance, are enforced to tackle the spread of COVID-19; boosting people's immunity could be of great importance in preventing the spread of the SARS-CoV-2 virus its entry into the body. Although several vaccines have been developed limitations in the manufacturing capacities and distributions capacities, the required herd immunity seems to be a distant mirage. Also, the genetic mutations occurring in the SARS-CoV-2 virus put vaccines' effectiveness at high risk. To meet the urgent need for a therapeutic agent effective over a broad spectrum of COVID-19 infections, alternate natural source-based anti-covid molecules will be important in fighting COVID-19 disease worldwide. Three potential targets of novel coronaviruses, i.e., papain-like protease (PLpro), spike protein receptor-binding domain, and 3C-like

protease (3CLpro) [3–6], are being targeted in search of new lead molecules by the majority of researchers for COVID-19 management. Necrosis of cells and inflammation further worsen the pathogenesis involved in COVID-19, which suggests molecule identification has antiviral, antioxidant, antiviral, immune-modulatory, and anti-inflammatory properties. During the course of its replication, SARS-CoV-2, like all viruses, accumulates mutations—alterations in its genetic code—that make it more dangerous. It is possible that this virus contains built-in RNA repair mechanisms, and as a result, it accumulates mutations at a slower rate than the majority of other RNA viruses. It is estimated that a virus genome from an infection collected in October 2020 has approximately 20 mutations in comparison to the first strain sequenced in January 2020 (Wuhan-Hu-1) [7]. Currently, as of 10th January 2022, as per WHO, four international variants of concern are Beta (B.1.351), first detected in South Africa, Gamma (P.1) first detected in Brazil, Delta (B.1.617.2), first detected in India and Omicron (B.1.1.529) first detected in South Africa and Botswana. The impact on severity was found to be increased in Beta, Gamma, and Delta than the initial variant of SARS-CoV-2 while the impact of Omicron is still unclear [8, 9].

Quercetin derivatives are a group of flavonoids obtained from plants [10]. Quercetin derivatives are chosen particularly for the study because there is substantial evidence in the literature confirming the antiviral activities of quercetin, which has been demonstrated in both in vitro and in vivo tests. In cultured cells, quercetin has been shown to suppress numerous respiratory viruses [11, 12]. Several rhinovirus and echovirus serotypes (types 7, 11, 12, and 19), coxsackievirus (types A21 and B1), and poliovirus (type 1 Sabin) serotypes are inhibited by this compound [13]. Quercetin also has anti-infective and anti-replicative capabilities against RNA and DNA viruses [respiratory syncytial virus (RSV), Polio type 1, parainfluenza type 3, and Herpes simplex virus-1 (HSV-1)] and has been shown to drastically inhibit plaque formation by these viruses [14]. HeLa cells inoculated with cytomegalovirus (CMV) are inhibited in their replication by this compound [15]. Dengue virus type 2 (DENV-2) replication in Vero cells is suppressed by quercetin at an IC50 of 35.7 g/mL, resulting in a 67% drop in DENV-2 RNA levels in the cells. This is due to quercetin's capacity to either prevent virus entry or suppress replicative enzymes like viral polymerases, which are responsible for virus replication [16]. Quercetin appears to protect mice infected with the meningoencephalitis virus from contracting a deadly illness, according to in vivo research [17]. A positive effect of quercetin administration was also shown in immunocompetent mice infected with the Mengo virus, where it was found to reduce the severity of the organ damage [18]. Athletes who take quercetin supplements are less likely to get an upper respiratory tract infection as a result of stress [19]. Therefore, in COVID-19 disease, it may be fruitful bioactive under investigation, which is identified with antiviral, antioxidant, and anti-inflammatory properties, which can be demonstrated using network pharmacology. Hence, based on the immunity-boosting/anti-inflammatory/anti-viral/antioxidant reports. With the help of in silico molecular docking and various system biology tools, we attempted to evaluate the antiviral efficacy of several derivatives of quercetin.

Materials and methods

Bioactive compounds with their drug-likeness score

From the Chemical Entities of Biological Interest (ChEBI) database (https://www.ebi.ac.uk/chebi/).and available records of literature, the phytoconstituents reported under the quercetin phytochemistry were retrieved. For drug-likeness score prediction, all the compounds were screened in MolSoft (https://molsoft.com/mprop/) by querying the SMILES of each molecule.

Immunity boosting efficacy assessment by target prediction and enrichment analysis

Upregulated and downregulated "protein-based targets" were identified using DIGEP-Pred [20] by querying high-positive drug-likeness scoring derivatives of quercetin at a probable activity of 0.5. The regulated proteins list obtained was further queried using STRING [21]. The probable modulated pathways were also identified using the Kyoto Encyclopedia of Genes and Genomes database. Further, Cytoscape version 3.8.2 was used for network construction between the bioactives, their potential targets, and modulated pathways [22]. To prevent false hit appearance, the elimination of the duplicate interconnection between two nodes was done, and also the entire network was analyzed further using the "network analyzer" tool [23].

Probable antiviral activity prediction

By keeping pharmacological activity (Pa) > Pharmacological inactivity (Pi), SMILES of each bioactive compound were queried in Prediction of Activity Spectra for Substances using the keyword "antiviral" to get the probable biological spectrum and to predict the antiviral activity of each compound [24]. Further, the records were also queried to identify the possible pharmacological spectrum against different viruses like influenza, herpes, adenovirus, trachoma, hepatitis B, rhinovirus, hepatitis C, cytomegalovirus (CMV), human immunodeficiency virus (HIV) and picornavirus.

In silico molecular docking

Ligand molecules preparation

From the database of PubChem (https://pubchem.ncbi.nlm.nih.gov/) ligands in 3D. sdf format with high positive drug-likeness scores was retrieved, or ChemSketch (https://www.acdlabs.com/resources/freeware/chemsketch/) was used to draw the structures of compounds as applicable. Using Discovery Studio, 2021 [25], all the ligands in .sdf format were converted into .pdb format. UFF was used as a forcefield for energy minimization of the bioactives [26]. After energy minimization, the conversion of all the ligand molecules into. pdbqt format was done.

Protein macromolecules preparation

Three potential target proteins of SARS-CoV-2, i.e., PLpro (PDB: 4M0W), spike protein receptor-binding domain (PDB: 6LZG), and 3CLpro (PDB: 6LU7), were selected. Using Discovery studio, 2021, heteroatoms present in the complex with proteins retrieved from Research Collaboratory for Structural Bioinformatics database were removed, and further, the proteins were saved in .pdb format.

Ligand-protein docking

Docking was performed between ligand and protein molecules using PyRx having AutoDock vina Plugin [27]. The grid box center values for 4M0W receptor were kept as X:8.6090, Y: 14.6186, and Z: 18.8131, whereas the dimension values in angstrom were X:77.8939, Y:70.8430, Z:25.0000. The grid box center values for 6LU7 receptor were kept as X: -22.9001, Y:14.5229, Z:58.9679, whereas the dimension values in angstrom were X:61.9565, 71.9321, and Z: 25.0000.

The grid box center values for 6LZG receptor were kept as X: -25.7988, Y:18.5947, Z: -25.4521, whereas the dimension values in angstrom were X: 69.3549, Y: 81.5506, and Z:25.0000. By keeping the exhaustiveness value at eight, dockings were performed in order to achieve 9 different ligand molecule poses. After completing docking, the ligand pose gave the minimum binding energy, the value of which was further selected for visualizing the interaction between ligand and protein using Discovery studio 2021 [28, 29].

Normal mode analysis in internal coordinates

Normal mode analysis in internal coordinates was carried out for the best ligands among the selected molecules. From the analysis of docking results, it was declared that quercetin 3-O-arabinoside 7-O-rhamnoside was the best ligand for papain-like protease, quercetin 3-[rhamnosyl-(1- > 2)-alpha-L-arabinopyranoside] was the best ligand for spike protein receptor-binding domain, and quercetin-3-neohesperidoside-7-rhamnoside was the best ligand for 3C-like protease. The normal mode analysis for all three protein-ligand complexes was carried out using iMODS server (http://imods.chaconlab.org/). It is a very effective, rapid, and user-friendly tool that can be used for the structural investigation of protein-ligand complexes. The analysis provides deformity values, eigenvalues, B-factor, elastic network details, variance, and covariance map. For a protein-ligand complex, the deformity depends upon the ability to deform at each of its amino acid residues. The energy that is required to deform the structure is understood by eigenvalue, which also represents the motion stiffness of the protein-ligand complex [30, 31].

Results

Bioactive compounds and their drug-likeness score

Among 134 quercetin derivatives, 40 bioactives with high drug-likeness scores were identified. Among them, Calabricoside B scored the highest drug-likeness score, i.e., 1.17 with molecular weight 904.23, 23 hydrogen bond acceptor, 13 hydrogen bond donors, and − 1.27 MolLogP. Druglikeness score details of individual compounds are summarized in Table 1.

Target prediction and their enrichment analysis to assess immune-boosting efficacy

Among all the compounds having a high-positive drug-likeness score, it was predicted that quercetin 3,7-di-O-α-L-rhamnoside modulates the maximum number of genes, i.e., 10. Also, Cadherin-1 (CDH-1) was targeted by the maximum number of bioactive compounds, i.e., 30. Further, 61 different pathways were identified by enrichment analysis in which cancer pathways were majorly modulated via 22 genes (KEAP1, HMOX1, RBX1, MMP2, SKP1, TRAF2, RARA, VHL, APC, MDM2, ITGAV, CDH1, AXIN1, CREBBP, EP300 EPAS1, LEF1, NOS2, CTNNB1, CASP8, AR, NFE2L2) under the background of 517 proteins at the false discovery rate of 7.71E−17. Modulated gene set's enrichment analysis with its modulated pathway and individual gene codes is summarized in Table 2. The protein-protein interaction of the modulated proteins is given in Fig. 1. The combined bioactive-proteins-pathways is given in Fig. 2. which also reflected the quercetin 3,7-di-O-α-L-rhamnoside to target the maximum number of proteins. The dot plot for KEGG Pathway analysis is given in Fig. 3

Possible antiviral activity prediction

The quercetin derivatives were found to have antiviral potential against influenza, herpes, hepatitis, hepatitis

Table 1 Druglikeness of quercetin derivatives with high positive score

Bioactives	Molecular formula	Molecular weight	NHBA	NHBD	MolLogP	MolPSA (A^2)	MolVol (A^3)	DLS
Quercetin 3,7-di-*O*-α-L-rhamnoside	$C_{27}H_{30}O_{15}$	594.16	15	9	− 1.13	195.34	531.93	0.78
Quercetin 3-*O*-rhamnoside-7-*O*-glucoside	$C_{27}H_{30}O_{16}$	610.15	16	10	− 1.99	212.65	539.15	0.78
Quercetin 3-*O*-[β-D-xylosyl-(1→2)-β-D-glucoside]	$C_{26}H_{28}O_{16}$	596.14	16	10	− 1.61	214.98	518.37	0.90
Quercetin 7-*O*-β-L-rhamnopyranoside	$C_{21}H_{20}O_{11}$	448.10	11	7	− 0.26	147.54	406.18	0.83
Quercetin 3-*O*-β-L-fucopyranoside	$C_{21}H_{20}O_{11}$	448.10	11	7	0.32	150.41	407.46	0.82
Quercetin 3-*O*-β-D-glucopyranosyl-7-*O*-α-L-rhamnopyranoside	$C_{27}H_{30}O_{16}$	610.15	16	10	− 1.99	212.65	539.15	0.78
Quercetin 3-*O*-α-(6‴-caffeoylglucosyl-β-1,2-rhamnoside)	$C_{36}H_{36}O_{19}$	772.19	19	11	0.98	250.40	699.90	0.90
Quercetin 3-(6″-*p*-hydroxybenzoylgalactoside)	$C_{28}H_{24}O_{14}$	584.12	14	8	1.40	189.07	524.25	0.83
Quercetin 3-*O*-(2″,3″-digalloyl)-β-D-galactopyranoside	$C_{35}H_{28}O_{20}$	768.12	20	12	1.00	273.40	680.77	1.01
Quercetin 3-*O*-β-D-glucopyranosyl-(1→2)-rhamnopyranoside	$C_{27}H_{30}O_{16}$	610.15	16	10	− 1.15	214.15	533.87	0.88
Quercetin 3-*O*-α-L-[6‴-*p*-coumaroyl-β-D-glucopyranosyl-(1→2)-rhamnopyranoside]	$C_{36}H_{36}O_{18}$	756.19	18	10	1.36	234.92	687.18	0.89
Quercetin 3-*O*-α-L-rhamnopyranosyl-(1→2)-α-L-arabinopyranoside	$C_{26}H_{26}O_{15}$	580.14	15	9	− 0.92	197.67	511.15	1.05
Quercitrin	$C_{21}H_{20}O_{11}$	448.10	11	7	0.32	150.41	407.46	0.82
Quercetin 3-*O*-α-L-[6‴-*p*-coumaroyl-β-D-glucopyranosyl-(1→2)-rhamnopyranoside]-7-*O*-β-D-glucopyranoside	$C_{42}H_{46}O_{23}$	918.24	23	13	− 0.95	297.16	818.87	0.79
Multinoside A	$C_{27}H_{30}O_{16}$	610.15	16	10	− 1.09	214.15	533.87	0.88
Rutin	$C_{27}H_{30}O_{16}$	610.15	16	10	− 1.55	213.63	533.42	0.91
Camellianoside	$C_{32}H_{38}O_{20}$	742.20	20	12	− 2.91	260.89	637.11	1.07
Hermannioside A	$C_{32}H_{38}O_{19}$	726.20	19	11	− 2.37	242.60	635.62	1.01
Quercetin 3′-isobutyrate	$C_{19}H_{16}O_{8}$	372.08	8	4	2.03	106.80	361.56	1.06
Quercetin 3-(2-galloylglucoside)	$C_{28}H_{24}O_{16}$	616.11	16	10	0.29	220.56	547.73	0.97
Quercetin 3-glucoside 7-xyloside	$C_{26}H_{28}O_{16}$	596.14	16	10	− 2.32	213.47	523.65	0.80
Quercetin 3-lathyroside	$C_{26}H_{28}O_{16}$	596.14	16	10	− 1.61	214.98	518.37	0.90
Quercetin 3-(6″-acetylglucoside)	$C_{23}H_{22}O_{13}$	506.11	13	7	0.08	171.83	460.42	0.80
Quercetin 3-(6″-malonylneohesperidoside)	$C_{30}H_{32}O_{19}$	696.15	19	10	− 1.42	245.96	608.70	0.86
Quercetin 3-(2-caffeoylsophoroside) 7-glucoside	$C_{42}H_{46}O_{25}$	950.23	25	15	− 2.54	330.48	838.90	0.87
Quercetin 3-O-arabinoside 7-O-rhamnoside	$C_{26}H_{28}O_{15}$	580.14	15	9	− 1.46	196.16	516.43	0.95
Quercetin 3-(3″,6″-diacetylgalactoside)	$C_{25}H_{24}O_{14}$	548.12	14	6	0.68	176.47	506.25	1.03
Quercetin 3-(2‴-p-coumarylsambubioside)-7-glucoside	$C_{41}H_{44}O_{23}$	904.23	23	13	− 1.91	298.51	803.46	1.02
Quercetin 3-[rhamnosyl-(1- > 2)-alpha-L-arabino-pyranoside]	$C_{26}H_{28}O_{15}$	580.14	15	9	− 0.92	197.67	511.15	1.05
Quercetin-7-*O*-[α-L-rhamnopyranosyl(1→6)-β-D-galactopyranoside]	$C_{27}H_{30}O_{16}$	610.15	16	10	− 2.13	210.76	532.15	0.92
Taxifolin	$C_{15}H_{12}O_{7}$	304.06	7	5	0.76	103.49	268.73	1.00
5-galloylquercetin-3-*O*-α-L-arabinofuranoside	$C_{27}H_{22}O_{14}$	570.10	14	9	0.79	198.07	516.59	0.86
Petiolaroside	$C_{27}H_{30}O_{16}$	610.15	16	10	− 1.99	212.65	539.15	0.78
2-(3,4-dihydroxybenzoyloxy)-4,6-dihydroxybenzoic acid	$C_{14}H_{10}O_{8}$	306.04	8	5	1.07	116.37	268.60	1.07
Calabricoside A	$C_{32}H_{38}O_{20}$	742.20	20	12	− 3.23	259.91	642.84	1.00
Calabricoside B	$C_{41}H_{44}O_{23}$	904.23	23	13	− 1.27	296.68	808.96	1.17
Cudranian 2	$C_{28}H_{26}O_{13}$	570.14	13	9	0.74	181.22	516.03	1.06
Quercetin-3′-glucuronide	$C_{21}H_{20}O_{13}$	480.09	13	8	− 0.86	177.94	405.92	1.00
Quercetin-3-*O*-arabinoside	$C_{20}H_{18}O_{11}$	434.08	11	7	− 0.01	151.23	391.96	0.93
Quercetin-3-neohesperidoside-7-rhamnoside	$C_{33}H_{40}O_{20}$	756.21	20	12	− 2.60	259.09	658.34	0.84

DLS druglikeness score, *NHBA* number of hydrogen bond acceptor, *NHBD* number of hydrogen bond donor

Table 2 Enrichment analysis of modulated proteins by the reported quercetin derivatives

Term ID	Term description	Observed gene count	Back-gene count	False discovery rate	Matching proteins in the network
hsa05200	Pathways in cancer	22	517	7.71E−17	KEAP1,HMOX1,RBX1,MMP2,SKP1,TRAF2,RARA,VHL,APC,MDM2,ITGAV,CDH1,AXIN1,CREBBP,EP300,EPAS1,LEF1,NOS2,CTNNB1,CASP8,AR,NFE2L2
hsa04310	Wnt signalling pathway	11	154	5.78E−10	RBX1,TBL1X,SKP1,APC,MMP7,AIN1,CREBBP,EP300,FBXW11,LEF CTNNB1
hsa05215	Prostate cancer	9	96	4.52E−09	PLAT,MDM2,CREBBP,EP300,LEF1,MP3,CTNNB1,PLAU,AR
hsa05132	Salmonella infection	10	209	1.28E−07	TNFRSF1A,RIPK3,TNFRSF10A,SKP1,TNFSF10,TRAF2,RIPK1,LEF1,CTNNB1,CASP8
hsa04066	HIF-1 signaling pathway	8	106	1.83E−07	HMOX1,RBX1,TIMP1,SERPINE1,VHL,CREBBP,EP300,NOS2
hsa05418	Fluid shear stress and atherosclerosis	8	130	6.93E−07	TNFRSF1A,KEAP1,HMOX1,MP2,PLAT,ITGAV,CTNNB1,NFE L2
hsa04120	Ubiquitin mediated proteolysis	8	135	7.86E−07	KEAP1,CDC34,RBX1,SKP1,VHL,MDM2,CUL3,FBXW11
hsa04390	Hippo signaling pathway	8	153	1.74E−06	SERPINE1,APC,CDH1,AXIN1,FBXW11,LEF1,CTNNB1,TP73
hsa05165	Human papillomavirus infection	10	325	3.28E−06	TNFRSF1A,VTN,APC,MDM2,ITGAV,AXIN1,CREBBP,EP300,CTNNB1,CASP8
hsa04520	Adherens junction	6	67	4.16E−06	VCL,CDH1,CREBBP,EP300,LEF1,CTNNB1
hsa04115	p53 signaling pathway	6	72	5.65E−06	TNFRSF10A,SERPINE1,MDM2,CASP8,TP73,CHEK1
hsa05170	Human immunodeficiency virus 1 infection	8	204	9.71E−06	TNFRSF1A,RBX1,SKP1,TRAF2,RIPK1,FBXW11,CASP8,CHEK1
hsa05131	Shigellosis	8	218	1.46E−05	TNFRSF1A,VCL,RBX1,SKP1,TRAF2,MDM2,RIPK1,FBXW11
hsa04217	Necroptosis	7	149	1.54E−05	TNFRSF1A,RIPK3,TNFRSF10A,TNFSF10,TRAF2,RIPK1,CASP8
hsa05206	MicroRNAs in cancer	7	160	2.28E−05	SIRT1,HMOX1,APC,MDM2,CREBBP,EP300,PLAU
hsa05225	Hepatocellular carcinoma	7	160	2.28E−05	KEAP1,HMOX1,APC,AXIN1,LEF1,CTNNB1,NFE2L2
hsa05213	Endometrial cancer	5	57	3.41E−05	APC,CDH1,AXIN1,LEF1,CTNNB1
hsa04668	TNF signaling pathway	6	112	4.03E−05	TNFRSF1A,RIPK3,TRAF2,RIPK1,MMP3,CASP8
hsa05167	Kaposi sarcoma-associated herpesvirus infection	7	187	4.90E−05	TNFRSF1A,TRAF2,CREBBP,EP300,LEF1,CTNNB1,CASP8
hsa04110	Cell cycle	6	120	5.32E−05	RBX1,SKP1,MDM2,CREBBP,EP300,CHEK1
hsa05211	Renal cell carcinoma	5	66	5.43E−05	RBX1,VHL,CREBBP,EP300,EPAS1
hsa04068	FoxO signaling pathway	6	127	6.62E−05	SIRT1,CAT,TNFSF10,MDM2,CREBBP,EP300
hsa04210	Apoptosis	6	132	7.84E−05	TNFRSF1A,TNFRSF10A,TNFSF10,TRAF2,RIPK1,CASP8
hsa05163	Human cytomegalovirus infection	7	218	0.0001	TNFRSF1A,TRAF2,MDM2,RIPK1,ITGAV,CTNNB1,CASP8
hsa05010	Alzheimer disease	8	355	0.00025	TNFRSF1A,LRP1,TRAF2,APC,AXIN1,NOS2,CTNNB1,CASP8
hsa05152	Tuberculosis	6	168	0.00025	TNFRSF1A,CREBBP,EP300,NOS2,CASP8,VDR
hsa05164	Influenza A	6	165	0.00025	TNFRSF1A,TNFRSF10A,TNFSF10,CREBBP,EP300,CASP8
hsa05203	Viral carcinogenesis	6	182	0.00038	TRAF2,MDM2,CREBBP,EP300,CASP8,CHEK1
hsa05130	Pathogenic Escherichia coli infection	6	187	0.00042	TNFRSF1A,TNFRSF10A,TNFSF10,TRAF2,RIPK1,CASP8
hsa05205	Proteoglycans in cancer	6	196	0.00053	MMP2,VTN,MDM2,ITGAV,CTNNB1,PLAU

Table 2 (continued)

Term ID	Term description	Observed gene count	Back-gene count	False discovery rate	Matching proteins in the network
hsa04919	Thyroid hormone signaling pathway	5	119	0.00056	MDM2,ITGAV,CREBBP,EP300,CTNNB1
hsa04114	Oocyte meiosis	5	120	0.00057	RBX1,SKP1,FBXW11,PGR,AR
hsa05217	Basal cell carcinoma	4	62	0.00068	APC,AXIN1,LEF1,CTNNB1
hsa04371	Apelin signaling pathway	5	131	0.0008	PLAT,SERPINE1,CDH1,PPARGC1A,NOS2
hsa05224	Breast cancer	5	145	0.0012	APC,AXIN1,LEF1,PGR,CTNNB1
hsa05226	Gastric cancer	5	144	0.0012	APC,CDH1,AXIN1,LEF1,CTNNB1
hsa04218	Cellular senescence	5	150	0.0014	SIRT1,SERPINE1,MDM2,FBXW11,CHEK1
hsa04610	Complement and coagulation cascades	4	82	0.0016	PLAT,SERPINE1,VTN,PLAU
hsa04710	Circadian rhythm	3	30	0.0016	RBX1,SKP1,FBXW11
hsa05160	Hepatitis C	5	156	0.0016	TNFRSF1A,TRAF2,RIPK1,CTNNB1,CASP8
hsa05210	Colorectal cancer	4	82	0.0016	APC,AXIN1,LEF1,CTNNB1
hsa04350	TGF-beta signaling pathway	4	91	0.0022	RBX1,SKP1,CREBBP,EP300
hsa05202	Transcriptional misregulation in cancer	5	171	0.0022	PLAT,RARA,MDM2,MMP3,PLAU
hsa04916	Melanogenesis	4	95	0.0024	CREBBP,EP300,LEF1,CTNNB1
hsa05216	Thyroid cancer	3	36	0.0024	CDH1,LEF1,CTNNB1
hsa05142	Chagas disease	4	99	0.0027	TNFRSF1A,SERPINE1,NOS2,CASP8
hsa04064	NF-kappa B signaling pathway	4	101	0.0029	TNFRSF1A,TRAF2,RIPK1,PLAU
hsa04922	Glucagon signaling pathway	4	101	0.0029	SIRT1,CREBBP,EP300,PPARGC1A
hsa05016	Huntington disease	6	298	0.0030	TRAF2,CREBBP,EP300,PPARGC1A,CASP8,GPX1
hsa05219	Bladder cancer	3	41	0.0030	MMP2,MDM2,CDH1
hsa05166	Human T-cell leukemia virus 1 infection	5	211	0.0046	TNFRSF1A,MMP7,CREBBP,EP300,CHEK1
hsa04934	Cushing syndrome	4	153	0.0118	APC,AXIN1,LEF1,CTNNB1
hsa04920	Adipocytokine signaling pathway	3	69	0.0119	TNFRSF1A,TRAF2,PPARGC1A
hsa04622	RIG-I-like receptor signaling pathway	3	70	0.0122	TRAF2,RIPK1,CASP8
hsa05100	Bacterial invasion of epithelial cells	3	70	0.0122	VCL,CDH1,CTNNB1
hsa04141	Protein processing in endoplasmic reticulum	4	165	0.0144	RBX1,SKP1,TRAF2,NFE2L2
hsa05412	Arrhythmogenic right ventricular cardiomyopathy	3	76	0.0145	ITGAV,LEF1,CTNNB1
hsa04621	NOD-like receptor signaling pathway	4	174	0.0168	RIPK3,TRAF2,RIPK1,CASP8
hsa04211	Longevity regulating pathway	3	87	0.0203	SIRT1,CAT,PPARGC1A
hsa04657	IL-17 signaling pathway	3	92	0.0233	TRAF2,MMP3,CASP8
hsa05169	Epstein-Barr virus infection	4	193	0.0233	TRAF2,MDM2,RIPK1,CASP8
hsa05222	Small cell lung cancer	3	92	0.0233	TRAF2,ITGAV,NOS2
hsa04510	Focal adhesion	4	198	0.0244	VCL,VTN,ITGAV,CTNNB1
hsa04061	Viral protein interaction with cytokine and cytokine receptor	3	96	0.0245	TNFRSF1A,TNFRSF10A,TNFSF10
hsa04215	Apoptosis - multiple species	2	30	0.0300	TNFRSF1A,CASP8
hsa05145	Toxoplasmosis	3	105	0.0304	TNFRSF1A,NOS2,CASP8
hsa05014	Amyotrophic lateral sclerosis	5	352	0.0316	TNFRSF1A,CAT,TRAF2,NOS2,GPX1
hsa04670	Leukocyte transendothelial migration	3	109	0.0326	VCL,MMP2,CTNNB1

B, hepatitis C, rhinovirus, HIV, CMV, trachoma, and picornavirus. Among them, the maximum number of the compounds were active against herpes virus and hepatitis B virus, i.e., 100%. The overall activity of bioactive compounds against different viruses is given in Fig. 4.

In silico molecular docking

Quercetin 3-O-arabinoside 7-O-rhamnoside was speculated to have the maximum binding affinity (-8.2 kcal/mol) with PLpro with 9 hydrogen bond interactions via LYS27B, GLN41B, ARG42B, ARG72B, ARG74B, ASN157A,

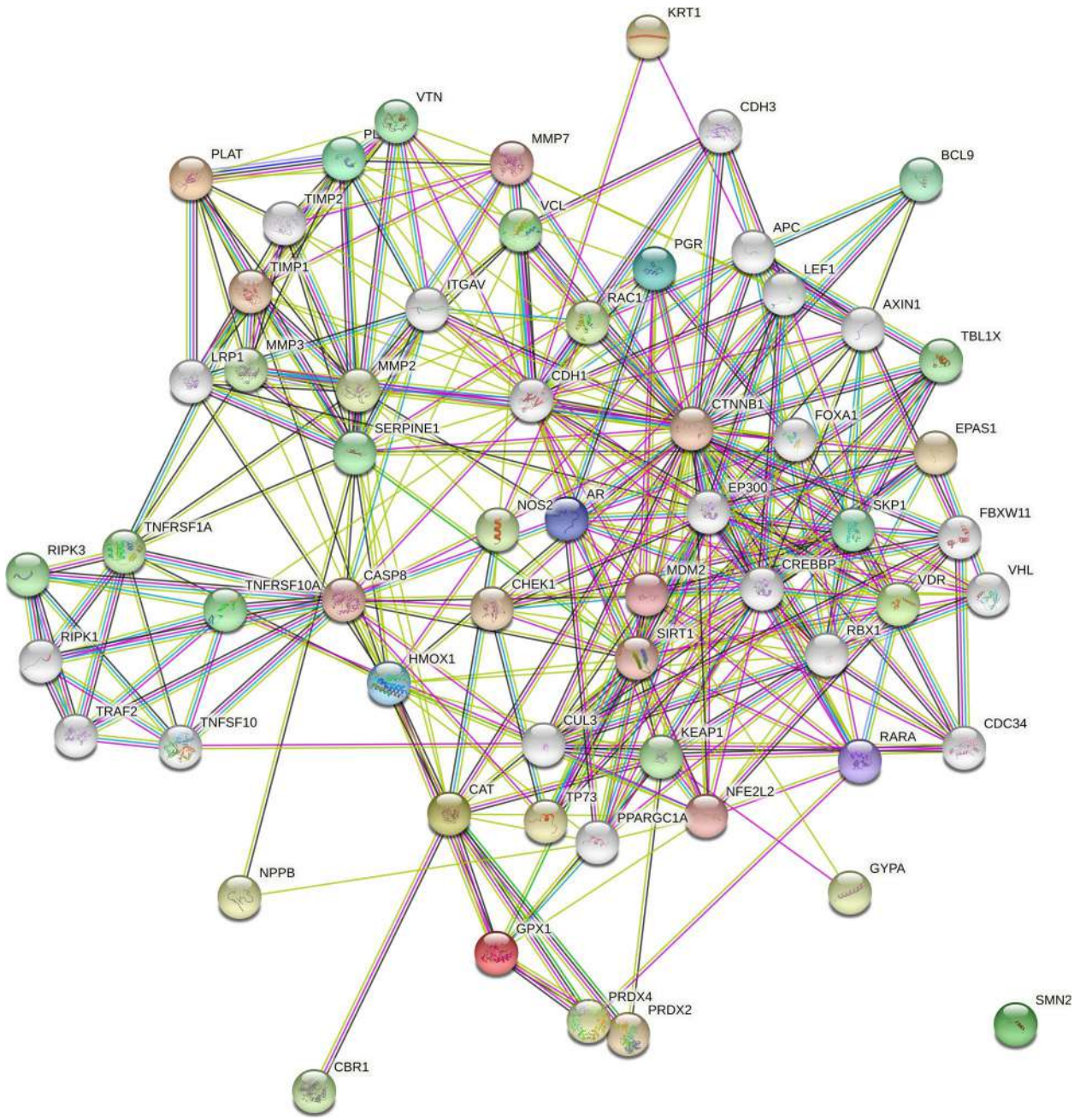

Fig. 1 Protein-protein interaction of regulated proteins

LYS158A, GLU162A, and HIS176A. The interaction details obtained using PLIP (https://plip-tool.biotec.tu-dresden.de/plip-web/plip/index) [32] are summarized in Table 3. Quercetin 3-[rhamnosyl-(1- > 2)-alpha-L-arabinopyranoside] was speculated in possessing maximum binding affinity (− 8.5 kcal/mol) with spike protein receptor-binding domain with 7 hydrogen bond interaction via ALA348A, TYR385A, ASN394, GLU398A, ARG514A. The interaction details obtained using PLIP (https://plip-tool.biotec.tu-dresden.de/plip-web/plip/index) [32] are summarized in Table 4. Quercetin-3-neohesperidoside-7-rhamnoside was predicted to possess maximum binding affinity (− 8.8 kcal/mol) with 3CLpro with 10 hydrogen bond interactions via ASN133A, THR169A, ALA194A,

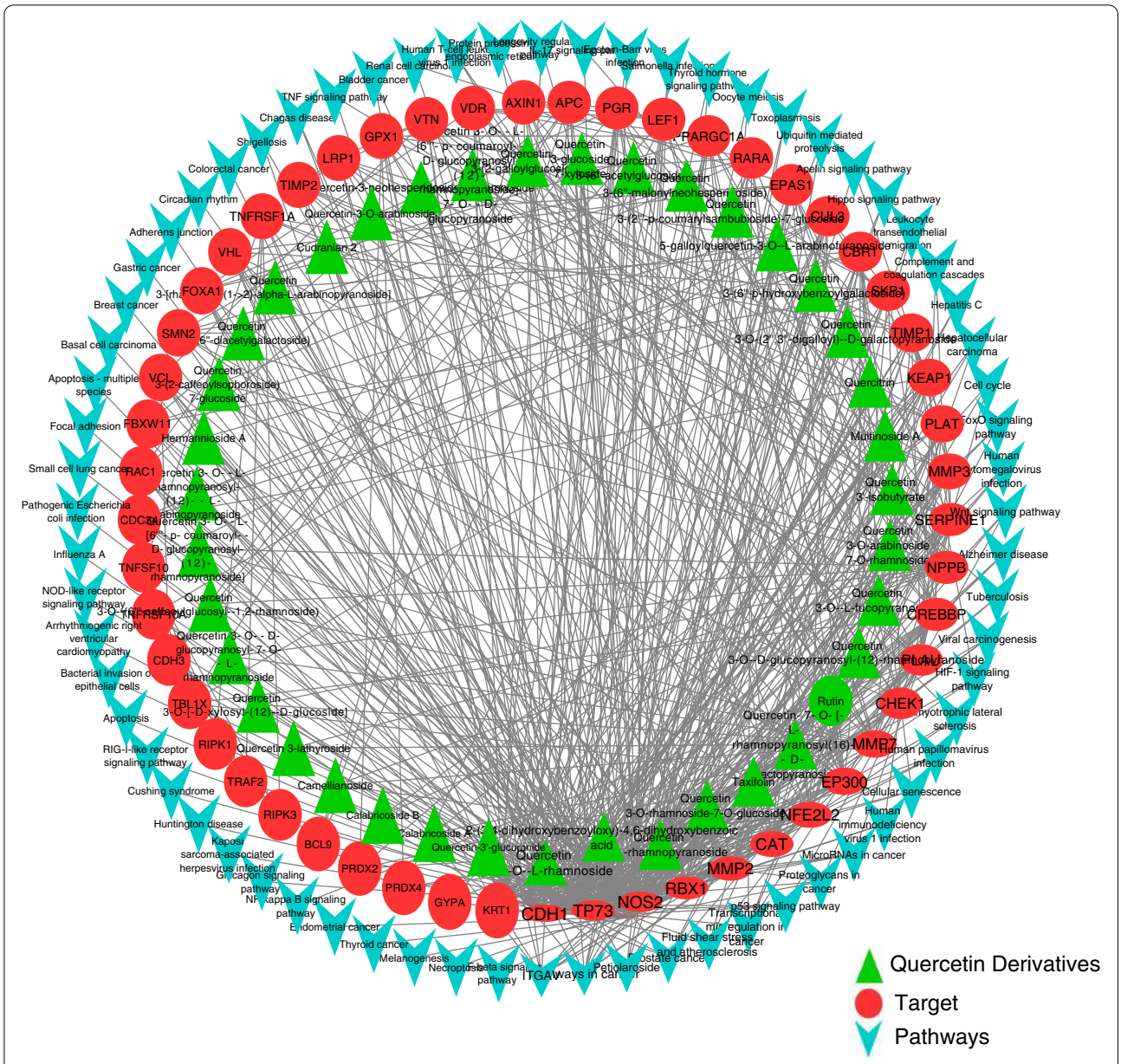

Fig. 2 Network interaction of quercetin derivatives with their proteins and regulated pathways

ASP197A, THR199A, ASN238A, and LEU287A. The interaction details obtained using PLIP (https://plip-tool.biotec.tu-dresden.de/plip-web/plip/index) [32] are summarized in Table 5. The interaction of quercetin 3-O-arabinoside 7-O-rhamnoside with PLpro, quercetin 3-[rhamnosyl-(1- > 2)-alpha-L-arabinopyranoside] with spike protein receptor-binding domain, and quercetin-3-neohesperidoside-7-rhamnoside with 3CLpro is shown in Fig. 5. Remdesivir as a standard antiviral drug showed a binding affinity of − 5.8 kcal/mol with PLpro, − 6.4 kcal/mol with 3CLpro, and − 8.6 kcal/mol with spike protein receptor-binding domain of SARS-CoV-2. 2D results of amino acid residues of protein-ligand interactions showed that remdesivir interacted with LYS A:307, GLU A:308, THR A:258, and LEU A:260 of PLpro, LEU A:272, LEU A:287, ASP A:289, ARG A:131 and TYR A:237 of 3CLpro and LEU A:73, LEU A:100, ALA A:99, ALA A:396, ASP A:206, LYS A:562, GLU A:564, GLU A:208, GLY A:205, and GLN A:98 of spike protein receptor-binding domain of SARS-CoV-2 (Fig. 6).

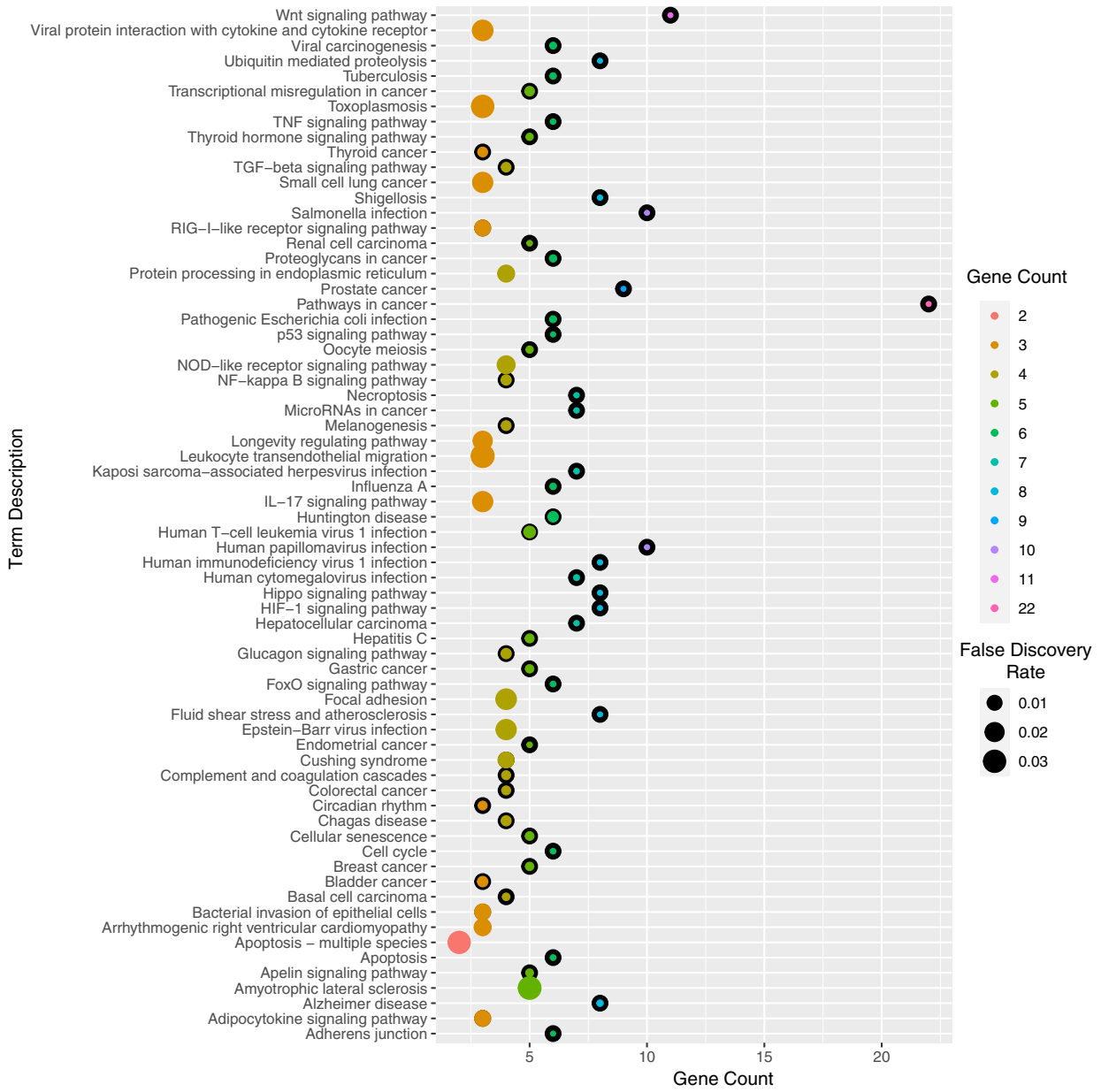

Fig. 3 Dot Plot of KEGG pathway enrichment analysis

Normal mode analysis in internal coordinates

Normal mode analysis in internal coordinates was performed using iMODS server to evaluate the movements of protein-ligand complexes. The NMA mobility of all the protein-ligand complexes is shown in Figs. 7a, 8a, and 9a. The main chain deformity is shown in Figs. 7b, 8b, and 9b, which shows hinges indicating high deformability regions. The B-factor values calculated by normal mode analysis are given in Figs. 7c, 8c, and 9c. Quantification of the uncertainty of each atom is calculated by B-factor values. Figures 7d, 8d, and 9d represent the eigenvalues of the complexes, which are a measure of the energy required for structure deformation. The lower the eigenvalue, the easier is the deformation. Eigenvalue for quercetin 3-O-arabinoside 7-O-rhamnoside and papain-like protease complex is 6.492351e−05. Eigenvalue for quercetin 3-[rhamnosyl-(1- > 2)-alpha-L-arabinopyranoside] and spike protein receptor-binding domain complex is 2.605057e−05 and the eigenvalue of quercetin-3-neohesperidoside-7-rhamnoside and 3C-like protease

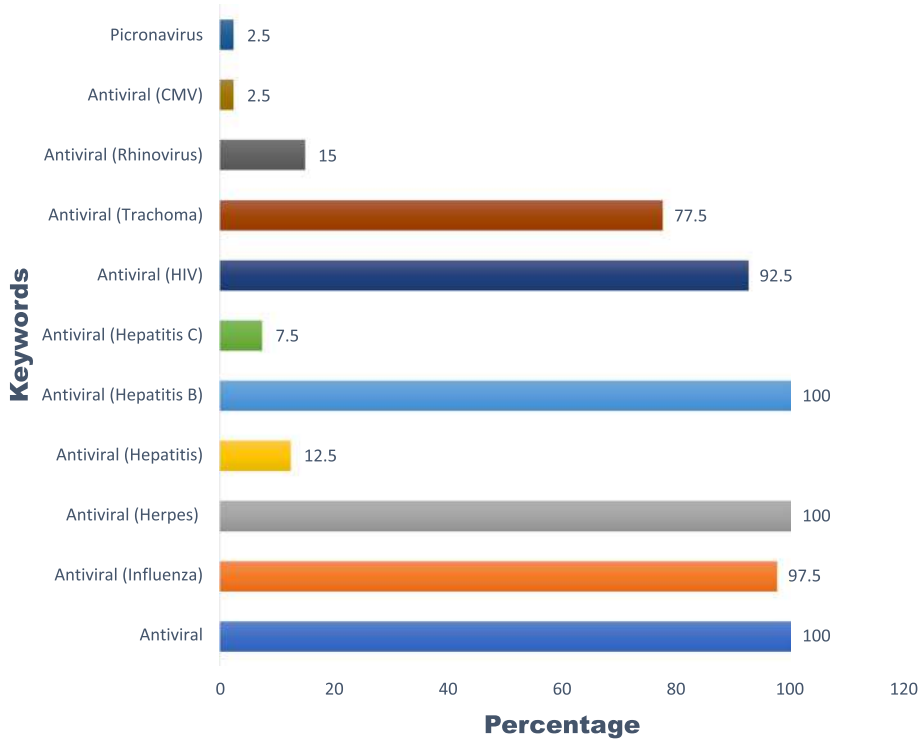

Fig. 4 Predicted antiviral activity of quercetin derivatives against multiple viruses

Table 3 Interactions of quercetin 3-O-arabinoside 7-O-rhamnoside with papain-like protease

Hydrogen bonds							
Index	Residue	AA	Distance H-A	Distance D-A	Donor angle	Donor atom	Acceptor atom
1	27B	LYS	2.12	2.80	122.17	3928 [O3]	3532 [O2]
2	41B	GLN	3.45	3.93	112.72	3551 [Ng+]	3928 [O3]
3	42B	ARG	2.27	2.90	119.01	3852 [Ng+]	3915 [O3]
4	72B	ARG	3.37	3.79	107.06	3878 [Ng+]	3915 [O3]
5	74B	ARG	3.26	4.01	131.04	1521 [Nam]	3938 [O3]
6	157A	ASN	2.43	2.86	104.85	1534 [N3+]	3917 [O3]
7	158A	LYS	2.04	2.94	145.30	1568 [O3]	3915 [O3]
8	162A	GLU	2.09	2.70	121.02	1568 [O3]	3915 [O3]
9	176A	HIS	2.10	3.06	154.95	1726 [Npl]	3944 [O3]
Hydrophobic interactions							
Index	Residue	AA	Distance	Ligand Atom	Protein atom		
1	157A	ASN	3.92	3907	1519		
Salt bridges							
Index	Residue	AA	Distance	Ligand Group	Ligand atoms		
1	27B	LYS	5.23	Carboxylate	3921,3926		
2	42B	ARG	4.09	Carboxylate	3919,3921		
3	42B	ARG	4.86	Carboxylate	3921,3926		
4	172A	HIS	4.56	Carboxylate	3898,3944		

Table 4 Interactions of quercetin 3-[rhamnosyl-(1- > 2)-alpha-L-arabinopyranoside] with spike protein receptor-binding domain

Hydrogen bonds							
Index	Residue	AA	Distance H-A	Distance D-A	Donor angle	Donor atom	Acceptor atom
1	348A	ALA	2.66	3.55	150.52	2678 [Nam]	6459 [O3]
2	385A	TYR	2.11	2.70	119.95	6461 [O3]	2987 [O3]
3	394A	ASN	2.62	3.40	136.26	3058 [Nam]	6415 [O3]
4	398A	GLU	1.81	2.76	163.63	6453 [O3]	3080 [O2]
5	398A	GLU	2.33	3.01	126.77	6451 [O3]	3080 [O2]
6	514A	ARG	2.35	3.19	145.13	6455 [O3]	4037 [Ng+]
7	514A	ARG	2.79	3.55	134.11	4040 [Ng+]	6453 [O3]
Salt bridges							
Index	Residue	AA	Distance	Ligand group	Ligand atoms		
1	401A	HIS	5.25	Carboxylate	6443,6451		

Table 5 Interactions of quercetin-3-neohesperidoside-7-rhamnoside with 3C-like protease

Hydrogen bonds							
Index	Residue	AA	Distance H-A	Distance D-A	Donor angle	Donor atom	Acceptor atom
1	133A	ASN	2.53	3.41	149.00	1031 [Nam]	2432 [O3]
2	169A	THR	2.36	2.99	121.92	2430 [O3]	1311 [O3]
3	194A	ALA	3.28	3.68	106.41	1492 [Nam]	2428 [O3]
4	194A	ALA	2.21	2.77	115.85	2428 [O3]	1495 [O2]
5	197A	ASP	2.71	3.33	121.36	1508 [Nam]	2418 [O3]
6	197A	ASP	3.58	4.09	115.72	2432 [O3]	1515 [O-]
7	199A	THR	2.65	3.24	119.32	2399 [O3]	1529 [O3]
8	199A	THR	2.32	3.05	131.84	1529 [O3]	2387 [O3]
9	238A	ASN	3.11	4.09	172.34	1852 [Nam]	2386 [O3]
10	287A	LEU	2.29	3.26	166.57	2206 [Nam]	2395 [O3]
Hydrophobic interactions							
Index	Residue	AA	Distance	Ligand atom	Protein atom		
1	197A	ASP	3.41	2378	1512		
2	287A	LEU	3.70	2392	2210		
Salt bridges							
Index	Residue	AA	Distance	Ligand group	Ligand atoms		
1	137A	LYS	5.44	Carboxylate	2369,2370		

complex is 1.066618e−04. The covariance map, shown in Figs. 7e, 8e, and 9e, shows the coupling between pairs of residues. Correlated motion is represented in red, uncorrelated motion is represented in white, and anti-correlated motion is given in blue color. The elastic network of the structures, shown in Figs. 7f, 8f, and 9f, defines the pair of atoms connected by springs where each dot in the graph represents one spring between the corresponding pair of atoms. Darker grays indicate stiffer springs.

Structural features of discovered bioactive compounds

Quercetin 3-O-arabinoside 7-O-rhamnoside is chemically 2-(3,4-dihydroxyphenyl)-5-hydroxy-7-[(3R,4R,5R,6S)-3,4,5-trihydroxy-6-methyloxan-2-yl]oxy-3-[(3R,4S,5S)-3,4,5-trihydroxyoxan-2-yl]oxychromen-4-one. It is a quercetin O-glycoside, a trihydroxyflavone and a disaccharide derivative. It has a molecular weight of 580.14, XLogP3-AA value of − 0.9. The hydrogen bond donor count is 9, whereas the hydrogen bond acceptor count is 15. The rotatable bond count is 5, and the topological polar surface area is 245 $Å^2$ (Fig. 10a).

Quercetin-3-neohesperidoside-7-rhamnoside is chemically 3-[(2*S*,3*R*,4*S*,5*S*,6*R*)-4,5-dihydroxy-6-(hydroxymethyl)-3-[(2*S*,3*R*,4*R*,5*R*,6*S*)-3,4,5-trihydroxy-6-methyloxan-2-yl]oxyoxan-2-yl]oxy-2-(3,4-dihydroxyphenyl)-5-hydroxy-7-[(2*S*,3*R*,4*R*,5*R*,6*S*)-3,4,5-trihydroxy-6-methyloxan-2-yl]oxychromen-4-one. It is a member of flavonoids and a

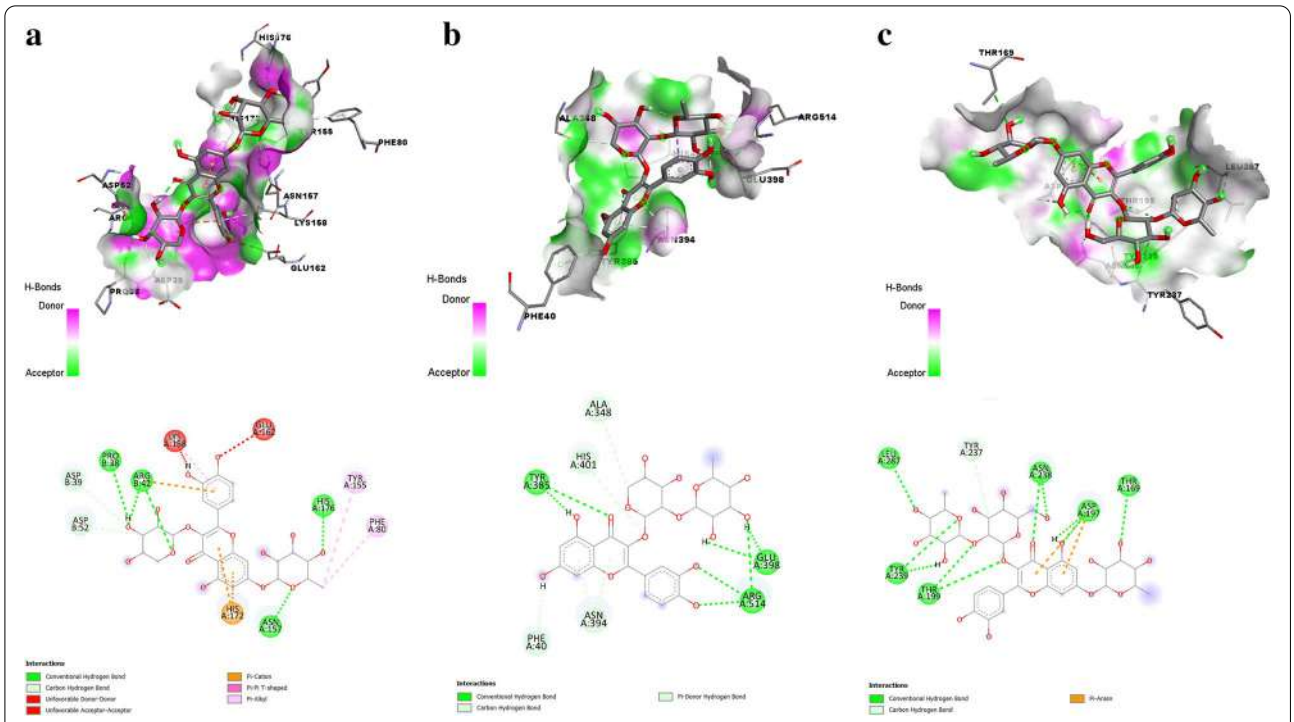

Fig. 5 Interaction of **a** Quercetin 3-O-arabinoside 7-O-rhamnoside with papain-like protease. **b** Quercetin 3-[rhamnosyl-(1- > 2)-alpha-L-arabinopyranoside] with spike protein receptor binding domain. **c** Quercetin-3-neohesperidoside-7-rhamnoside with 3C-like protease

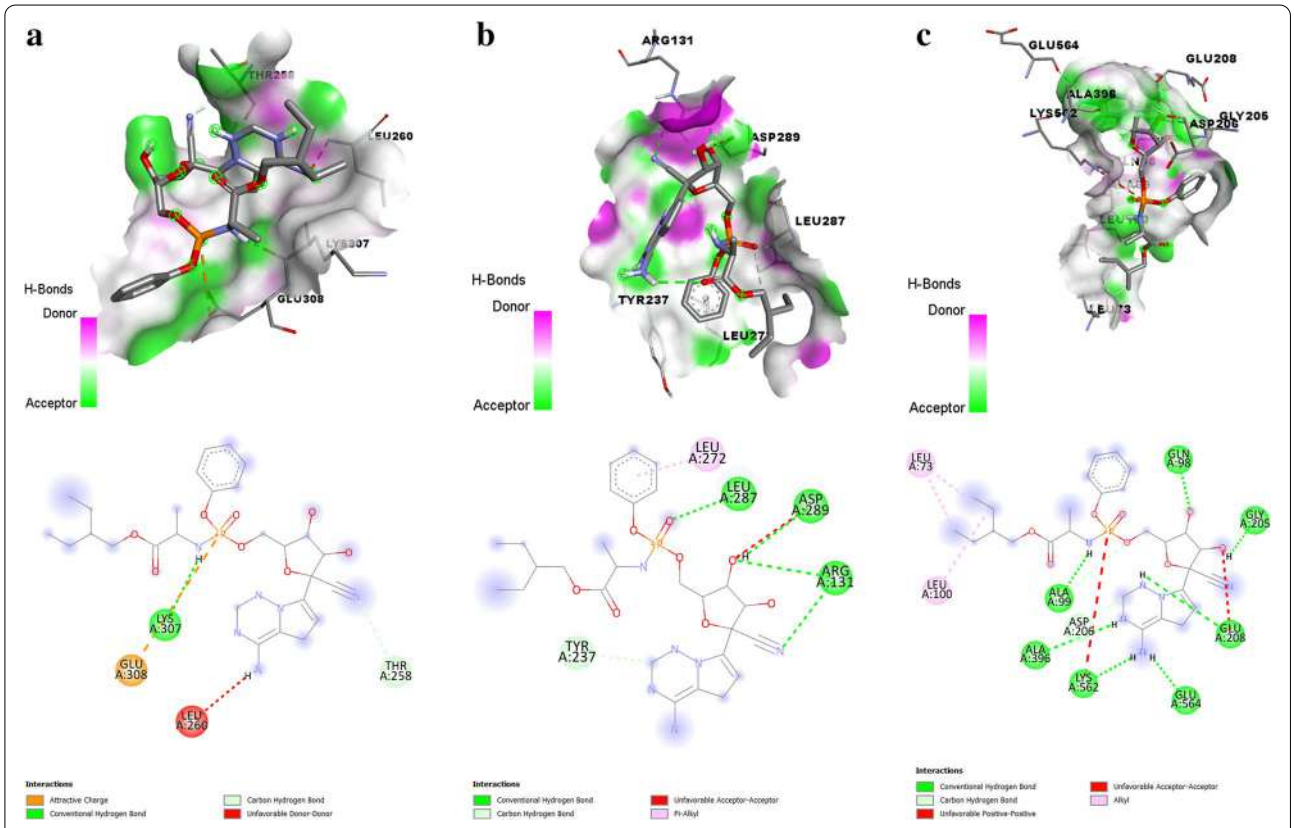

Fig. 6 Interaction of **a** Remdesivir with PLpro. **b** Remdesivir with 3CLpro. **c** Remdesivir with spike protein receptor binding domain

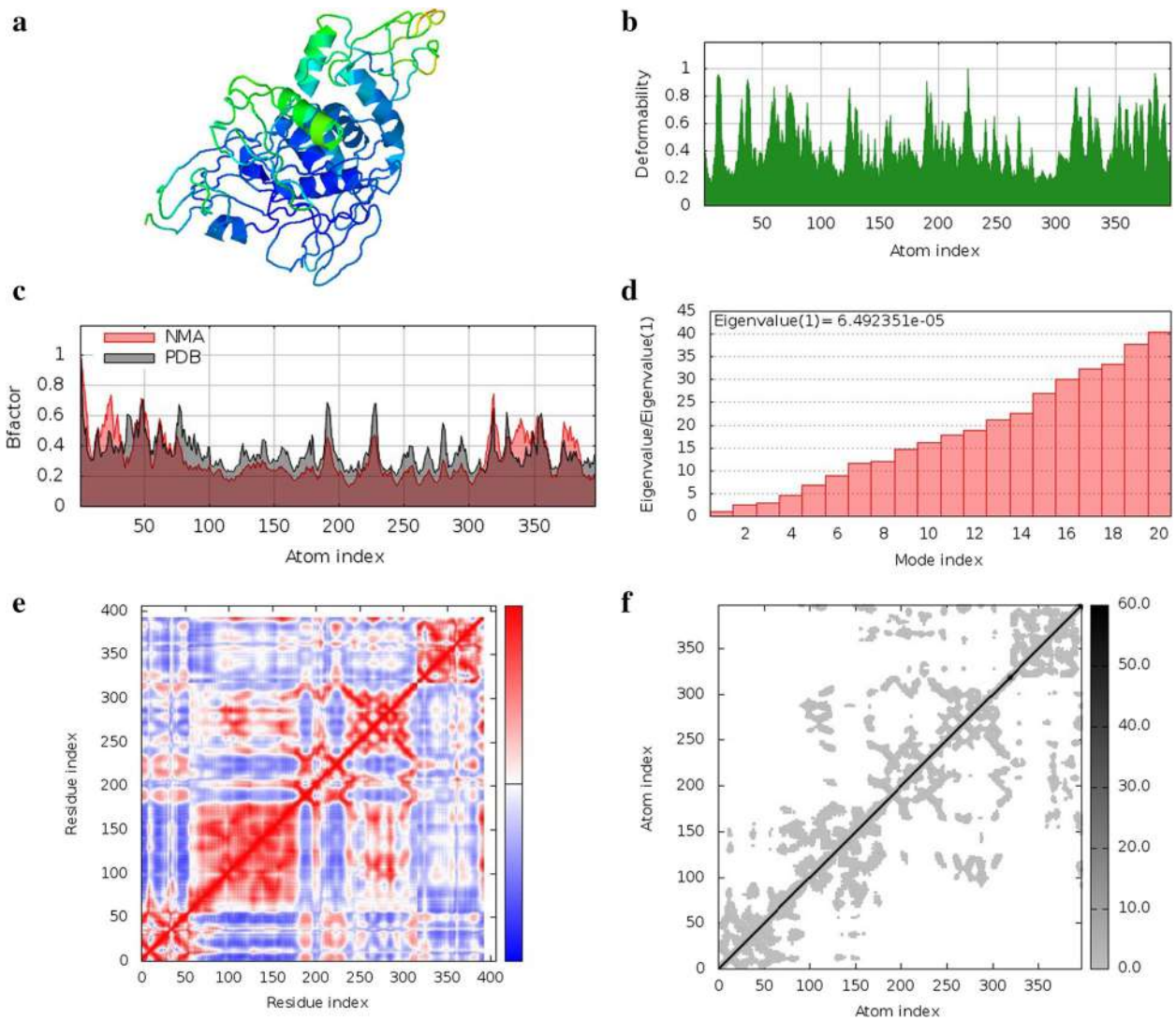

Fig. 7 Normal mode analysis of quercetin 3-O-arabinoside 7-O-rhamnoside and papain-like protease complex **a** NMA mobility, **b** deformity, **c** B-factor, **d** eigenvalues, **e** covariance map, **f** elastic network of complex

glycoside having a molecular weight of 756.21, XLogP3-AA value of − 2. The hydrogen bond donor count is 12 whereas the hydrogen bond acceptor count is 20. The rotatable bond count is 8 and topological polar surface area is 324 $Å^2$ (Fig. 10b).

Quercetin 3-[rhamnosyl-(1- > 2)-alpha-L-arabinopyranoside] is chemically 2-(3,4-dihydroxyphenyl)-3-[4,5-dihydroxy-3-(3,4,5-trihydroxy-6-methyloxan-2-yl) oxyoxan-2-yl]oxy-5,7-dihydroxychromen-4-one. It is a member of flavonoids and a glycoside having a molecular weight of 580.14, XLogP3-AA value of − 0.7. The hydrogen bond donor count is 9, whereas the hydrogen bond acceptor count is 15. The rotatable bond count is 5, and the topological polar surface area is 245 $Å^2$ (Fig. 10c).

Discussion

When it comes to SARS-CoV-2 structural proteins, the spike or S-protein is the most well-known, as it is the one responsible for the virus's attachment to the host cell. The S2 domain is responsible for viral fusion with the membrane of the host cell [33, 34]. The correct functioning of S protein will be disrupted if its attachment to the ACE2 receptor is prevented, its fusion function is inhibited, and the proteases responsible for its cleavage are inhibited [33]. 3CLpro is a coronavirus nonstructural protein. This enzyme cleaves viral polyproteins, resulting in the production of proteins necessary for virus replication and maturation. 3CLpro inhibition limits virus replication, making this protease

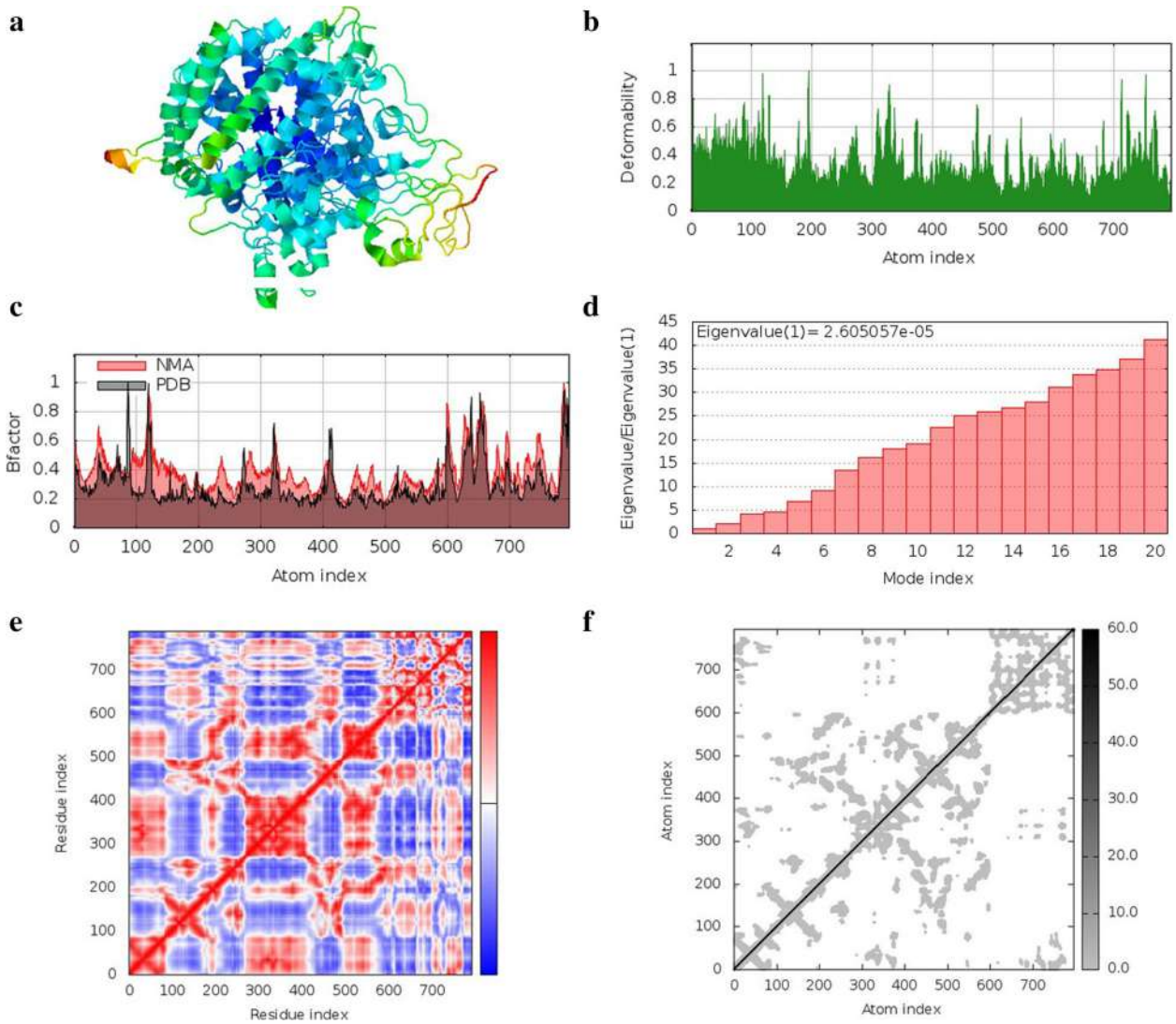

Fig. 8 Normal mode analysis of quercetin 3-[rhamnosyl-(1- > 2)-alpha-L-arabinopyranoside] and spike protein receptor binding domain complex **a** NMA mobility, **b** deformity, **c** B-factor, **d** eigenvalues, **e** covariance map, **f** elastic network of complex

a suitable therapeutic target [35]. PLpro can affect the innate immune response by cleaving ubiquitin and interferon-stimulated gene 15 (ISG15), recognized regulators of host innate immunity pathways, in addition to its protease action. Inhibition of this protease prevents viral replication [36].

Humayun et al. found different marine natural compounds to have a strong binding affinity for neuropilin-1 receptor of SARS-CoV-2. The molecular dynamics simulations also suggested the formation of stable complexes between the novel hits from natural marine compounds and neuropilin-1 receptor [37].

Ghosh et al. found that epigallocatechin-3-gallate (EGCG), epicatechin-gallate, and gallocatechin-3-gallate have strong binding affinity for Mpro and can hydrogen bond with one or both of its catalytic residues (His41 and Cys 145) in their investigation. In comparison to the unligated enzyme, produced complexes were more stable and less prone to conformational changes, as indicated by molecular dynamics (MD) simulations [38].

Herbacetin, rhoifolin, and pectolinarin are flavanoids that have previously been proven to be potent inhibitors of SARS-CoV Mpro. The IC50 values of the compounds were measured using a FRET-based assay and were 33.17, 27.45, and 37.78 M, respectively. They were projected to bind to the primary viral protease's active site [39]. H herbacetin, pectolinarin, and baicalin were identified to block SARS-CoV-2 Mpro proteolytic activity [40].

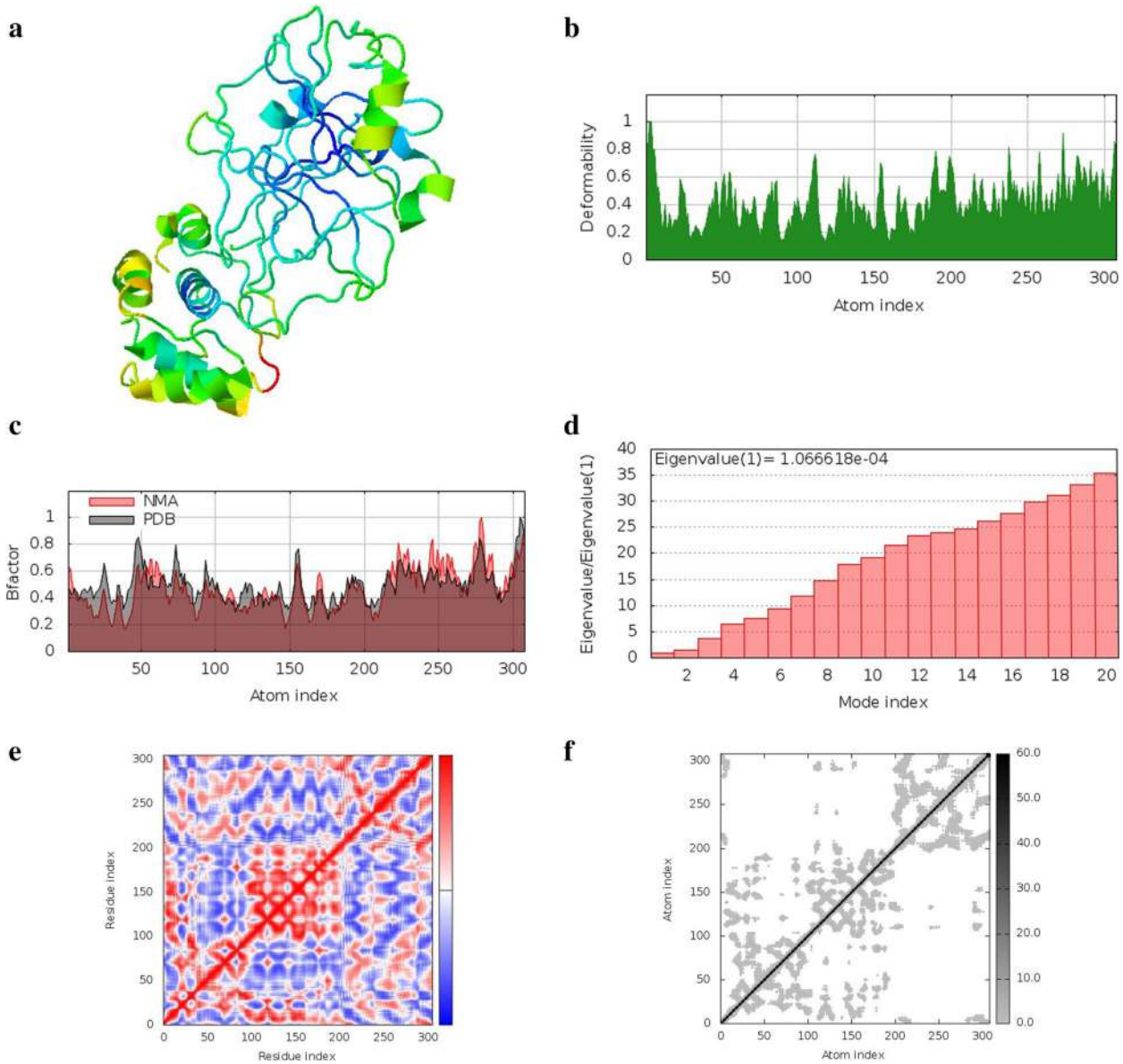

Fig. 9 Normal mode analysis of quercetin-3-neohesperidoside-7-rhamnoside and 3C-like protease complex **a** NMA mobility, **b** deformity, **c** B-factor, **d** eigenvalues, **e** co-variance map, **f** elastic network of complex

Another promising natural medication against SARS-CoV-2 was discovered to be tannic acid. Mpro and the host cell protease TMPRSS2 are both inhibited by this polyphenol, which functions as a dual inhibitor. Tannic acid showed binding to Mpro with a dissociation constant of 1.1 M and TMPRSS2 with a dissociation constant of 1.77 M using surface plasmon resonance (SPR) [41].

In a recent in silico molecular docking research [38], EGCG, the major polyphenol in green tea, was identified as a possible inhibitor of SARS-CoV-2 Mpro [38].

The recent COVID-19 pandemic that caused severe necrosis and inflammation inside a host's body resulted in malfunctioning of supply of oxygen along with necessary nutrients into the host's cells, proving to be a severe complication with subjects having compromised immunity. Therefore, in this current study, an effort was carried out to investigate the efficacy of quercetin derivatives against potential COVID-19 targets, i.e., papain-like protease, spike protein receptor-binding domain, and 3C-like protease with their combined immune modulation activity. Initially, the calculation of the drug-likeness score of individual molecules was done based on "Lipinski's rule of five" [42] because most of the drugs of plant origin are utilized via the

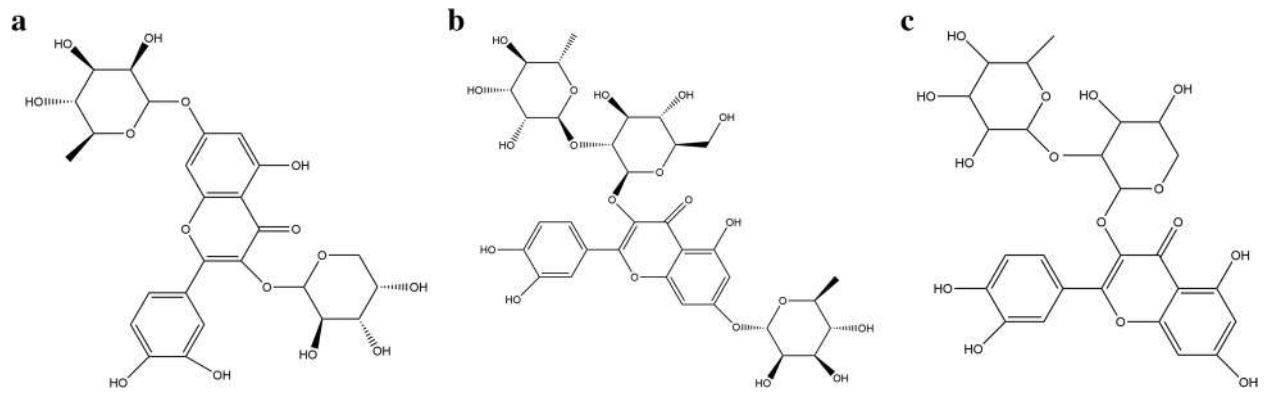

Fig. 10 **a** Chemical structure of quercetin 3-O-arabinoside 7-O-rhamnoside. **b** Chemical structure of quercetin-3-neohesperidoside-7-rhamnoside. **c** Chemical structure of quercetin 3-[rhamnosyl-(1- > 2)-alpha-L-arabinopyranoside]

oral route that identified 40 different compounds with high positive drug-likeness scores were considered to have good oral absorption (Table 1) that were used for further studies.

The concept of "single drug-single protein disease" involved in the regular drug discovery process might not be beneficial in managing the infectious disease. This is possible because of the greater affinity of the available pathogens (viruses and bacteria) to alter the multiple homeostatic functions of the protein molecules, which means different proteins present in pathogens are responsible for generating this effect. Management of this process can therefore be carried out by utilization of the "multi compound-multi protein-disease" concept, which is a modified drug development process interaction where multiple bioactives are involved in the regulation of multiple proteins [43], which in turn can be used as a basic key in the up-regulation of the immune system. Therefore, this present study deals with the combined synergistic phenomenon of quercetin derivatives, an investigation of which was done rather than the investigation of a single bioactive molecules to find out the multiple pathways that are directly or indirectly linked with the immune system.

The gene set enrichment analysis helped identify multiple pathways such as the p53 signaling pathway [44] and NF-kappa B signaling pathway [45] that has an involvement in upscaling of the immune system. Also, the other pathways like that of pathways in cancer, prostate cancer, MicroRNAs in cancer, hepatocellular carcinoma, endometrial cancer, breast cancer, and gastric cancer reflect quercetin derivatives potency in patients suffering from diseases like cancer from these mentioned pathways. Also, diseases like obesity and diabetes associated with pathways like p53 signaling pathways, PI3K-Akt, Wnt signaling are proven to be beneficial if regulated by the quercetin derivatives in patients with compromised immunity, thereby can act as a preventative strategy during the management of COVID-19. Further, herbal medicines rich in quercetin have potential antiviral properties against multiple viruses. Therefore, in this study, an attempt was conducted to evaluate the possible antiviral activity of quercetin derivatives against different viruses like influenza, HIV, rhinovirus, hepatitis B, hepatitis C, Trachoma, Picornavirus, CMV, and herpes virus based on their high-positive drug-likeness scores.

It was found that in the incorporation of viral polypeptides and deregulation of the homeostatic task of functional proteins, 3CL pro alters the ubiquitin regulatory protein consisting of 76 amino acids [46] that were majorly targeted by quercetin-3-neohesperidoside-7-rhamnoside. Furthermore, alteration of protein phosphate 1A and protein phosphate 1B, which regulates the replicase proteins to adjust viral cell life, is altered by PLpro [47] modulated by quercetin 3-O-arabinoside 7-O-rhamnoside. Similarly, the spike protein utilizes the ACE-2 (angiotensin-converting enzyme 2) as its target receptor to invade the host cell [48, 49], and this was chiefly modulation by quercetin 3-[rhamnosyl-(1- > 2)-alpha-L-arabinopyranoside]. In most of the studies conducted, the natural compounds were able to inhibit specifically one or two target proteases of SARS-CoV-2, but during our in silico study, we could identify three new hit derivatives of parent quercetin molecule, which could potentially inhibit all the three essential targets of SARS-CoV-2 as discussed above. Also, network pharmacology-based study and protein-protein interaction study were included along with molecular docking and molecular dynamics simulations to identify the specific pathways through which these potential quercetin derivatives will act, which was found to be missing from most of the in silico-based studies present in literature. The above

results reflect the possibility of quercetin derivatives to act as a potential antiviral agent against SARS-CoV-2.

Conclusion

The present study was carried out BY utilizing the in silico molecular docking tools to identify the affinity of quercetin derivatives binding against 3clpro, PLpro that was recorded previously. Also, the study was carried out to identify the affinity of quercetin binding against the spike protein receptor-binding domain. Quercetin 3-O-arabinoside 7-O-rhamnoside, quercetin 3-[rhamnosyl-(1->2)-alpha-L-arabinopyranoside], and quercetin-3-neohesperidoside-7-rhamnoside are considered as the lead hits. Also, the identification of the modulation of multiple pathways like p53, Wnt signaling pathway, RIG-I-like receptor signaling pathway was estimated using the network combined synergies generated. In addition, the quercetin derivatives were also found to be the modulators of specific disease pathways like diabetes and obesity, where immunity is compromised. All the available results provided a clear suggestion about the possible therapeutic activity in utilizing quercetin derivative as an immune modulator and an antiviral agent against the novel coronavirus. However, the above study's findings are based only on the computer simulations, validation of which with an adequately designed experimental protocol is necessary.

Future perspective and possible applications

The COVID-19 pandemic caused numerous social and economic disruptions around the world, and the effects of the epidemic are still being felt. Several efforts were made to counteract the effect and bring things back to normal. There is always a quest for lead compounds that can be useful in neutralizing the adverse effects of foreign substances entering our immune system, and the same is true for the COVID-19 therapy strategy.

In silico studies give a solid scientific foundation for three new quercetin derivatives as possible anti-SARS-CoV-2 agents. The in silico experiments indicated a substantial interaction of quercetin analogs with various SARS-CoV-2 proteases, leading to the conclusion that these newly identified quercetin derivatives could be used as a lead molecule. Although more research into the efficiency of three new quercetin derivatives is needed, it is possible that these analogs could be explored for antiviral therapy. It is possible to expand the current investigation to include in vitro and in vivo experiments using experimental animals to investigate the effects of quercetin analogs on antiviral therapy. It may be useful to confront SARS CoV-2 in a more substantial manner after acquiring positive results for the examined compounds using in vitro and in vivo procedures. This evidence-based study can be used to build a formulation of choice subject to achieving the intended effect, which will be useful against the COVID-19 therapy regimen. Furthermore, various developments in targeted delivery systems might be used in this lead molecule, which could be advantageous in delivering the agent of choice in the amount required to avoid future problems caused due to the virus strains.

Abbreviations

COVID-19: Coronavirus disease; ChEBI: Chemical Entities of Biological Interest; CMV: Cytomegalovirus; 3CLpro: 3C-like protease; DENV-2: Dengue virus type 2; DIGEP-Pred: Prediction of drug-induced changes of gene expression profile; FRET: Fluorescence resonance energy transfer; HIV: Human immunodeficiency virus; HSV-1: Herpes simplex virus-1; NMA: Normal mode analysis; PLpro: Papain-like protease; Pa: Pharmacological activity; Pi: Pharmacological inactivity; RSV: Respiratory syncytial virus; SARS-CoV-2: Severe acute respiratory syndrome coronavirus 2; SMILE: Simplified Molecular Input Line Entry System; TMPRSS2: Transmembrane serine protease 2; UFF: Universal forcefield.

Acknowledgements

All the authors are thankful to NETES Institute of Pharmaceutical Science, Assam, India, for providing all the necessary support for completing the study.

Authors' contributions

KB: protocol development, alongside performing the work and drafting of the manuscript. RB and BJS were involved in reviewing and finalizing the manuscript. NRC, RK, and AB authors equally contributed to mining the database and assisted in carrying out the study. All authors read and approved the final manuscript.

Funding

Not applicable.

Availability of data and materials

We declare that all the data generated are included in this study.

Declarations

Ethics approval and consent to participate

Not applicable.

Consent for publication

Not applicable.

Competing interests

All authors declare that they have no competing interests.

Author details

[1]NETES Institute of Pharmaceutical Science, Mirza, Guwahati, Assam 781125, India. [2]Assam Science and Technology University, Guwahati, Assam, India. [3]Faculty of Pharmaceutical Science, Assam Downtown University, Guwahati, Assam, India. [4]Royal School of Pharmacy, Royal Global University, Guwahati, Assam, India.

Received: 19 November 2021 Accepted: 4 February 2022
Published online: 09 March 2022

References

1. Miura TA, Holmes KV (2009) Host-pathogen interactions during coronavirus infection of primary alveolar epithelial cells. J Leukoc Biol 86:1145–1151 https://doi.org/10.1189/jlb.0209078
2. University of Melbourne (2020) Science News. Activation and cancer development. Oncogene. 29:4493–4503 https://www.sciencedaily.com/

releases/2020/03/200317103815.htm. Accessed 29 Sept 2021. https://doi.org/10.1038/onc.2010.190
3. Khanal P, Duyu T, Patil BM, Dey YN, Pasha I, Kavalapure RS, Chand S, Gurav S (2021) Screening of JAK-STAT modulators from the antiviral plants of Indian traditional system of medicine with the potential to inhibit 2019 novel coronavirus using network pharmacology. 3 Biotech 11:1–18 https://doi.org/10.1007/s13205-021-02664-4
4. Khanal P, Duyu T, Patil BM, Dey YN, Pasha I, Wanjari M, Gurav SS, Maity A (2020) Network pharmacology of AYUSH recommended immune-boosting medicinal plants against COVID-19. J Ayurveda Integr Med:0–4 https://doi.org/10.1016/j.jaim.2020.11.004
5. Zhang DH, Wu KL, Zhang X, Deng SQ, Peng B (2020) In silico screening of Chinese herbal medicines with the potential to directly inhibit 2019 novel coronavirus. J Integr Med 18:152–158 https://doi.org/10.1016/j.joim.2020.02.005
6. Mahdian S, Ebrahim HA, Zarrabi M (2020) Drug repurposing using computational methods to identify therapeutic options for COVID-19. J Diabetes Metab Disord. 19:691–699 https://doi.org/10.1007/s40200-020-00546-9
7. Rapid Risk Assessment: Detection of new SARS-CoV-2 variants related to mink. European Centre for Disease Prevention and Control (2020) Available from: https://www.ecdc.europa.eu/en/publications-data/detection-new-sars-cov-2-variants-mink.
8. European Centre for Disease Prevention and Control (2021) Assessing SARS-CoV-2 circulation, variants of concern, non-pharmaceutical interventions and vaccine rollout in the EU/EEA, 15th update – 10 June 2021. ECDC, Stockholm
9. Kumar S, Thambiraja TS, Karuppanan K, Subramaniam G (2021) Omicron and Delta Variant of SARS-CoV-2: A Comparative Computational Study of Spike Protein. J Med Virol. https://doi.org/10.1002/jmv.27526
10. Bhattacharya K, Chanu NR, Bhattacharjee A, Bordoloi R, Sahariah BJ, Talukdar A, Kalita R (2021) Quercetin for the experimantal treatment of COVID-19. In: Handbook of Research on Knowledge and Organisation Systems in Library and Information Science, pp 69–87 https://doi.org/10.4018/978-1-7998-7258-0.ch004
11. Debiaggi M, Tateo F, Pagani L, Luini M, Romero E (1990) Effects of propolis flavonoids on virus infectivity and replication. Microbiologica 13:207–213
12. De Palma AM, Vliegen I, De Clercq E, Neyts J (2008) Selective inhibitors of picornavirus replication. Med Res Rev. 28:823–884 https://doi.org/10.1002/med.20125
13. Itsuka H, Ohsawa C, Ohiwa T, Umeda I, Suhara Y (1982) Antipicornavirus flavone Ro 09- 0179. Antimicrob Agents Chemother. 22:611–616 https://doi.org/10.1128/AAC.22.4.611
14. Kaul TN, Middleton E Jr, Ogra PL (1985) Antiviral effect of flavonoids on human viruses. J Med Virol. 15:71–79 https://doi.org/10.1002/jmv.1890150110
15. Evers DL, Chao CF, Wang X, Zhang Z, Huong SM, Huang ES (2005) Human cytomegalovirus-inhibitory flavonoids: studies on antiviral activity and mechanism of action. Antiviral Res. 68:124–134 https://doi.org/10.1016/j.antiviral.2005.08.002
16. Zandi K, Teoh BT, Sam SS, Wong PF, Mustafa MR, Abubakar S (2011) Antiviral activity of four types of bioflavonoid against dengue virus type-2. Virol J. 8:560 https://doi.org/10.1186/1743-422X-8-560
17. Veckenstedt A, Béládi I, Mucsi I (1978) Effect of treatment with certain flavonoids on Mengo virus-induced encephalitis in mice. Arch Virol. 57:255–260 https://doi.org/10.1007/bf01315089
18. Güttner J, Veckenstedt A, Heinecke H, Pusztai R (1982) Effect of quercetin on the course of mengo virus infection in immunodeficient and normal mice. A histologic study. Acta Virol 26:148–155
19. Nieman DC, Henson DA, Gross SJ, Jenkins DP, Davis JM, Murphy EA, Camichael MD, Dumke CL, Utter AC, McAnulty SR, McAnulty LS, Mayer EP (2007) Quercetin reduces illness but not immune perturbations after intensive exercise. Med Sci Sports Exerc. 39:1561–1569 https://doi.org/10.1249/mss.0b013e318076b566
20. Lagunin A, Ivanov S, Rudik A, Filimonov D, Poroikov V (2013) DIGEP-Pred: Web service for in silico prediction of drug-induced gene expression profiles based on structural formula. Bioinformatics 29:2062–2063 https://doi.org/10.1093/bioinformatics/btt322
21. Szklarczyk D, Morris JH, Cook H, Kuhn M, Wyder S, Simonovic M, Santos A, Doncheva NT, Roth A, Bork P, Jensen LJ, Von MC (2017) The STRING database in 2017: Quality-controlled protein-protein association networks, made broadly accessible. Nucleic Acids Res 45:D362–D368 https://doi.org/10.1093/nar/gkw937
22. Shannon P, Markiel A, Ozier O, Baliga NS, Wang JT, Ramage D, Amin N, Schwikowski B, Ideker T (1971) Cytoscape: a software environment for integrated models. Genome Res 13:426 https://doi.org/10.1101/gr.1239303.metabolite
23. Khanal P, Patil BM (2020) α-Glucosidase inhibitors from Duranta repens modulate p53 signaling pathway in diabetes mellitus. Adv Tradit Med 20:427–438 https://doi.org/10.1007/s13596-020-00426-w
24. Borodina Y, Sadym A, Filimonov D, Blinova V, Dmitriev A, Poroikov V (2003) Predicting biotransformation potential from molecular structure. J Chem Inf Comput Sci 43:1636–1646 https://doi.org/10.1021/ci034078l
25. Biovia DS (2021) Discovery Studio client (DassaultSystèmes, San Diego, 2021), p 2021
26. Rappe AK, Casewit CJ, Colwell KS, Goddard WA, Skiff WM (1992) UFF, a full periodic table force field for molecular mechanics and molecular dynamics simulations. J Am Chem Soc 25:10024–10035 https://doi.org/10.1021/ja00051a040
27. Kondapuram SK, Sarvagalla S, Coumar MS (2021) Docking-based virtual screening using PyRx Tool: autophagy target Vps34 as a case study. Mol Docking Comput Aided Drug Design:463–477 https://doi.org/10.1016/B978-0-12-822312-3.00019-9
28. Khanal P, Patil BM, Hullatti KK (2019) *In silico* Antidiabetic Screening of Borapetoside C, Cordifolioside A and Magnoflorine. Indian J Pharm Sci 81:550–555 https://10.36468/pharmaceutical-sciences.543
29. Khanal P, Magadum P, Patil BM, Hullatti KK (2019) *In silico* docking study of limonoids from *Azadirachta indica* with pfpk5: a novel target for *Plasmodium falciparum*. Indian J Pharm Sci 81:326–332 https://10.36468/pharmaceutical-sciences.514
30. Lopez BJR, Aliaga JI, Quintana OES, Chacon P (2014) iMODS: Internal coordinates normal mode analysis server. Nucleic Acids Res 42:W271–W276. https://doi.org/10.1093/nar/gku339
31. Lopez BJR, Garzon JI, Chacon P (2011) iMod: Multipurpose normal mode analysis in internal coordinates. Bioinformatics 27:2843–2850. https://doi.org/10.1093/bioinformatics/btr497
32. Adasme MF, Linnemann KL, Bolz SN, Kaiser F, Salentin S, Haupt VJ, Scroeder M (2021) PLIP 2021: expanding the scope of the protein–ligand interaction profiler to DNA and RNA. Nucl Acids Res 49:530–534 https://doi.org/10.1093/nar/gkab294
33. Huang Y, Yang C, Xu XF, Xu W, Liu SW (2020) Structural and functional properties of SARS-CoV-2 spike protein: potential antivirus drug development for COVID-19. Acta Pharmacol Sin. 41:1141–1149
34. Wrapp D, Wang N, Corbett KS, Goldsmith JA, Hsieh CL, Abiona O, Graham BS, McLellan JS (2020) Cryo-EM structure of the 2019-nCoV spike in the prefusion conformation. Science. 367:1260–1263
35. Pluskota KD, Hoffmann M, Barciszewski J (2021) Reducing SARS-CoV-2 pathological protein activity with small molecules. J Pharm Anal. 11:383–397
36. Shin D, Mukherjee R, Grewe D, Bojkova D, Baek K, Bhattacharya A, Schulz L, Widera M, Mehdipour AR, Tascher G, Geurink PP, Wilhelm A, Noort GJ, Ovaa H, Muller S, Knobeloch KP, Rajalingam K, Schulman BA, Cinatl J, Hummer G, Ciesek S, Dikic I (2020) Papain-like protease regulates SARS-CoV-2 viral spread and innate immunity. Nature. 587:657–662
37. Humayun F, Khan A, Ahmad S, Yuchen W, Wei G, Nizam UN, Hussain Z, Khan W, Zaman N, Rizwan M, Waseem M, Wei DQ (2021) Abrogation of SARS-CoV-2 interaction with host (NRP1) neuropilin-1 receptor through high-affinity marine natural compounds to curtail the infectivity: a structural-dynamics data. Comput Biol Med.:104714 https://doi.org/10.1016/j.compbiomed.2021.104714
38. Ghosh R, Chakraborty A, Biswas A, Chowdhuri S (2021) Evaluation of green tea polyphenols as novel corona virus (SARS-CoV-2) main protease (Mpro) inhibitors—An in silico docking and molecular dynamics simulation study. J Biomol Struct Dyn. 39:4362–4374
39. Jo S, Kim S, Shin DH, Kim MS (2020) Inhibition of SARS-CoV 3CL protease by flavonoids. J Enzym Inhib Med Chem. 35:145–151
40. Jo S, Kim S, Kim DY, Kim MS, Shin DH (2020) Flavonoids with inhibitory activity against SARS-CoV-2 3CLpro. J Enzym Inhib Med Chem. 35:1539–1544
41. Wang SC, Chen Y, Wang YC, Wang WJ, Yang CS, Tsai CL, Hou MH, Chen HF, Shen YC, Hung MC (2020) Tannic acid suppresses SARS-CoV-2 as a dual inhibitor of the viral main protease and the cellular TMPRSS2 protease. Am J Cancer Res 10:4538–4546

42. Lipinski CA (2004) Lead- and drug-like compounds: the rule-of-five revolution. Drug Discov Today Technol 1:337–341 https://doi.org/10.1016/j.ddtec.2004.11.007
43. Khanal P, Patil BM (2020) Gene ontology enrichment analysis of α-amylase inhibitors from Duranta repens in diabetes mellitus. J Diabetes Metab Disord 19:735–747 https://doi.org/10.1007/s40200-020-00554-9
44. Fontela CM, Mandinova A, Aaronson SA, Lee SW (2016) Emerging roles of p53 and other tumour-suppressor genes in immune regulation. Nat Rev Immunol 16:741–750 https://doi.org/10.1038%2Fnri.2016.99
45. Sokol CL, Luster AD (2015) The chemokine system in innate immunity. Cold Spring Harb Perspect Biol 7:1–20 https://doi.org/10.1101/cshperspect.a016303
46. Yang WL, Zhang X, Lin HK (2010) Emerging role of Lys-63 ubiquitination in protein kinase and phosphatase activation and cancer development. Oncogene 29:4493–4503 https://doi.org/10.1038/onc.2010.190
47. Lindner HA, Fotouhi AN, Lytvyn V, Lachance P, Sulea T, Ménard R (2005) The papain-like protease from the severe acute respiratory syndrome coronavirus is a deubiquitinating enzyme. J Virol 79:15199–15208 https://doi.org/10.1128/jvi.79.24.15199-15208.2005
48. Tanonaka K, Marunouchi T (2016) Angiotensin-converting enzyme 2. Folia Pharmacol Jpn 147:120–121 https://doi.org/10.1254/fpj.147.120
49. Kuhn JH, Li W, Choe H, Farzan M (2004) Angiotensin-converting enzyme 2: A functional receptor for SARS coronavirus. Cell Mol Life Sci 61:2738–2743 https://doi.org/10.1007/s00018-004-4242-5

Publisher's Note

Journal of Biomolecular Structure and Dynamics

ISSN: (Print) (Online) Journal homepage: https://www.tandfonline.com/loi/tbsd20

Computational pharmacology profiling of borapetoside C against melanoma

Kunal Bhattacharya, Pukar Khanal, Vishal S. Patil, Prarambh S. R. Dwivedi, Nongmaithem Randhoni Chanu, Raushan Kumar Chaudhary, Satyendra Deka & Arup Chakraborty

To cite this article: Kunal Bhattacharya, Pukar Khanal, Vishal S. Patil, Prarambh S. R. Dwivedi, Nongmaithem Randhoni Chanu, Raushan Kumar Chaudhary, Satyendra Deka & Arup Chakraborty (2023): Computational pharmacology profiling of borapetoside C against melanoma, Journal of Biomolecular Structure and Dynamics, DOI: 10.1080/07391102.2023.2213333

To link to this article: https://doi.org/10.1080/07391102.2023.2213333

JOURNAL OF BIOMOLECULAR STRUCTURE AND DYNAMICS
https://doi.org/10.1080/07391102.2023.2213333

Computational pharmacology profiling of borapetoside C against melanoma

Kunal Bhattacharya[a,b], Pukar Khanal[c], Vishal S. Patil[d], Prarambh S. R. Dwivedi[c], Nongmaithem Randhoni Chanu[a,e], Raushan Kumar Chaudhary[f], Satyendra Deka[a] and Arup Chakraborty[a]

[a]Pratiksha Institute of Pharmaceutical Sciences, Guwahati, Assam, India; [b]Royal School of Pharmacy, The Assam Royal Global University, Guwahati, Assam, India; [c]Department of Pharmacology, NGSM Institute of Pharmaceutical Sciences (NGSMIPS), Nitte (Deemed to be University), Mangalore, India; [d]KLE College of Pharmacy, KLE Academy of Higher Education and Research, Belagavi, India; [e]Faculty of Pharmaceutical Science, Assam Downtown University, Guwahati, Assam, India; [f]Department of Pharmacy Practice, NGSM Institute of Pharmaceutical Sciences (NGSMIPS), Nitte (Deemed to be University), Mangalore, India

Communicated by Ramaswamy H. Sarma

ABSTRACT

Melanoma,also known as a '*black tumor*', begins in the melanocytes when cells (that produce pigment) grows out of control. Immunological dysregulation, which raises the risk for multiple illnesses, including melanoma, may be influenced by stress tiggered through viral infection, long term effects of ultraviolet radiation, environmental pollutants etc. Borapetoside C is one of the phytoconstituents from *Tinospora crispa*, and its biological source has been reported for its antistress property. Network pharmacology and KEGG pathway analysis of borapetoside C-regulated proteins were conducted to identify the hub genes involved in melanoma development. Further, a molecular docking was performed between borapetoside C and targets involved in melanoma. Further, the top *3* complexes were selected based on the binding energy to conduct molecular dynamics simulations to evaluate the stability of ligand-protein complex followed by principal component analysis and dynamic cross-correlation matrix. In addition, borapetoside C was also screened for its pharmacokinetics and toxicity profile. Network Pharmacology studies and KEGG pathway analysis revealed *8* targets involved in melanoma. Molecular docking between borapetoside C and targets involved in melanoma identified *3* complexes with minimum binding i.e. borapetoside C- *MAP2K1*, *MMP9*, and *EGFR*. Further, molecular dynamics simulations showed a stable complex of borapetoside C with *MMP9* and *EGFR*. The present study suggested that borapetoside C may target *MMP9* and *EGFR* to possess an anti-melanoma property. This finding can be useful in developing a novel therapeutic agent against melanoma from a natural source.

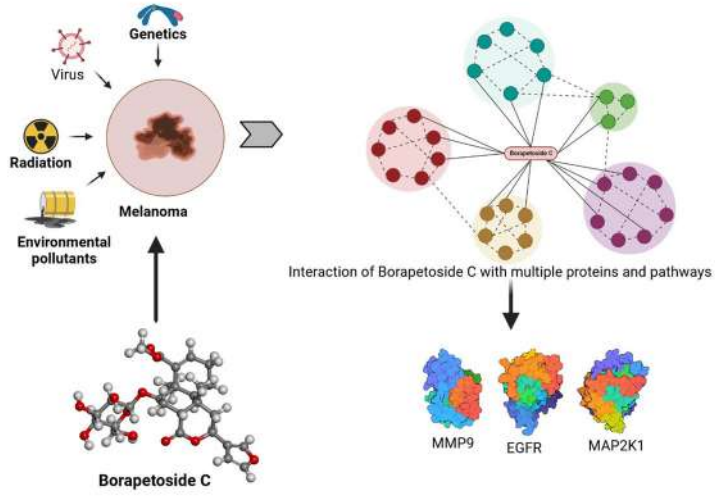

ARTICLE HISTORY
Received 25 January 2023
Accepted 4 May 2023

KEYWORDS
Bioinformatics; borapetoside C; melanoma; network pharmacology; *Tinospora crispa*

1. Introduction

Melanocytes produce the ultraviolet (UV)-absorbing pigment melanin and are located at the basal level of the epidermis. Melanocyte-stimulating hormone is secreted by keratinocytes in response to UV light exposure, and this hormone subsequently binds with the melanocortin 1 receptor to produce

CONTACT Pukar Khanal pukarkhanal58@gmail.com Department of Pharmacology, NGSM Institute of Pharmaceutical Sciences, Nitte deemed to be University, Mangalore, India.

Supplemental data for this article can be accessed online at https://doi.org/10.1080/07391102.2023.2213333.

melanin (Williams *et al*., 2011). Melanocytes produce both eumelanin and pheomelanin. A decreased risk of developing skin cancer is associated with a higher concentration of the UV-protective pigment eumelanin, which is present in darker skin tones. The formation of pheomelanin not only results in carcinogens (Seiberg, 2001; Morgan *et al*., 2013; Mitra *et al*., 2012) but also provides less protection from UV light. There is evidence that pheomelanin increases UV-induced reactive oxidative species, which in turn increases deoxyribonucleic acid (DNA) damage (Seiberg, 2001; Morgan *et al*., 2013; Gajula & Gaddameedhi, 2015; Robles-Espinoza *et al*., 2016). Cancer data from the Centers for Disease Control and Prevention show that 22.1% of every 100,000 Americans develop melanoma (malignant tumor originating from melanocytes). Despite only making up 4% of skin cancer incidences, it is responsible for 75% of skin cancer-related fatalities. Therefore, there is a need for new chemotherapeutic agents against melanoma with minimal side effects.

Tinospora species are frequently employed in multiple forms of traditional medicine for a variety of reasons (Gray-Schopfer *et al*., 2007). Previously, the use of *T. cordifolia* lotion has been recommended against *Sarcoptes scabiei* infection to combat scabies (Castillo *et al*., 2013). In addition, *T. cordifolia* exerts antiosteoporosis, anti-diabetic, hypolipidemic, anticancer, anti-HIV, antitoxic, immunomodulating, wound healing, and antioxidant effects (Sharma *et al*., 2019). The adaptogenic capacity of *T. cordifolia* was reported to boost physical performance while at the same time inhibiting excessive activation of the sympathetic nervous system (Salve *et al*., 2015).

It has been reported that stress hormones like norepinephrine promote the function of cytokines like interleukin *6* and *8*, which are proangiogenic and assist tumor growth. It is believed that stress, in conjunction with genetic and environmental variables, may contribute to developing melanoma and its progression (Sinnya & De'Ambrosis, 2013). In addition, previously, *T. crispa* has been reported to inhibit MMP-13 and also check the migration of squamous cell carcinoma cell lines (Phienwej *et al*., 2015) followed by antiproliferative activities on different human cancer cell lines (Zulkhairi *et al*., 2008). Further, borapetoside C (a furanoid diterpene glycoside) is one of the active phytoconstituent from *T. crispa* (Ruan *et al*., 2012; Hossen *et al*., 2016). Based on these study backgrounds, we attempted to screen borapetoside C (Figure 1) as a potential anti-melanoma compound.

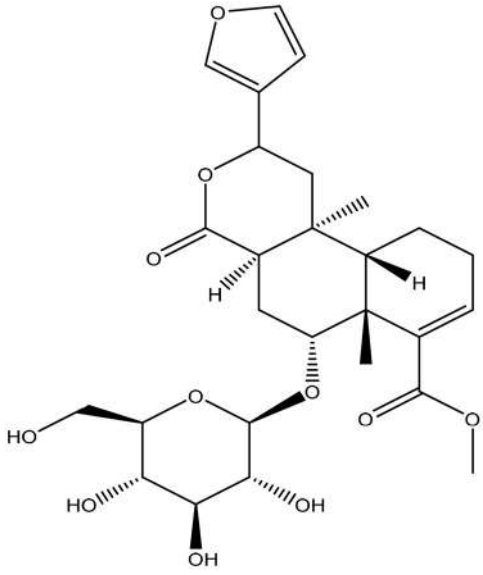

Figure 1. 2D structure of borapetoside C. PubChem CID: *101697033*, molecular formula: $C_{27}H_{36}O_{11}$, molecular weight: 536.6, InChIKey: RBPCODNTTHTSFN-OLHDSMRXSA-N.

2. Materials and methods

2.1. Assessment of pharmacokinetic, and toxicity profile and targets of borapetoside C

Absorption, distribution, metabolism, and excretion (ADME) and probable side effects (related toxicity effects) profile of borapetoside C were predicted by SwissADME (Daina *et al*., 2017; http://www.swissadme.ch/) and ADVERPred (Ivanov *et al*., 2018; https://www.way2drug.com/adverpred/) online servers, respectively. Borapetoside C-regulated targets were identified from SwissTargetPrediction (Gfeller *et al*., 2014; http://www.swisstargetprediction.ch/) and DIGEP-Pred (Lagunin et al., 2013; http://www.way2drug.com/ge/) by querying its simplified molecular input line entry system (SMILES). The reported targets of melanoma (UMLS CUI: *C0025202*) were retrieved from the DisGeNET database (Piñero *et al*., 2017; https://www.disgenet.org/). Further, the borapetoside C-regulated targets (involved in melanoma) overlapped with UMLS CUI: *C0025202* were identified using Venny 2.1.0 (https://bioinfogp.cnb.csic.es/tools/venny/).

2.2. Enrichment analysis

Borapetoside C-modulated melanoma proteins were enriched in a search tool for the retrieval of interacting genes/proteins (STRING) database (Snel *et al*., 2000; https://string-db.org/) in a full network at *0.4* confidence and *5*% FDR stringency to trace gene ontology terms and probably modulated Kyoto Encyclopedia of Genes and Genomes (KEGG) pathways at *5*% false discovery rate stringency for *Homo sapiens*. The protein-protein interactions were evaluated based on known interactions (curated databases and experimentally determined), predicted interactions (gene neighbourhood, gene fusions, and gene co-occurrence), and miscellaneous (text mining, co-expression, and protein homology) by assuming whole genome statistical background.

2.3. Disease-protein network construction and analysis

Before constructing the network, all the KEGG disease records were evaluated for '*cancer*' by using '*melanoma*', '*sarcoma*', '*cancer*', '*glioma*', '*leukemia*', and '*carcinoma*' keywords. The disease-proteins-borapetoside C network was constructed using Cytoscape (Shannon *et al*., 2003; https://cytoscape.org). The protein-protein network was evaluated by treating it directed. Also, the disease (KEGG pathways) -protein-borapetoside C network was evaluated by treating it undirected by setting the node size as '*low values to small sizes*' and node color from '*low values to bright colors*' (Dwivedi *et al*., 2021).

2.4. In silico molecular docking of borapetoside C with proteins involved in melanoma

2.4.1. Protein preparation

The 3D structures of serine/threonine-protein kinase B-raf; *BRAF* (PDB: 3C4C), matrix metalloproteinase-9; *MMP9* (PDB: 1L6J), epidermal growth factor receptor; *EGFR* (PDB: 1M17), mitogen-activated protein kinase-1; *MAPK1* (PDB: 1TVO), dual specificity mitogen-activated protein kinase kinase 1; *MAP2K1* (α-fold ID: AF- A4QPA9), caspase *3*; *CASP3* (α-fold ID: AF-C9JXR7), mitogen-activated protein kinase *3*; *MAPK3* (α-fold ID: AF-H0YEX6) and matrix metalloproteinase 2; MMP2 (α-fold ID: AF-Q2EF79*)* were retrieved from Research Collaboratory for Structural Bioinformatics (RCSB; https://www.rcsb.org/) protein data bank and Uniprot databases (https://www.uniprot.org/) as applicable. The water molecules and pre-complexed ligands were removed using Biovia Discovery Studio (https://discover.3ds.com/discovery-studio-visualizer-download) *ver.* 2021 and prepared for molecular docking (Bhattacharya *et al*., 2022).

2.4.2. Ligand molecule preparation

Borapetoside C (PubChem CID: *101697033*) in .sdf format was retrieved from PubChem (https://pubchem.ncbi.nlm.nih.gov/) database, which was further converted into .pdb format using Discovery Studio Visualizer *ver.* 2021, energy was minimized and later used as a ligand.

2.4.3. Prediction of the active site in receptors

The active site of macromolecules was identified using the Indian Institute of Technology, Delhi's supercomputing facility for bioinformatics and computational biology server (http://www.scfbio-iitd.res.in/dock/ActiveSite.jsp) to search all of the possible binding cavities. The cavity possessing the highest volume was selected to dock the ligand as it would be the most suitable site for molecular docking. The cavity points were noted for performing docking with Auto Dock Tools 1.5.6 (Morris *et al*., 2009; https://autodock.scripps.edu/).

2.4.4. Molecular docking of borapetoside C with proteins involved in melanoma

Borapetoside C was docked against *BRAF* (x: *−7.300*, y: *−11.297*, and z: *−29.103*), *CASP3* (x: *−5.733*, y: *−4.309*, and z: *2.780*), *EGFR* (x: *29.215*, y: *8.321*, and z: *47.322*), *MAP2K1* (x: *−14.657*, y: *12.892*, and z: *15.158*), *MAPK1* (x: *4.593*, y: *−7.431*, and z: *12.564*), *MAPK3* (x: *−2.215*, y: *−1.484*, and z: *14.597*), *MMP2* (x: *−6.543*, y: *4.236*, z: *2.996*), *MMP9* (x: *34.362*, y: *44.387*, and z: *24.453*) using Auto Dock Tools at 60 dimensions (x, y, and z) and 0.5 Å space. After docking, the ligand posewith the minimum binding energy was selcted to visualize the ligand-protein interaction in Biovia Discovery Studio 2021 (Bhattacharya *et al*., 2022).

2.5. Molecular dynamics simulation

To examine docked complexes' structural and intermolecular interaction stabilities, an all-atom explicit molecular dynamics (MD) simulation for 100 ns was carried out. The GROMACS (https://www.gromacs.org) 2021.3 software package with Amber ff99SB-ildn force field was employed during the simulation as demonstrated previously (Van Der Spoel *et al*., 2005; Dwivedi *et al*., 2022). The topological parameters of the ligand and the whole complex were generated using the xleap module of AmberTools (https://ambermd.org/AmberTools.php), and the partial charges of the small molecules were obtained by doing quantum calculations using an antechamber with a '*bcc*' charge model. The prepared system was solvated in a rectangular box with 10.0 Å boundary conditions from the protein's borders in all directions using the *3*-site water (TIP3P) model. The charges on the prepared system were neutralized by introducing the required number of counter ions. To find the near-global state least energy conformations, the steepest descent followed by the conjugate gradient energy minimization method was applied. Canonical (NVT) and isobaric (NPT) ensembles were used to equilibrate the system for 1 ns. A modified Berendsen thermostat method was used in NVT equilibration to maintain the volume and temperature constant (300 K). Parrinello-Rahman barostat was used to maintain the pressure at 1 bar constant during NPT equilibration. In addition, the Particle Mesh Ewald approximation was used with a cut-off value of 1 nm to calculate the long-range electrostatic interactions, van der Waals, and coulomb interactions. Similarly, bond length was constrained using the LINear Constraint Solver algorithm. Finally, each complex was simulated for a 100 ns production run with coordinates at every 2 fs. The trajectories produced were examined using the built-in gromacs utilities. The MD plots were constructed using xmgrace.

2.5.1. Evaluation of binding affinity using molecular mechanics poisson–boltzmann surface area

In MD simulations and thermodynamic calculations, the relative binding energy of a ligand-protein complex was employed to evaluate the binding affinities. In the present study, the relative binding energy and its contribution to individual residues were calculated *via* the molecular mechanics Poisson–Boltzmann surface area (MM-PBSA) method using the '*g mmpbsa*' tool (Kumari *et al*., 2014). The parameters from past studies (Bhandare *et al*., 2019; Bhandare & Ramaswamy, 2018) were considered while calculating the binding energy. The binding energy was determined throughout the stable trajectory observed between 50 and 100 ns using 50 representative snapshots.

2.5.2. Principal component analysis

Using MD trajectories, principal component analysis investigates the molecular motion i.e. translational and rotational mobility of the molecule using the '*least square fit*' to the reference structure (Amadei *et al*., 1993; Amadei *et al*., 1996; Moharana *et al*., 2022). The direction of the molecule's motion is reflected in a group of eigenvectors that are produced by diagonalizing a covariance matrix which was created by a linear transform of cartesian coordinate space. The energy contribution of each eigenvector to the motion shown by the eigenvalue is associated with the eigenvector.

The '*time-dependent movements*' that the components carry out in a certain vibrational mode are demonstrated by projecting the trajectory onto a particular eigenvector. The atomic vibrational components' contribution towards this form of coordinated motion is demonstrated by the projection's time average. Using the built-in gromacs utilities '*g_covar*', the eigenvectors and eigenvalues of the trajectory were produced by computing and diagonalizing the covariance matrix. Additionally, the eigenvectors were examined and illustrated using the '*g_anaeig*' program.

2.5.3. The dynamic cross-correlation matrix

To determine if motion between atom pairs is correlated (positive or negative), the dynamic cross-correlation matrix was used to measure the magnitude of all pairwise cross-correlation coefficients (Khanal *et al*., 2021; Khanal *et al*., 2022). In this section, using MD trajectory we examined each dynamic cross-correlation matrix component. $C_{ij} = 1$ denotes that the fluctuations of *i* and *j* have the same period and phase (positive correlation), $C_{ij} = 0$ denotes that there is no correlation, and $C_{ij} = 1$ denotes that the fluctuations have a negative correlation.

3. Results

3.1. Pharmacokinetic, and toxicity profile and targets of borapetoside C

Borapetoside C was predicted to be soluble in water with low gastrointestinal absorption (according to boiled egg theory) and *2.62* LogP. In addition, it was predicted as a p-glycoprotein substrate, a noninhibitor of *CYP1A2*, *CYP2C19*, *CYP2C9*, *CYP2D6*, and *CYP3A4* and non-blood-brain barrier permeable. Further, borapetoside C side effects were predicted as nephrotoxic with a pharmacological activity (Pa) value of *0.377* (Pa value *0* to *1* represents low to high toxicity).

Concerning previously recorded targets for melanoma (UMLS CUI: *C0025202*; DisGeNET), we identified borapetoside C to regulate *65* proteins (*ACHE*, *ACVRL1*, *ADAM17*, *ADORA2A*, *AGTR1*, *ALOX5*, *AURKA*, *AURKB*, *BCL2A1*, *BRAF*, *CA2*, *CA9*, *CASP1*, *CASP3*, *CASP6*, *CASP7*, *CASP8*, *CDK2*, *CDK4*, *CHEK1*, *CTSD*, *DHFR*, *DPP4*, *EGFR*, *EIF4A1*, *EPHB4*, *ERBB2*, *F3*, *FGFR1*, *IGF1R*, *IGFBP3*, *ITGAL*, *JAK1*, *JAK2*, *KDR*, *LGALS1*, *LGALS3*, *LGALS7*, *LGALS9*, *MAP2K1*, *MAP3K9*, *MAPK1*, *MAPK14*, *MAPK3*, *MME*, *MMP1*, *MMP13*, *MMP14*, *MMP2*, *MMP8*, *MMP9*, *OPRM1*, *PDE2A*, *PDE5A*, *PIM1*, *PIM3*, *PTGES*, *REN*, *SIRT2*, *SLC2A1*, *SLC5A2*, *SMN2*, *SOAT1*, *SYK*, and *TOP1*); Figure 2.

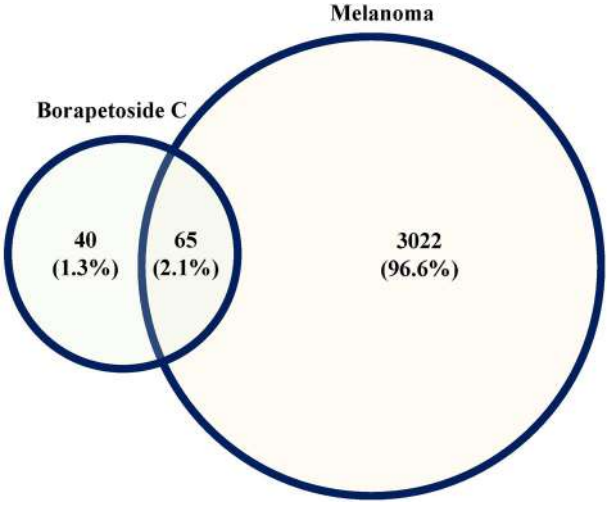

Figure 2. Borapetoside C shares 2.1%, i.e. 65 different targets for melanoma recorded targets concerning DisGeNET (UMLS CUI: C0025202).

3.2. Gene ontology analysis

The protein-protein interaction (PPI) of *65* proteins (nodes) had *306* different interactions (edges) with a *9.42* average node degree, *0.585* average local clustering coefficient, and *97* expected number of edges at enrichment $p < 1.0e\text{-}16$ (Figure 3a). In addition, *CASP3*, *EGFR*, *MMP9*, *MAPK3,* and *MMP2* were identified as major hub genes (Figure 3b). The detailed scores of each protein for average short path length, clustering coefficient, closeness centrality, eccentricity, stress, degree, neighbourhood connectivity, number of directed edges, topological coefficient, Edge count, in degree, and outdegree are summarized in Figure 4.

A total of *47* different cellular components were regulated by the borapetoside C majorly affecting membrane raft (GO: *0045121*) and modulating *13* genes (*MAPK1*, *CTSD*, *MAPK3*, *KDR*, *EGFR*, *ADAM17*, *CASP3*, *CASP8*, *DPP4*, *JAK2*, *OPRM1*, *SLC2A1*, and *MME*) at *1.08* strength and 1.12E-07 false discovery rate. Similarly, 60 different molecular functions were traced in which catalytic activity, acting on a protein (GO:*0140096*) was majorly triggered by *41* genes (*MAPK1*, *AURKA*, *MMP2*, *MAPK14*, *CTSD*, *MMP8*, *SIRT2*, *CDK4*, *MMP13*, *MAPK3*, *KDR*, *CASP6*, *CDK2*, *IGF1R*, *ERBB2*, *REN*, *EGFR*, *BRAF*, *MAP2K1*, *MMP14*, *ADAM17*, *CASP3*, *AURKB*, *MMP1*, *JAK1*, *EPHB4*, *CASP8*, *DPP4*, *PIM3*, *TOP1*, *CASP7*, *MMP9*, *PIM1*, *SYK*, *JAK2*, *ACVRL1*, *CHEK1*, *FGFR1*, *MME*, *CASP1*, and *MAP3K9*) at *0.77* strength and *3.00E-20* false discovery rate. In addition, a total of *601* different biological processes were identified for borapetoside C. Among them, the protein metabolic process (GO:*0019538*) was identified was chiefly modulated by regulating *48* genes (*MAPK1*, *LGALS1*, *AURKA*, *MMP2*, *MAPK14*, *CTSD*, *MMP8*, *SIRT2*, *CDK4*, *MMP13*, *MAPK3*, *KDR*, *CASP6*, *CDK2*, *IGF1R*, *ERBB2*, *REN*, *EGFR*, *BRAF*, *EIF4A1*, *MAP2K1*, *ACHE*, *MMP14*, *ADAM17*, *CASP3*, *AURKB*, *MMP1*, *F3*, *ADORA2A*, *JAK1*, *EPHB4*, *CASP8*, *DPP4*, *PIM3*, *TOP1*, *CASP7*, *MMP9*, *PIM1*, *SYK*, *IGFBP3*, *JAK2*, *ACVRL1*, *LGALS9*, *CHEK1*, *FGFR1*, *MME*, *CASP1*, *MAP3K9*) at *0.53* strength and *7.37E-15* false discovery rate. The top *10* gene ontology terms with their gene count are presented in Figure 5.

3.3. KEGG pathway analysis

A total of *127* KEGG pathways were traced to be regulated by borapetoside C of which *25* were identified for different types of cancer. Among them, 21 genes (*MAPK1*, *MMP2*, *CDK4*, *MAPK3*, *CDK2*, *IGF1R*, *ERBB2*, *EGFR*, *BRAF*, *MAP2K1*, *CASP3*, *MMP1*, *JAK1*, *CASP8*, *CASP7*, *MMP9*, *PIM1*, *JAK2*, *FGFR1*, *SLC2A1*, and *AGTR1*) were modulated in pathways in cancer

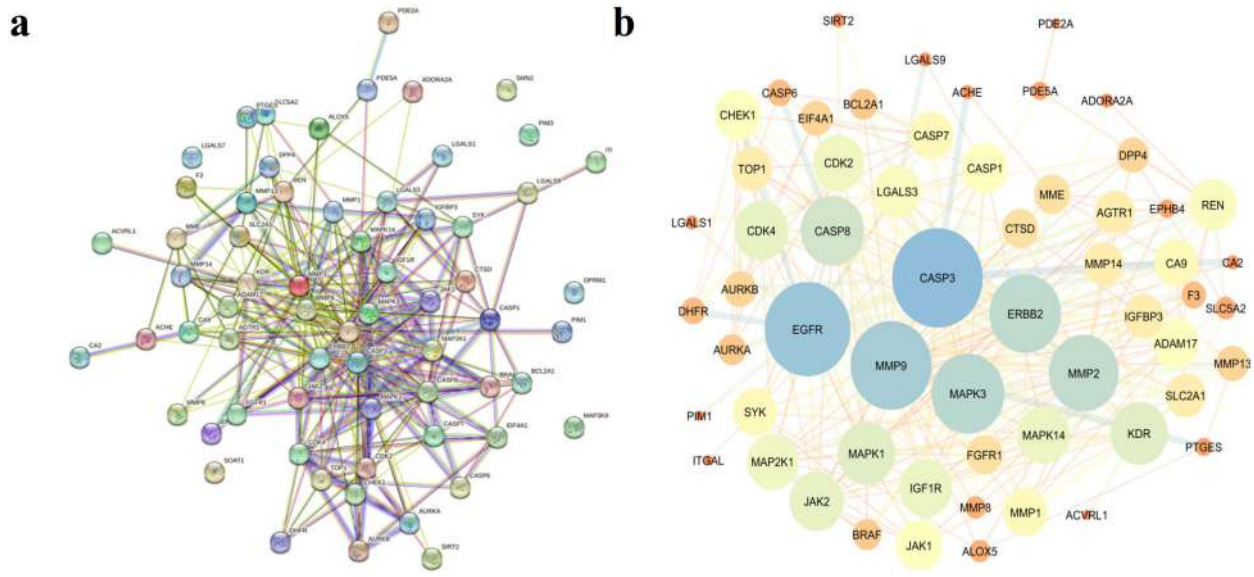

Figure 3. a: Protein-protein interaction (visualized in a: STRING and b: Cytoscape after analysis) of the borapetoside C-triggered protein. Node color; colored nodes: query proteins and first shell of interactors, white nodes: second shell of interactors, node content; empty nodes: proteins of unknown 3D structure, filled nodes: some 3D structure is known or predicted, known interactions; from curated databases, experimentally determined, predicted interactions; gene neighbourhood, gene fusions, gene co-occurrence & others; text mining, co-expression, protein homology.

(*hsa05200*) at *1.09* strength and *7.08E-15* false discovery rate. Further, in melanoma (*hsa05218*) borapetoside C modulated *8* genes (*MAPK1*, *CDK4*, *MAPK3*, *IGF1R*, *EGFR*, *BRAF*, *MAP2K1*, and *FGFR1*) at *1.52* strength and *6.23E-09* false discovery rate. The different diseases and their association with different modulated genes are presented in Figure 6. In the disease-protein-borapetoside C interaction, we observed zero scores for clustering coefficient, self-loops, stress, and betweenness centrality; the interaction of each node is presented in Figure 7, and the score of each node for average short path length, closeness centrality, eccentricity, edge count, in degree, out-degree, and neighborhood connectivity is summarized in Figure 8.

3.4. Active site of macromolecule and molecular docking

Borapetoside C was docked against macromolecule at the following identified active sites i.e. *BRAF* (cavity point= −7.30, −11.29, −29.10, cavity volume = 1226), *CASP3* (cavity point= −5.73, −4.30, 2.78, cavity volume = 619), *EGFR* (cavity point= −9.05, −51.39, 27.54, cavity volume = 1901), *MAP2K1* (cavity point = −14.65, 12.89, 15.15, cavity volume = 1351), *MAPK1* (cavity point= 4.59, −7.43, 12.56, cavity volume = 1314), *MAPK3* (cavity point= −2.21, −1.48, 14.59, cavity volume = 1071), *MMP2* (cavity point= −6.54, 4.23, 2.96, cavity volume = 463), *MMP9* (cavity point= 34.36, 44.38, 24.45, cavity volume = 1911).

Borapetoside C was predicted to have the minimum binding energy of −12.15 kcal/mol with *MAP2K1* with an inhibition constant of 1.25 nM. Borapetoside C was predicted to have *2 H*-bonds in the docked complex with amino acids *Leu54* and *His119* of *MAP2K1*. This was followed by a complex between borapetoside C and *MMP9* with a binding energy of −12.03 kcal/mol by interacting with *Asp185* and *Gly186* and a complex between borapetoside C and *EGFR* having a binding energy of −11.77 kcal/mol interacted with *Met98*. The least affinity was predicted between borapetoside C and *MMP2* with a binding energy of −8.86 kcal/mol and interacted with *Asp26* (Table 1). Further, the borapetoside C interaction with *BRAF*, *CASP3*, *EGFR*, *MAP2K1*, *MAPK1*, *MAPK3*, *MMP2*, and *MMP9* is presented in Figure 9.

3.5. Molecular dynamics simulation

3.5.1. Stability of EGFR-borapetoside C complex

The *EGFR*- borapetoside C complex trajectory demonstrated stable dynamics throughout the *100* ns MD simulation (Figure 10). The average root means square deviation (RMSD) value for the backbone and complex was observed to be ∼*2.5* Å and ∼*3.2* Å, respectively. The complex reached stability after an equilibration period of ∼ *10* ns i.e. from *10* to *100* ns, and the complex RMSD achieved the optimum geometric conformation. The N and C terminal amino acid residues (*Gly1* to *Glu16* and *Arg282* to *Met292*) forming a loop showed maximum fluctuation (∼ *8* Å and ∼ *6.2* Å) respectively, and the residues involved in ligand interaction (*Thr766*, *Cys751*, *Thr830*, *Asp831*, *Leu820*, *Cys773*, *Val702*, *Leu768*, *Leu694*, and *Val704*) showed minimal residual fluctuations up to 2 Å. The radius of gyration (Rg) explains the structural folding and compactness of the molecule. The Rg value revealed stable folding during the simulation by exhibiting a steady decrease in Rg value from *20.5* to *20* Å and showed stable complex formation. Similarly, the solvent-accessible surface area (SASA) was analyzed to distinguish the protein compactness behavior. The initial and final average surface area occupied by *EGFR*-borapetoside C docked complex was *160* nm^2 and *155* nm^2 respectively. The complex formed a compact globular shape as revealed by a

	ASPL	ClCo	ClCe	ECC	S	D	NC	NDE	TC	EC	ID	OD
TOP1	0	0.3	0	0	0	9	19.4	9	0.4	9	9	0
SYK	0	0.2	0	0	0	10	16.7	10	0.3	10	10	0
SLC5A2	0	0.1	0	0	0	4	10.8	4	0.4	4	4	0
SLC2A1	1	0.3	1	1	47	9	22.6	9	0.4	9	8	1
SIRT2	0	0.5	0	0	0	2	26.5	2	0.7	2	2	0
REN	1	0.2	1	1	50	12	14.6	12	0.3	12	11	1
PTGES	0	0.3	0	0	0	3	14.7	3	0.4	3	3	0
PIM1	0	0	0	0	0	1	36	1	0	1	1	0
PDE5A	1.5	0.2	0.7	2	2	3	17.3	3	0.4	3	2	1
PDE2A	2	0	0.5	3	0	1	3	1	0	1	0	1
MMP9	1.3	0.1	0.8	2	113	33	13.5	33	0.2	33	31	2
MMP8	2	0.4	0.5	3	0	4	29.8	4	0.6	4	3	1
MMP2	1.4	0.2	0.7	2	71	26	15.2	26	0.3	26	23	3
MMP14	2.2	0.3	0.5	3	6	9	19	9	0.4	9	8	1
MMP13	1.9	0.3	0.5	3	17	7	19.6	7	0.4	7	4	3
MMP1	1.8	0.4	0.6	3	13	10	23.4	10	0.4	10	7	3
MME	1.7	0.2	0.6	3	9	8	13.6	8	0.3	8	5	3
MAPK3	1.2	0.2	0.8	2	164	28	15	28	0.3	28	20	8
MAPK14	1.5	0.3	0.6	2	69	15	18.5	15	0.3	15	10	5
MAPK1	1.8	0.3	0.6	2	33	18	18.8	18	0.3	18	15	3
MAP2K1	1.6	0.4	0.6	2	16	14	22	14	0.4	14	9	5
LGALS9	0	0.5	0	0	0	2	11.5	2	0.7	2	2	0
LGALS3	1.7	0.2	0.6	3	74	12	18.3	12	0.3	12	7	5
LGALS1	2.5	0.5	0.4	4	0	2	24	2	0.6	2	1	1
KDR	1.5	0.2	0.7	2	86	18	16.7	18	0.3	18	10	8
JAK2	1.8	0.4	0.6	3	20	16	20.4	16	0.4	16	10	6
JAK1	1.7	0.4	0.6	3	4	11	21.5	11	0.4	11	4	7
ITGAL	1	0	1	1	0	1	10	1	0	1	0	1
IGFBP3	1.7	0.4	0.6	3	5	9	24.7	9	0.5	9	5	4
IGF1R	1.5	0.4	0.7	3	9	15	21.4	15	0.4	15	4	11
FGFR1	1.9	0.5	0.5	3	0	8	26	8	0.5	8	3	5
F3	2	0.4	0.5	3	3	5	25	5	0.5	5	1	4
ERBB2	1.3	0.2	0.8	3	163	27	15.4	27	0.3	27	10	17
EPHB4	1.8	0.5	0.5	3	0	3	31.7	3	0.7	3	1	2
EIF4A1	0	0.3	0	0	0	7	15.7	7	0.4	7	7	0
EGFR	1.2	0.1	0.8	2	373	36	12.8	36	0.2	36	12	24
DPP4	1.7	0.3	0.6	3	9	7	19.1	7	0.4	7	1	6
DHFR	2.1	0.4	0.5	3	21	5	17.2	5	0.4	5	3	2
CTSD	1.9	0.4	0.5	3	6	8	25.5	8	0.5	8	2	6
CHEK1	2.1	0.3	0.5	3	48	11	16.5	11	0.3	11	7	4
CDK4	2	0.3	0.5	4	51	16	16.5	16	0.3	16	6	10
CDK2	2.2	0.2	0.5	4	38	14	16.6	14	0.3	14	5	9
CASP8	1.6	0.2	0.6	3	117	22	17	22	0.3	22	5	17
CASP7	1.9	0.3	0.5	3	18	10	20.6	10	0.4	10	2	8
CASP6	2.5	0.4	0.4	4	2	5	16.6	5	0.4	5	2	3
CASP3	1.3	0.1	0.8	2	308	39	12.6	39	0.2	39	7	32
CASP1	1.8	0.3	0.6	3	14	11	19.1	11	0.3	11	1	10
CA9	1.9	0.3	0.5	3	95	10	19.2	10	0.4	10	2	8
CA2	2.8	0.5	0.4	4	0	2	21.5	2	0.6	2	0	2
BRAF	1.9	0.5	0.5	3	0	6	23.2	6	0.5	6	0	6
BCL2A1	2	0.3	0.5	3	0	6	20	6	0.4	6	0	6
AURKB	2	0.3	0.5	3	3	7	17.1	7	0.4	7	1	6
AURKA	1.9	0.4	0.5	3	0	6	20.5	6	0.4	6	0	6
ALOX5	1.6	0.2	0.6	3	0	4	18	4	0.5	4	0	4
AGTR1	1.8	0.4	0.5	3	0	9	24	9	0.4	9	0	9
ADORA2A	1.9	0.5	0.5	3	0	2	20	2	0.6	2	0	2
ADAM17	2.1	0.3	0.5	4	0	11	19.1	11	0.4	11	0	11
ACVRL1	2.4	0	0.4	3	0	1	18	1	0	1	0	1
ACHE	2.2	0	0.5	3	0	2	23.5	2	0.6	2	0	2

Color Scale: Low | Medium | High

Figure 4. Score analysis of each protein for different protein nodes. ASPL: average short path length, *ClCo*: clustering coefficient, *ClCe*: closeness centrality, *ECC*: eccentricity, *S*: stress, *D*: Degree, *NC*: neighbourhood connectivity, *NDE*: Number of directed edges, *TC*: Topological coefficient, *EC*: Edge count, *ID*: in degree, *OD*: Outdegree.

steady decrease in both Rg and SASA values. This complex formed *7* stable *H*-bonds, of which *4* were consistent throughout the simulations. Further, the relative binding affinity between borapetoside C and *EGFR* was investigated using the MMPBSA approach by the g_mmpbsa tool. The estimated relative binding energy was *−66.401* kJ/mol. Further, the estimated van der Waal, electrostatic, polar solvation, and SASA energy was *−135.646*, *−149.381*, *234.865*, and *−66.401* kJ/mol. The residues contributing most to the binding energy were identified by calculating residue decomposition energy. The residues *Ser696*, *Gly697*, *Phe699*, *Gly700*, *Thr701*, *Val702*, and *Ile735* favored the stable

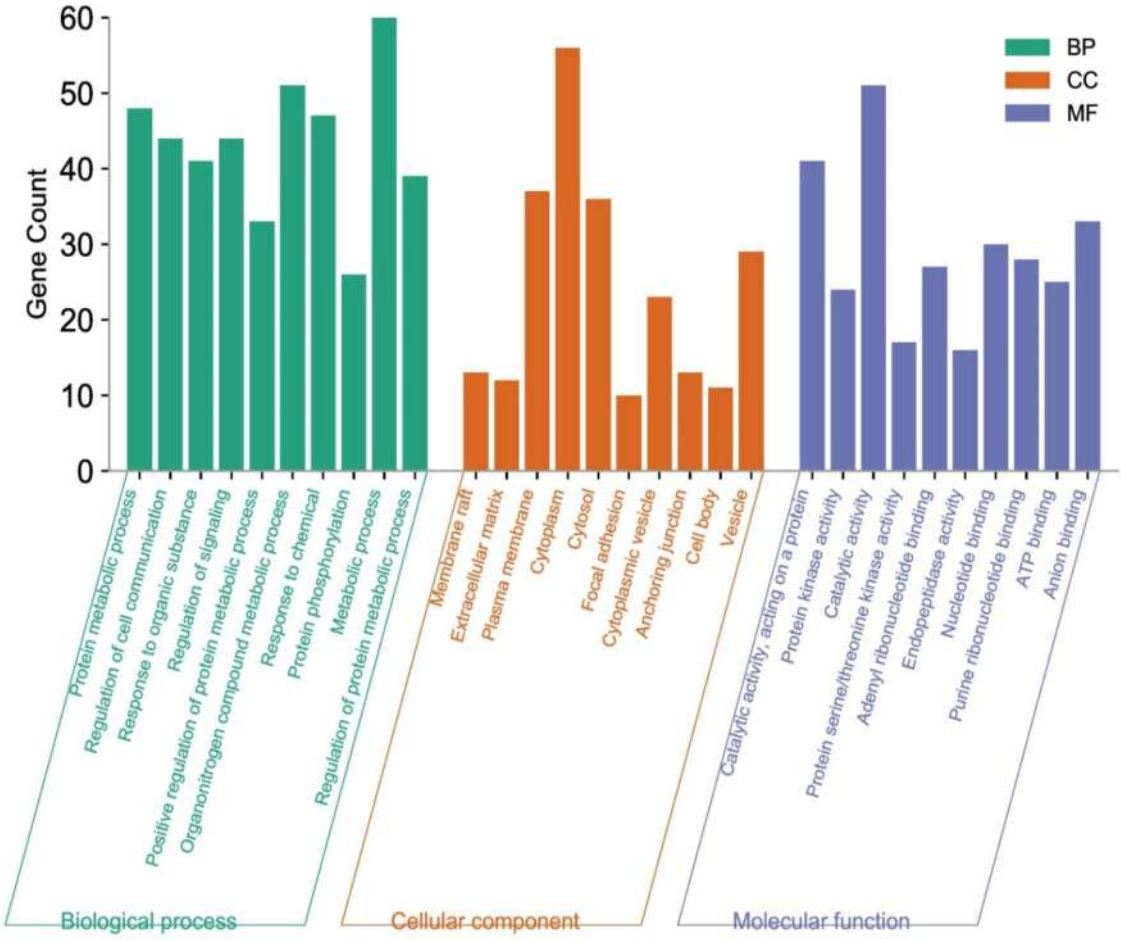

Figure 5. Gene ontology analysis of borapetoside C regulated genes for cellular components, molecular function, and biological process. The gene ontology terms were evaluated at 5% false discovery rate stringency for *Homo sapiens*.

complex formation. However, *Lys721*, *Glu738*, and *Asp831* residues did not favor the interactions. Among these residues, *Val702* showed significant contributions to the binding energy as it had the least contribution energy (−*6.447* kJ/mol). However, other residues also possessed the contribution energy between −*2.581* to −*3.65* kJ/mol and participated in stable complex formation.

3.5.2. Stability of MAP2K1-borapetoside C complex

In the *MAP2K1*-borapetoside C complex, the RMSD of backbone atoms was found to be stable (∼ *9.0* Å) throughout the *100* ns simulation (Figure 11). However, the RMSD of the complex was observed to be stable till *30* ns, and a large fluctuation was observed throughout *100* ns (∼ *16* Å). The N terminal residues showed maximum fluctuation, and the residues involved in ligand interaction (*Gly61*, *Leu63*, *Ala132*, *Lys57*, *His119*, and *Leu54*) showed minimal residual fluctuations up to *2.5* Å. However, the ligand was bound adjacent to the N-terminal residues (the N-terminal residues forming the longest loop possessed higher fluctuation) which allowed the ligand to get escape from the binding pocket. The Rg and SASA explain the structural folding and compactness of the molecule. The Rg value of protein revealed stable folding during the simulation by exhibiting a steady decrease in Rg value from *25* to *23* Å and revealed stable complex formation. Similarly, the solvent-accessible surface area (SASA) was analyzed, and the initial and final average surface area occupied by *MAP2K1*-borapetoside C docked complex was *220* nm^2 and *210* $nm^{2,}$ respectively. From *0* to *10* ns, a sharp decrease in the Rg and SASA indicates an unstable binding of borapetoside C to *MAP2K1*. This complex formed *8 H*-bonds, of which none of the interactions was consistent throughout the simulations. Further, the relative binding affinity between borapetoside C and *MAP2K1* was investigated using the MMPBSA approach by the g_mmpbsa tool. The estimated relative binding energy was 1926.877.401 kJ/mol. Further, the estimated van der Waal, electrostatic, polar solvation, and SASA energy were −*0.002*, *0.122*, *1926.671*, and *0.086* kJ/mol. The positive relative binding energy of the complex is due to the unstable binding mode of borapetoside C with *MAP2K1*. The residues contributing most to the binding energy were identified by calculating residue decomposition energy. All the residues exhibited significant positive energy contribution for opposing the borapetoside C binding to the *MAP2K1*. None of the residues participated in ligand binding and stable complex formation.

3.5.3. Stability of MMP9-borapetoside C complex

In the *MMP9*-borapetoside C complex, a steady increase in the RMSD of backbone and complex was observed till *50* ns (from ∼ *3* to *7.5* Å) and was found to be stable throughout

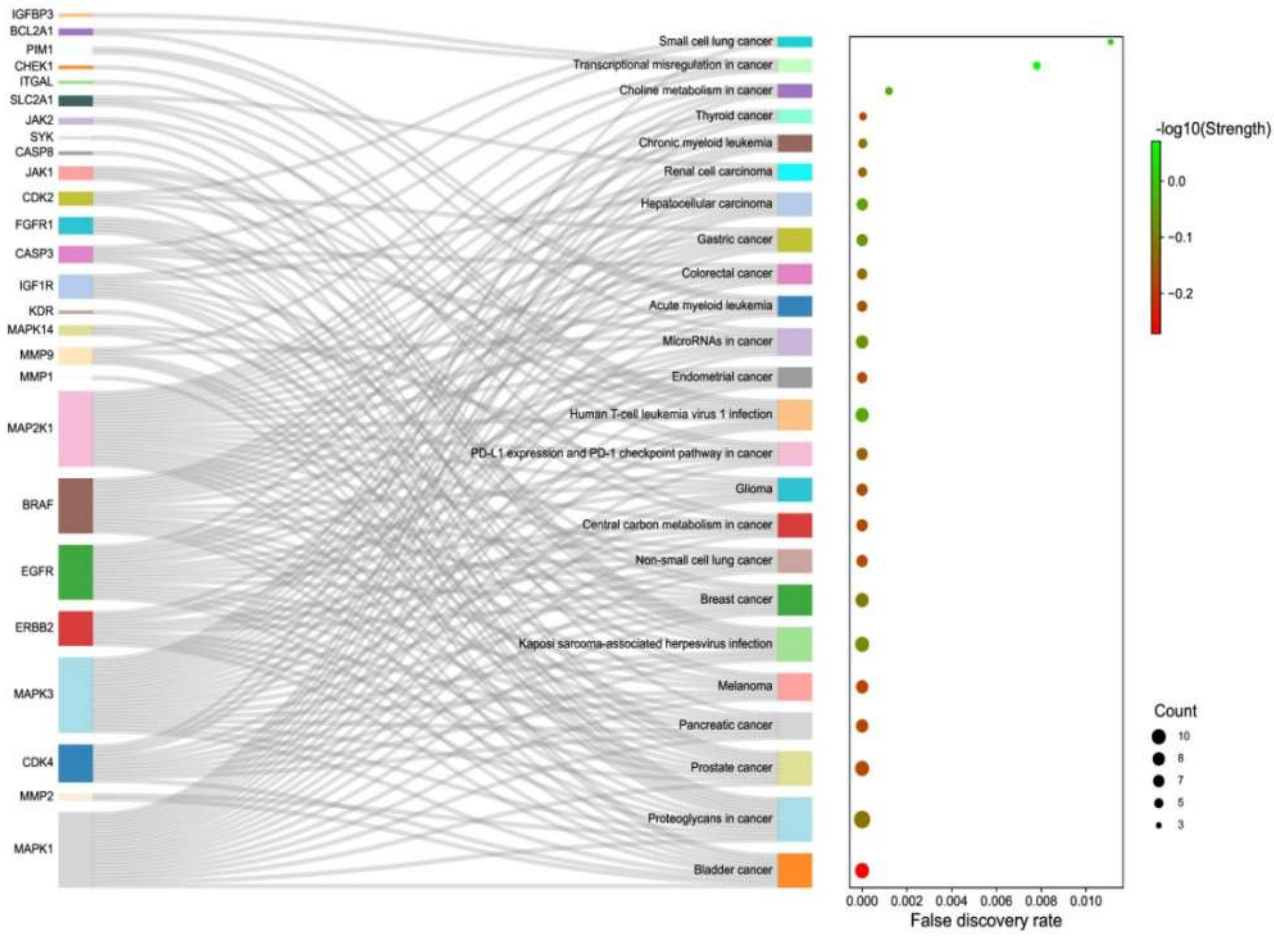

Figure 6. Interaction representation of the disease–gene association. The interaction was evaluated at a 5% false discovery rate stringency for *Homo sapiens* against a whole genome statistical background run.

100 ns with slight fluctuation at *70* ns (Figure 12). The steady increase in the RMSD could be due to the longest loop region (*Arg95* to *His119*) adjacent to the binding pocket showing relatively higher fluctuation compared to ligand binding residues, which allowed ligands to get buried into the binding pocket for stable complex formation. This was confirmed by the steady decrease in the Rg and SASA values. Interestingly, both backbone and complex atoms maintain a similar trend throughout the *100* ns MD simulation, indicating a formation of stable complex formation. The residues involved in ligand interaction (*Tyr48*, *Tyr52*, *Leu39*, *Asp1185*, *Gly186*, *Thr37*, and *Asn38*) showed minimal residual fluctuations up to *3* Å. The residues forming loop '*Ser300* to *Arg312*' showed large fluctuation (∼ *4.0* to *7.5* Å). The Rg and SASA were also found to be stable throughout the *100* ns simulation. The overall Rg value range was between *26* to *25* Å. The initial Rg value was found to be ∼ *26* Å and gradually decreased to *25* Å during simulation. Similarly, the SASA range was within ∼ *230* to *210* nm^2 with an average SASA of ∼ *220* nm^2. The initial SASA value was found to be ∼ *230* nm^2 and gradually decreased to *210* nm^2 during simulation. A stable complex was formed during the MD simulation and established a compact globular shape as revealed by a decrease in the Rg and SASA value. This complex formed *7* stable *H*-bonds, of which *5* were consistent throughout the simulations. Further, the relative binding affinity between borapetoside C and *MMP9* was investigated using the MMPBSA approach by the g_mmpbsa tool. The estimated relative binding energy was −*124.553* kJ/mol. Further, the estimated van der Waal, electrostatic, polar solvation, and SASA energy was −*257.702*, −*109.904*, *267.117*, and −*24.064* kJ/mol. The residues contributing most to the binding energy were identified by calculating residue decomposition energy. The residues *Leu44*, *Glu46*, *Tyr48*, *Ala93*, *Met94*, *Arg95*, and *Met422* favored the stable complex formation. However, *Thr96*, *Lys92*, and *Asp103* residues did not favor the interactions. Among these residues, *Tyr48* showed significant contributions to the binding energy as it had the least contribution energy (−*6.994* kJ/mol). However, other residues also possessed the contribution energy between −*2.23* to −*5.39* kJ/mol and participated in stable complex formation.

3.5.4. Principal component analysis of complexes

The maximum collective motion of the complex was investigated by the first 2 principal components (PC1 and PC2) and captured by the first *50* eigenvectors. It was observed that the borapetoside C-*MAP2K1* complex showed higher conformational flexibility (PC1: −*20* nm to *10* nm and PC2: −*10* nm to *15* nm) and a larger diversity of conformations (eigenvalue: *35* nm^2) during the simulations (indicated in red in Figure 13B1 and B2). Similarly, borapetoside C- *EGFR*

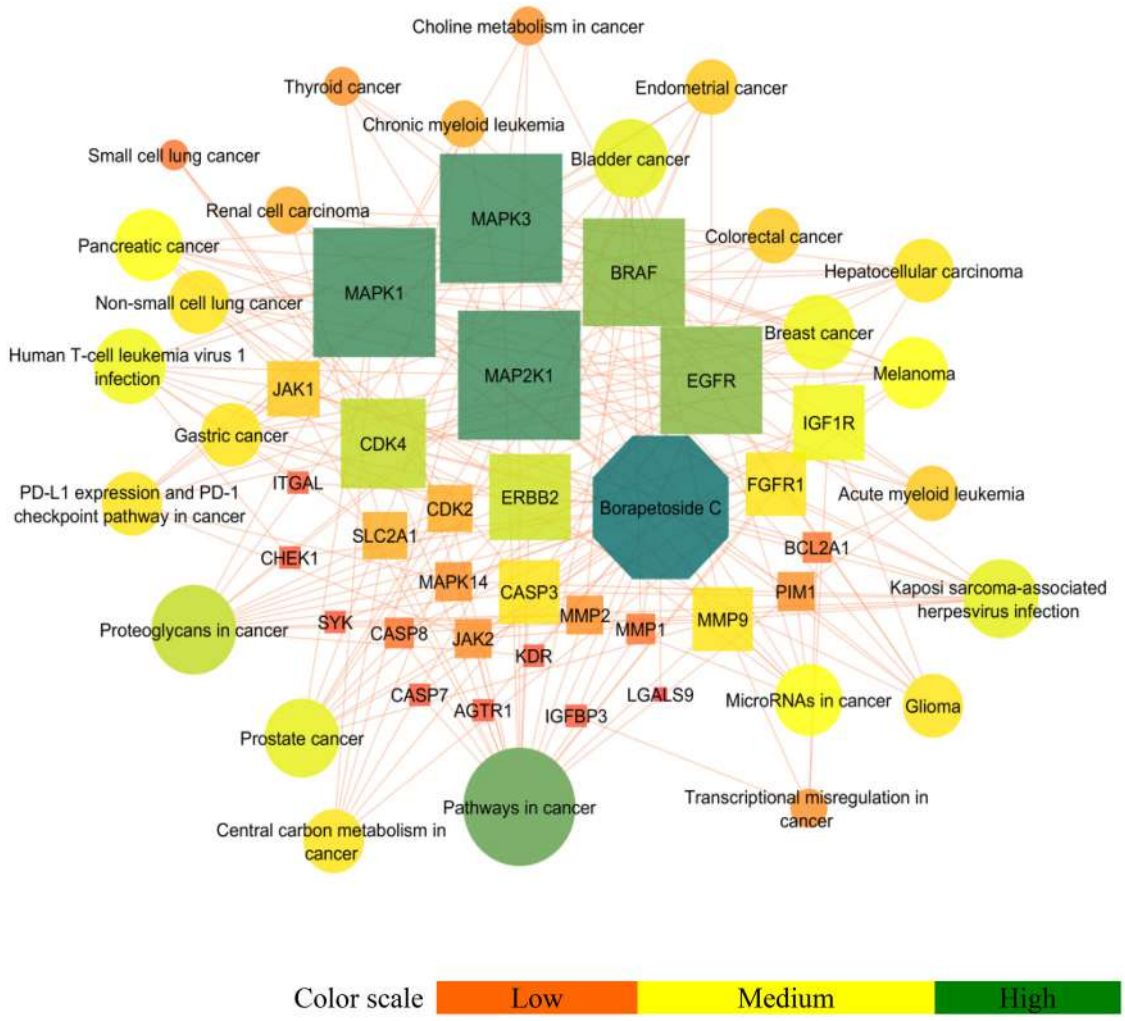

Figure 7. Interaction of borapetoside C-proteins-pathways. *MAPK1*, *MAPK3*, *MAP2K1*, *BRAF*, and *EGFR* were identified as lead hub genes.

complexes showed lower conformational flexibility and (PC1: −*8* nm to *3* nm and PC2: −*6* nm to *4* nm) smaller diversity of conformations (eigenvalue: *4* nm^2) (indicated in black in Figure 13A1 and A2). Likewise, borapetoside C-*MMP9* showed moderate conformational flexibility (PC1: −*13* nm to *15* nm and PC2: −*7* nm to *7* nm) and moderate diversity of conformations (eigenvalue: *37* nm^2) during the simulations (indicated in green in Figure 13C1 and C2).

3.5.5. Dynamic cross-correlation matrix

Structural information on the coordinated motion of ligand-binding domains was gained from the observation of dynamic cross-correlation in complexes and the concerted residual motion in all the simulated complexes is presented in Figure 14. In complex borapetoside C-*EGFR*, the binding site residues show anti-correlation with the N-terminal domain of the *EGFR*. The amplitude of anticorrelation is maximum compared to borapetoside C with *MAP2K1* and *MMP9* complexes. Borapetoside C - *EGFR* complex showed a strong correlation between the residues *700* to *830*. The cooperative motion expressed by the binding pocket residues ranging from *700* to *830* with the N- and C- terminal region revealed the significance of the active site residues in stabilizing the borapetoside C - *EGFR* complex whereas, in the borapetoside C—*MAP2K1* complex, binding pocket correlation was lost. However, in borapetoside C—*MAP2K1* complex, binding pocket residues ranging from *130* to *270* revealed a strong correlation. Thus, we propose binding of borapetoside C with *EGFR* and *MMP9* would favor the conformational transition and promote the stable complex formation with enhanced non-bonded interactions compared to the borapetoside C—*MAP2K1* complex.

4. Discussion

Melanoma is developed in the melanocytes when these pigment-producing cells start proliferating uncontrollably (Rotte & Bhandaru, 2016). It is one of the most dreaded types of skin cancer, with the highest number of cases recorded in Australia in 2020 (https://www.wcrf.org/cancer-trends/skin-cancer-statistics/). The current pharmacotherapy for melanoma involves the use of surgery, radiation, and chemotherapy, including drugs like cisplatin, temozolomide, and dacarbazine (Velho, 2012). *Tinospora* species (mainly *T. crispa*) is the major source of borapetoside C, and also reports suggest polysaccharide fraction *T. cordifolia* to be effective in lowering the metastatic potential of B16F-10 melanoma cells (Sharma *et al.*, 2019; Leyon & Kuttan, 2004). In addition,

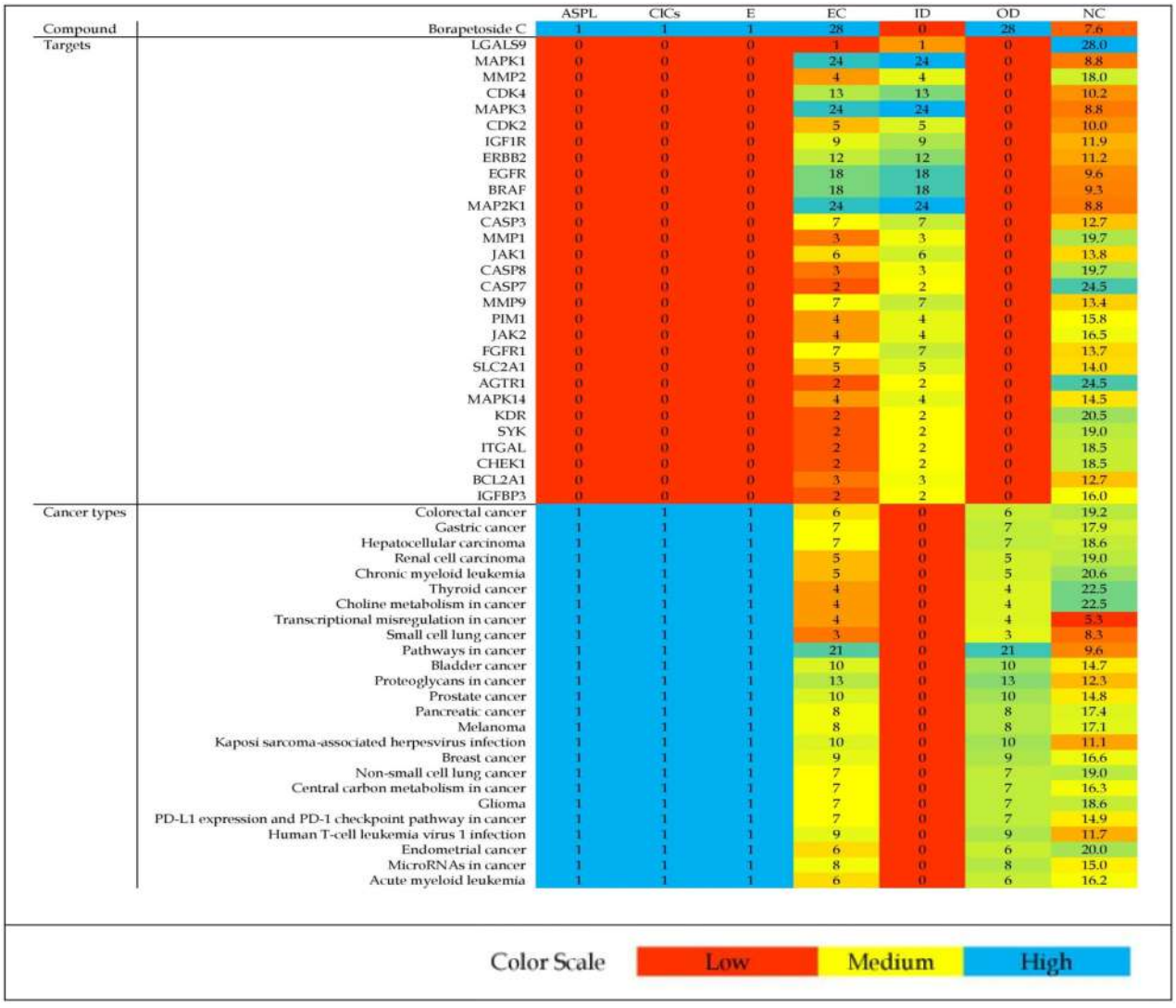

		ASPL	CICs	E	EC	ID	OD	NC
Compound	Borapetoside C	1	1	1	28	0	28	7.6
Targets	LGALS9	0	0	0	1	1	0	28.0
	MAPK1	0	0	0	24	24	0	8.8
	MMP2	0	0	0	4	4	0	18.0
	CDK4	0	0	0	13	13	0	10.2
	MAPK3	0	0	0	24	24	0	8.8
	CDK2	0	0	0	5	5	0	10.0
	IGF1R	0	0	0	9	9	0	11.9
	ERBB2	0	0	0	12	12	0	11.2
	EGFR	0	0	0	18	18	0	9.6
	BRAF	0	0	0	18	18	0	9.3
	MAP2K1	0	0	0	24	24	0	8.8
	CASP3	0	0	0	7	7	0	12.7
	MMP1	0	0	0	3	3	0	19.7
	JAK1	0	0	0	6	6	0	13.8
	CASP8	0	0	0	3	3	0	19.7
	CASP7	0	0	0	2	2	0	24.5
	MMP9	0	0	0	7	7	0	13.4
	PIM1	0	0	0	4	4	0	15.8
	JAK2	0	0	0	4	4	0	16.5
	FGFR1	0	0	0	7	7	0	13.7
	SLC2A1	0	0	0	5	5	0	14.0
	AGTR1	0	0	0	2	2	0	24.5
	MAPK14	0	0	0	4	4	0	14.5
	KDR	0	0	0	2	2	0	20.5
	SYK	0	0	0	2	2	0	19.0
	ITGAL	0	0	0	2	2	0	18.5
	CHEK1	0	0	0	2	2	0	18.5
	BCL2A1	0	0	0	3	3	0	12.7
	IGFBP3	0	0	0	2	2	0	16.0
Cancer types	Colorectal cancer	1	1	1	6	0	6	19.2
	Gastric cancer	1	1	1	7	0	7	17.9
	Hepatocellular carcinoma	1	1	1	7	0	7	18.6
	Renal cell carcinoma	1	1	1	5	0	5	19.0
	Chronic myeloid leukemia	1	1	1	5	0	5	20.6
	Thyroid cancer	1	1	1	4	0	4	22.5
	Choline metabolism in cancer	1	1	1	4	0	4	22.5
	Transcriptional misregulation in cancer	1	1	1	4	0	4	5.3
	Small cell lung cancer	1	1	1	3	0	3	8.3
	Pathways in cancer	1	1	1	21	0	21	9.6
	Bladder cancer	1	1	1	10	0	10	14.7
	Proteoglycans in cancer	1	1	1	13	0	13	12.3
	Prostate cancer	1	1	1	10	0	10	14.8
	Pancreatic cancer	1	1	1	8	0	8	17.4
	Melanoma	1	1	1	8	0	8	17.1
	Kaposi sarcoma-associated herpesvirus infection	1	1	1	10	0	10	11.1
	Breast cancer	1	1	1	9	0	9	16.6
	Non-small cell lung cancer	1	1	1	7	0	7	19.0
	Central carbon metabolism in cancer	1	1	1	7	0	7	16.3
	Glioma	1	1	1	7	0	7	18.6
	PD-L1 expression and PD-1 checkpoint pathway in cancer	1	1	1	7	0	7	14.9
	Human T-cell leukemia virus 1 infection	1	1	1	9	0	9	11.7
	Endometrial cancer	1	1	1	6	0	6	20.0
	MicroRNAs in cancer	1	1	1	8	0	8	15.0
	Acute myeloid leukemia	1	1	1	6	0	6	16.2

Figure 8. Network analysis of the borapetoside C-disease-protein interaction. *ASPL*: Average short path length, *CICs*: Closeness centrality, *E*: Eccentricity, *EC*: Edge count, *ID*: in degree, *OD*: Outdegree, *NC*: Neighborhood connectivity scores of proteins, disease, and borapetoside C nodes.

Table 1. Binding affinity, inhibitory constant, and interaction of borapetoside C with targets.

Protein	RMSD	Binding energy (kcal/mol)	IC (Ki)	No. of *H*- bonds	*H*- bond interactions
BRAF	27.71	−9.99	47.51 nM	3	*Phe468, Gly596, Phe595*
CASP3	15.8	−10.27	29.70 nM	2	*Asn52, Asn54*
EGFR	55.58	−11.77	2.35 nM	1	*Met98*
MAP2K1	19.46	−12.15	1.25 nM	2	*Leu54, His119*
MAPK1	15.26	−11.51	3.64 nM	4	*Ser153, Asp111, Met108, Thr110*
MAPK3	11.43	−10.46	21.51 nM	4	*Thr54, Asp50, Leu53, Phe55*
MMP2	6.9	−8.86	322.17 nM	1	*Asp26*
MMP9	62.63	−12.03	1.51 nM	2	*Asp185, Gly186*

RMSD: Root Mean Square Deviation *IC*: Inhibition constant.

human cancer cell lines HepG2, HL-60 (human promyelocytic leukemia cells), and Hep3B cell lines were suppressed by the methanol extract of *T. crispa* stem and displayed a dose-dependent activity (Ibahim *et al*., 2011; Ahmad *et al*., 2016). Since, borapetosideC is one of the important active bioactive of *T. crispa*, the present study aimed to identify the effect of borapetoside C against melanoma through multiple computationalapporaches like gene ontology enrichment analysis, molecular docking, molecular dynamic simulations, MMPBSA analysis etc.

In the early stage of drug discovery, system biology tools play an evident role in proposing the possible mechanism of test agents against disease (Dwivedi *et al*., 2022; Patil *et al*., 2022a). Similarly, in the present study, we retrieved targets modulated by borapetoside C which were further cross-matched with the melanoma-linked targets to perform enrichment analysis. Further, KEGG pathway analysis was performed to identify hub genes and evident pathways modulated by borapetoside C against melanoma. In addition, molecular docking and simulation studies were performed

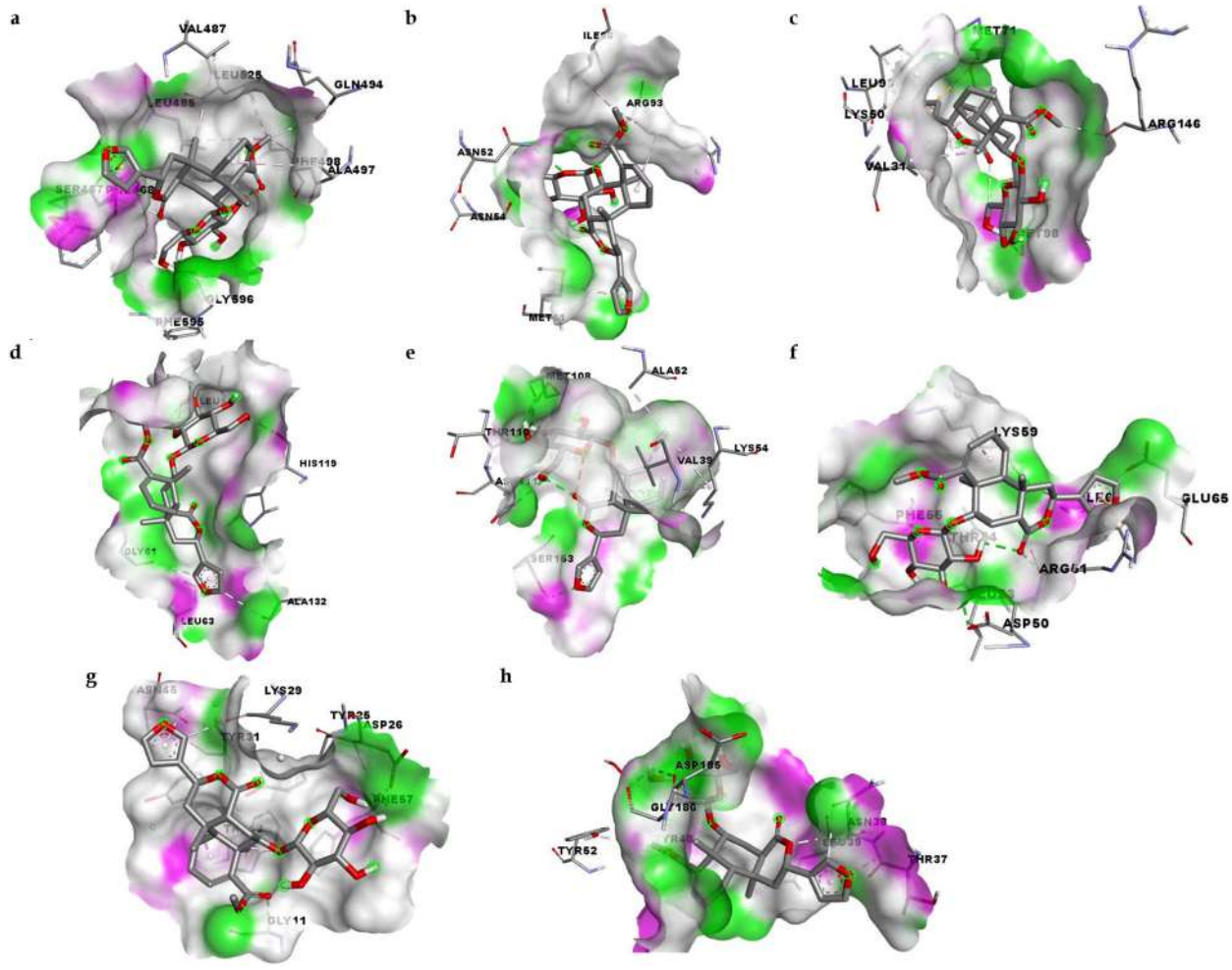

Figure 9. Interaction of borapetoside C with (a) *BRAF*, (b) *CASP3*, (c) *EGFR*, (d) *MAP2K1*, (e) *MAPK1*, (f) *MAPK3*, (g) *MMP2*, and (h) *MMP9*. The green bond presents the *H*- bond interaction between the ligand and the respective protein whereas the other bond represents the hydrophobic interactions. The pink and green shade around the ligand represents the *H*-bond donor and acceptor respectively. A 2D sketch of borapetoside C interaction with the above-mentioned targets is provided in the supplementary figure

on the identified hub genes to retrieve ligand-protein interaction and stability.

Enrichment analysis identified borapetoside C to modulate *65* genes (*61.90*% of total borapetoside C-modulated) in melanoma pathogenesis. Further, the gene ontology analysis predicted *CASP3*, *EGFR*, *MMP9*, and *MAPK3* as major hub genes, and membrane raft (GO: *0045121*) was identified as the lead cellular component; membrane rafts are small (10–*200* nm), heterogeneous, highly dynamic, sterol- and sphingolipid-enriched membrane domains that compartmentalize cellular processes (Pike, 2006). Similarly, catalytic activity, acting on a protein (GO:*0140096*) was predicted as the lead molecular function, and protein metabolic process (GO:*0019538*) as the lead biological process indicates the effect of borapetoside C *via* catalytic activity on proteins at the membrane rafts of the cell. Further, KEGG pathway analysis predicted pathways in cancer (*hsa05200*) to be the major KEGG pathway. Further, the melanoma pathway was identified to be modulated by eight genes (*MAPK1*, *CDK4*, *MAPK3*, *IGF1R*, *EGFR*, *BRAF*, *MAP2K1*, and *FGFR1*).

Molecular docking revealed borapetoside C- dual specificity mitogen-activated protein kinase *1* complex to possess the highest binding affinity. High somatic mutation rates in melanoma are known to exhibit the distinctive features of UV-induced DNA repair (Sample & He, 2018). Recently, it has been discovered that Spitz neoplasms are significantly impacted by structural rearrangements in *MAPK* genes. According to reports, non-canonical *BRAF* mutations in melanomas were associated with gain-of-function mutations in *MAP2K1* and *MAP2K2* (*MEK1* and *MEK2*, respectively), leading to constitutive *ERK* phosphorylation and increased resistance to *MEK* inhibitors. Recurrent somatic *MAP2K1* and *MAP2K2* mutations were found in a larger sample of melanoma patients and occurred at an average frequency of *8*% (Sunshine *et al*., 2020).

The top *3* hub genes were identified through molecular docking were further subjected to molecular dynamics simulations of *100* ns. In the present study, molecular docking revealed the interaction of borapetoside C with the active site residue of *EGFR*, *MAP2K1*, and *MMP9*. During *100* ns MD simulation, borapetoside C was identified to interact stably with the *EGFR* and *MMP9* but not with *MAP2K1*. In the borapetoside C-*EGFR* complex, initially, borapetoside C was predicted to interact with *Thr766*, *Cys751*, *Thr830*, *Asp831*, *Leu820*, *Cys773*, *Val702*, *Leu768*, *Leu694*, and *Val704* residues. However, after MD simulation, the residual contribution energy revealed borapetoside C to interact stably with

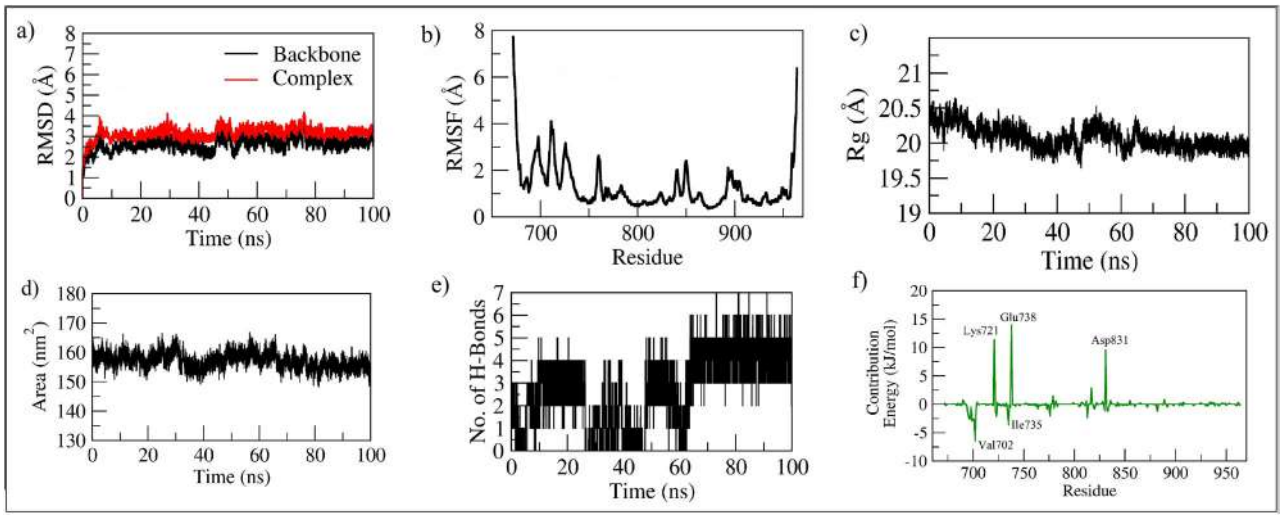

Figure 10. MD simulation of *EGFR* - borapetoside C complex for 100 ns. (a) The RMSD plot of backbone and complex, (b) RMSF plot of C-α, (c) protein Rg plot, (d) protein SASA, (e) number of *H*-bond interactions formed between *EGFR* and borapetoside C, and (f) contribution energy plot highlighting the importance of the binding pocket residues in stable complex formation.

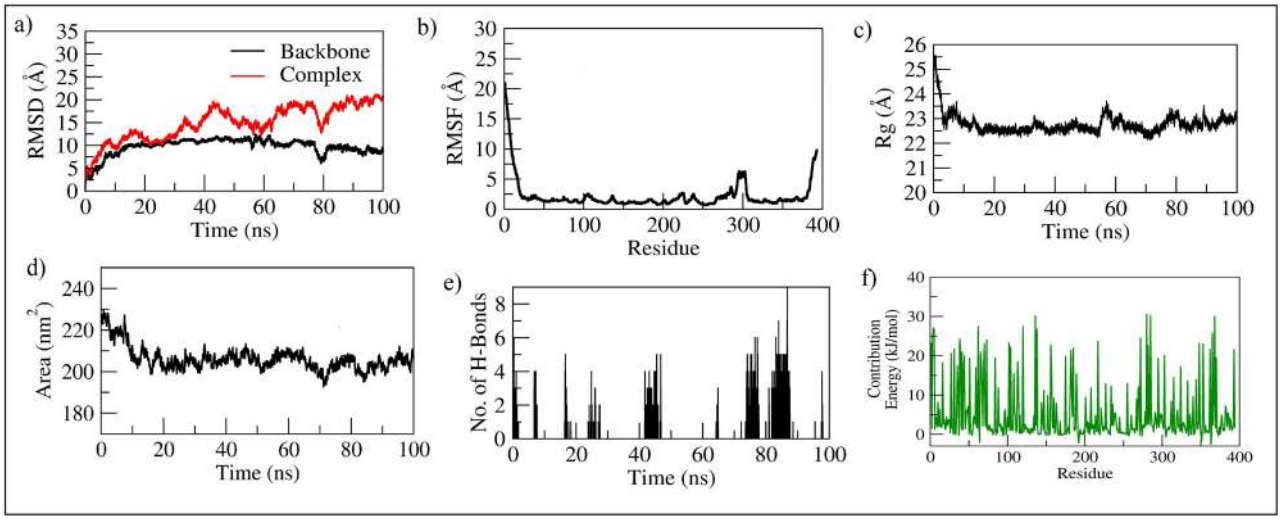

Figure 11. MD simulation of *MAP2K1* - borapetoside C complex for *100* ns. (a) the RMSD plot of backbone and complex, (b) RMSF plot of C-α, (c) protein Rg plot, (d) protein SASA, (e) number of *H*-bond interactions formed between *MAP2K1* and Borapetoside C, and (f) contribution energy plot highlighting the importance of the binding pocket residues in stable complex formation.

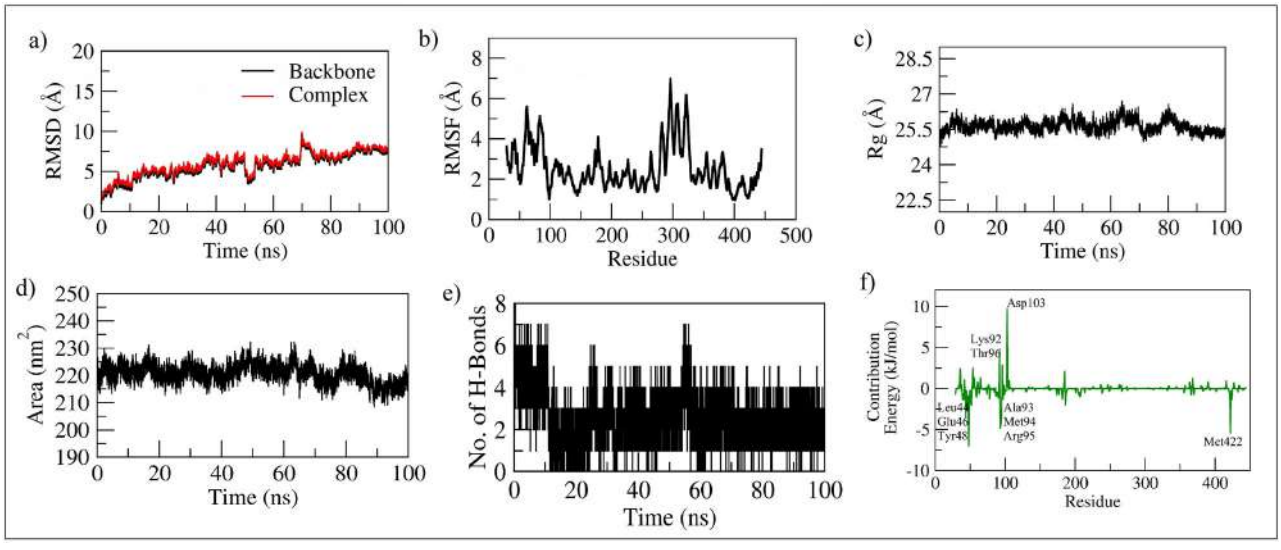

Figure 12. MD simulation of *MMP9* - borapetoside C complex for *100* ns. (a) the RMSD plot of backbone and complex, (b) RMSF plot of C-α, (c) protein Rg plot, (d) protein SASA, (e) number of *H*-bond interactions formed between *MMP9* and Borapetoside C, and (f) contribution energy plot highlighting the importance of the binding pocket residues in stable complex formation.

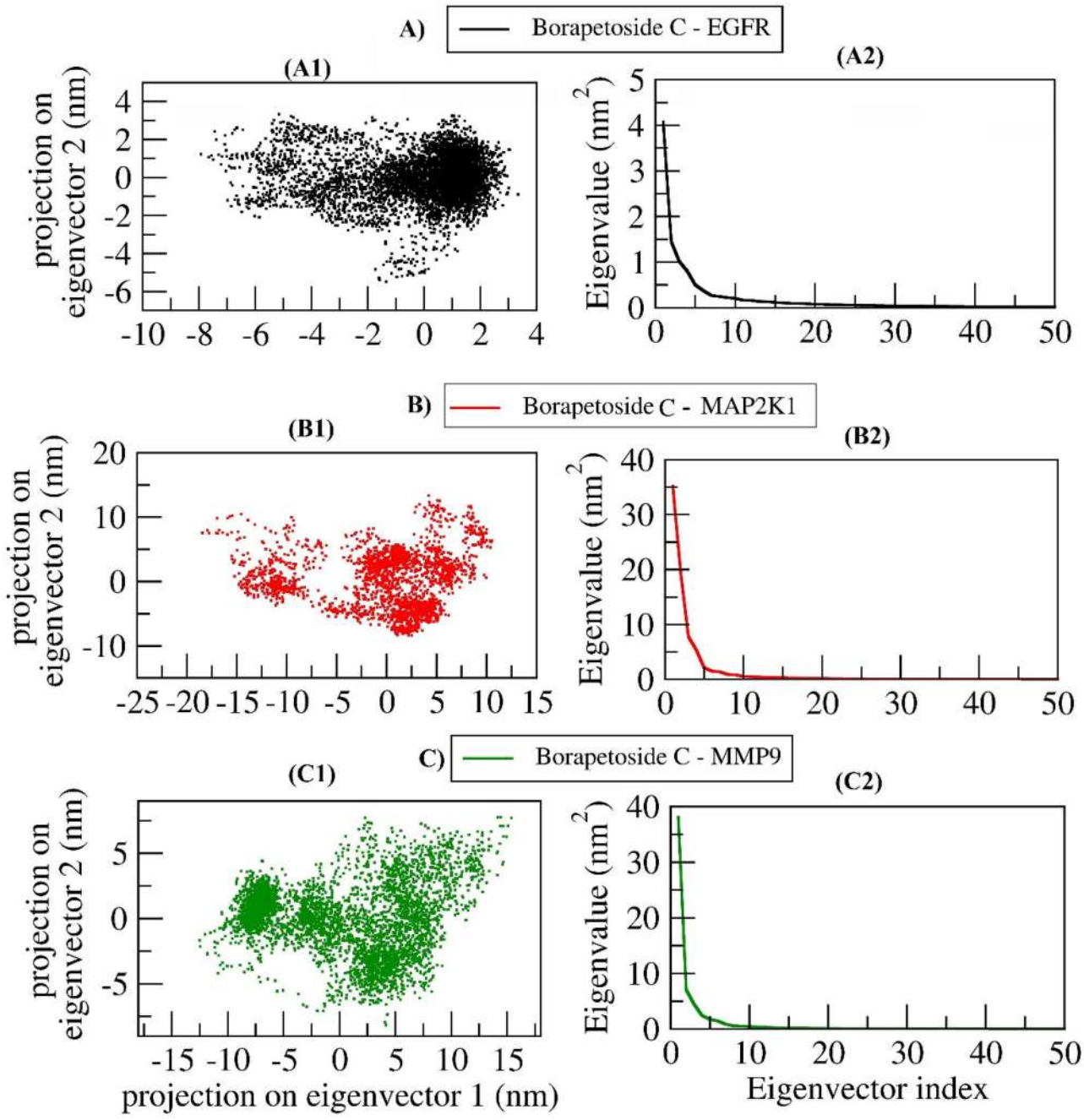

Figure 13. Principal component analysis of complexes of borapetoside C with (A) *EGFR*, (B) *MPA2K1*, and (C) *MMP9*. A1, B1, and C1 represent projections of MD trajectories on two eigenvectors corresponding to the first 2 principal components, respectively and A2, B2, and C2 represent the first *50* eigenvectors plotted versus eigenvalue for A), B), and C) respectively.

Ser696, *Gly697*, *Phe699*, *Gly700*, *Thr701*, *Val702*, and *Ile735*. Among these, *Val702* was found to be a common interactive residue, and interestingly other residues were also found to be within the active site region. Secondly, in the borapetoside C-*MAP2K1* complex, borapetoside C initially formed interaction with *Gly61*, *Leu63*, *Ala132*, *Lys57*, *His119*, and *Leu54,* and during simulation, the trajectory analysis revealed an unstable binding mode of borapetoside C to the active site . Hence, it may not be a suitable lead candidate against *MAP2K1*. Similarly, in the borapetoside C-*MMP9* complex, borapetoside C initially formed interaction with *Tyr48*, *Tyr52*, *Leu39*, *Asp1185*, *Gly186*, *Thr37*, and *Asn38,* and during MD simulation, borapetoside C showed stable contacts with *Leu44*, *Glu46*, *Tyr48*, *Ala93*, *Met94*, *Arg95*, and *Met422*. Among these, *Tyr48* was found to be a common interactive residue and scored the least contribution energy of -6.994 kJ/mol. The MD analysis concludes that borapetoside C is a potent lead hit toward the active residues of *EGFR* and *MMP9*. Additionally, the principal component analysis revealed that the maximum collective motion of the borapetoside C with *EGFR* and *MMP9* complexes and showed lower conformational flexibility with a smaller diversity of conformations compared to *MAP2K1*. Thus, we propose that borapetoside C with *EGFR* and *MMP9* could be more effective.

Further, an examination of the *EGFR* gene expression in melanoma using fluorescence *in situ* hybridization (FISH)

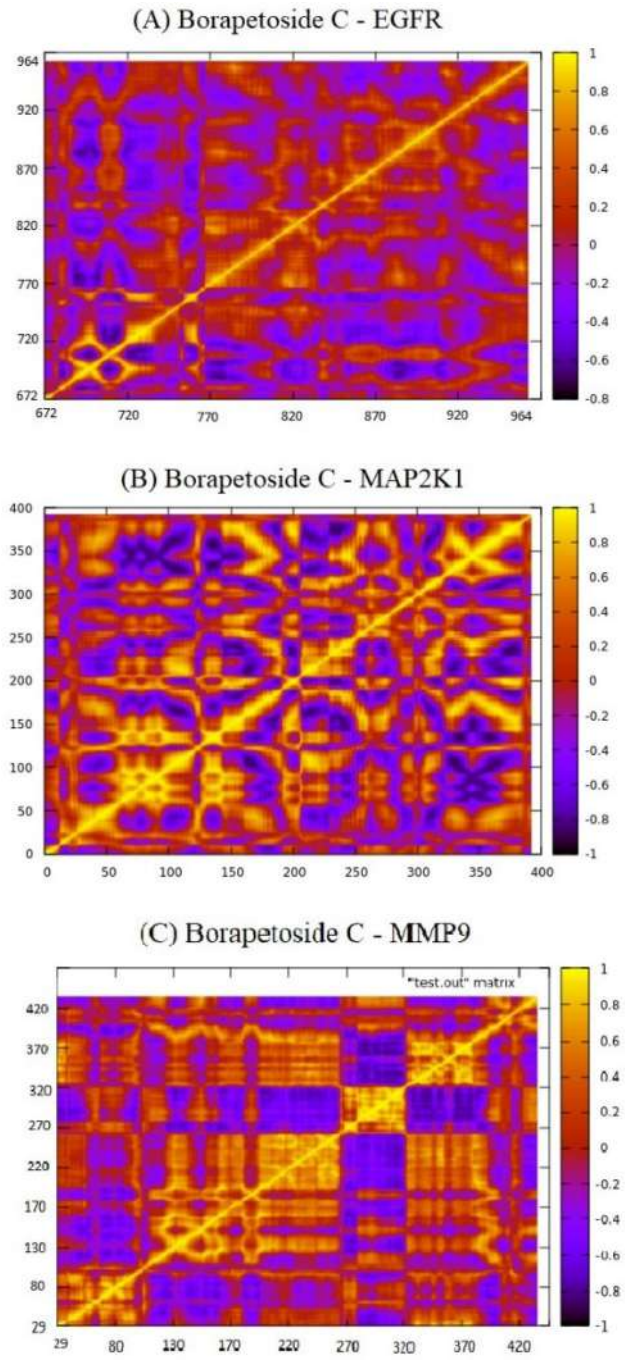

Figure 14. Dynamic cross-correlation matrix of complexes for borapetoside C with A) *EGFR*, B) *MPA2K1*, and C) *MMP9*. The diagonal amber-colored line shows a strong self-correlation of each residue with itself. The amplitude of correlation to anticorrelation is scaled from amber to blue color respectively. Amber color represents strongly correlated motions (*Cij = 1*) and blue color represents anti-correlated motions (*Cij = -1*).

revealed that *EGFR* gene amplification is associated with a worse prognosis and that *EGFR* protein expression is more frequently seen in patients who have a positive sentinel lymph node. Thicker tumors were linked to the presence of *EGFR* polysomy (Sunshine *et al*., 2020; Vidal *et al*., 2020). Additionally, studies have shown that *MEK* inhibitors like trametinib and cobimetinib can help with chemotherapy resistance. Thus, to improve the efficacy of current treatment regimens and combat the formation of acquired resistance, new molecular targets and treatment approaches are required. Such a target might be *EGFR*, which appears to be a key player in the process. Thus, using its inhibitors in anti-melanoma therapy may be advantageous for some melanoma patients (Lim *et al*., 2017; Chen & Davies, 2014; Patil *et al*., 2022b). A type of peptidase known as matrix metalloproteinases (*MMP*s) can alter the extracellular matrix by encouraging tumor-invasive activities. *MMP9* is the peptidase that contributes the most to the growth of cancer, including melanoma. Abnormal overexpression of *MMP9* can be brought on by dysfunctions in the PI3K/Akt and *MAPK* signaling pathways. Non-coding RNAs and other proteins, such as osteopontin and tissue inhibitors of metalloproteinases, that activate or inhibit *MMP9* are also linked to the abnormal synthesis of the *MMP9* (Niland *et al*., 2022).

5. Conclusions

The current study utilized a series of computational pharmacology tools to evaluate borapetoside C as an anti-melanoma agent. Network pharmacology and KEGG pathway analysis identified *8* hub genes to be modulated with borapetoside C treatment. Further molecular docking of these genes with borapetoside C suggested *MAP2K1*to possess the highest binding affinity followed by *MMP9* and *EGFR*. The stability of all the 3 complexes was further evaluated using molecular dynamics simulations. Further, borapetoside C-*MMP9* and borapetoside C-*EGFR* complexes were found to be stable, suggesting *MMP9* and *EGFR* as probable targets for borapetoside C to combat against melanoma. In addition, the present study is solely based on the computational approach and hence, these findings need to be further validated with suitable wet-lab experiments.

Acknowledgement

The graphical abstract provided in this draft was drawn using BioRender: Scientific Image and Illustration Software (https://www.biorender.com/).

Disclosure statement

All the authors of this research declare that they do not have any conflict of interest in any financial or non-financial means to declare.

Funding

The author(s) reported there is no funding associated with the work featured in this article.

ORCID

Kunal Bhattacharya http://orcid.org/0000-0002-5546-1504
Pukar Khanal http://orcid.org/0000-0002-8187-2120

Authors' contributions

KB, PK: Conceptualization, Experimentation, Methodology, Draft, Edit, Review, Finalize, Supervision. VSP: Experimentation, Methodology, Draft, Edit, Review, Revise, Finalize. PSRD, NRC, RKC, SD, AC: Review, Draft. All authors have read and approved the presented version of the research.

References

Ahmad, W., Jantan, I., & Bukhari, S. N. (2016). *Tinospora crispa* (L.) Hook. f. & Thomson: A review of its ethnobotanical, phytochemical, and pharmacological aspects. *Frontiers in Pharmacology*, *7*, 59. https://doi.org/10.3389/fphar.2016.00059

Amadei, A., Linssen, A. B., & Berendsen, H. J. (1993). Essential dynamics of proteins. *Proteins*, *17*(4), 412–425. https://doi.org/10.1002/prot.340170408

Amadei, A., Linssen, A. B., de Groot, B. L., van Aalten, D. M., & Berendsen, H. J. (1996). An efficient method for sampling the essential subspace of proteins. *Journal of Biomolecular Structure & Dynamics*, *13*(4), 615–625. https://doi.org/10.1080/07391102.1996.10508874

Bhandare, V. V., & Ramaswamy, A. (2018). The proteinopathy of D169G and K263E mutants at the RNA Recognition Motif (RRM) domain of Tar DNA-binding protein (Tdp43) causing neurological disorders: A computational study. *Journal of Biomolecular Structure & Dynamics*, *36*(4), 1075–1093. https://doi.org/10.1080/07391102.2017.1310670

Bhandare, V. V., Kumbhar, B. V., & Kunwar, A. (2019). Differential binding affinity of tau repeat region R2 with neuronal-specific β-tubulin isotypes. *Scientific Reports*, *9*(1), 10795. https://doi.org/10.1038/s41598-019-47249-7

Bhattacharya, K., Bordoloi, R., Chanu, N. R., Kalita, R., Sahariah, B. J., & Bhattacharjee, A. (2022). In silico discovery of 3 novel quercetin derivatives against papain-like protease, spike protein, and 3C-like protease of SARS-CoV-2. *Journal of Genetic Engineering and Biotechnology*, *20*(1), 43. https://doi.org/10.1186/s43141-022-00314-7

Castillo, A. L., Osi, M. O., Ramos, J. D. A., De Francia, J. L., Dujunco, M. U., & Quilala, P. F. (2013). Efficacy and safety of tinospora cordifolia lotion in sarcoptes scabiei var hominis-infected pediatric patients: A single blind, randomized controlled trial. *Journal of Pharmacology & Pharmacotherapeutics*, *4*(1), 39–46. https://doi.org/10.4103/0976-500X.107668

Chen, G., & Davies, M. A. (2014). Targeted therapy resistance mechanisms and therapeutic implications in melanoma. *Hematology/Oncology Clinics of North America*, *28*(3), 523–536. https://doi.org/10.1016/j.hoc.2014.03.001

Daina, A., Michielin, O., & Zoete, V. (2017). SwissADME: A free web tool to evaluate pharmacokinetics, drug-likeness and medicinal chemistry friendliness of small molecules. *Scientific Reports*, *7*(1), 42717. https://doi.org/10.1038/srep42717

Dwivedi, P. S. R., Patil, R., Khanal, P., Gurav, N. S., Murade, V. D., Hase, D. P., Kalaskar, M. G., Ayyanar, M., Chikhale, R. V., & Gurav, S. S. (2021). Exploring the therapeutic mechanisms of *Cassia glauca* in diabetes mellitus through network pharmacology, molecular docking and molecular dynamics. *RSC Advances*, *11*(62), 39362–39375. https://doi.org/10.1039/d1ra07661b

Dwivedi, P. S. R., Patil, V. S., Khanal, P., Bhandare, V. V., Gurav, S., Harish, D. R., Patil, B. M., & Roy, S. (2022). System biology-based investigation of silymarin to trace hepatoprotective effect. *Computers in Biology and Medicine*, *142*, 105223. https://doi.org/10.1016/j.compbiomed.2022.105223

Gajula, R. P., & Gaddameedhi, S. (2015). Commentary: Chemiexcitation of melanin derivatives induces DNA photoproducts long after UV exposure. *Frontiers in Physiology*, *6*(347), 842–848. https://doi.org/10.3389/fphys.2015.00276

Gfeller, D., Grosdidier, A., Wirth, M., Daina, A., Michielin, O., & Zoete, V. (2014). SwissTargetPrediction: A web server for target prediction of bioactive small molecules. *Nucleic Acids Research*, *42*(W1), W32–W38. https://doi.org/10.1093/nar/gku293

Gray-Schopfer, V., Wellbrock, C., & Marais, R. (2007). Melanoma biology and new targeted therapy. *Nature*, *445*(7130), 851–857. https://doi.org/10.1038/nature05661

Hossen, F., Ahasan, R., Haque, M. R., Begum, B., & Hasan, C. M. (2016). Crispene A, B, C and D, four new clerodane type furanoid diterpenes from *Tinospora crispa* (L.). *Pharmacognosy Magazine*, *12*(Suppl 1), S37–S41. https://doi.org/10.4103/0973-1296.176116

Ibahim, M. J., Wan-Nor, I. W. M. Z., Narimah, A. H. H., Nurul, A. Z., Siti-Nur, S. S. A. R., & Froemming, G. A. (2011). Anti-proliperative and antioxidant effects of *Tinospora crispa* (Batawali). *Biomed. Res*, *22*(1), 57–62.

Ivanov, S. M., Lagunin, A. A., Rudik, A. V., Filimonov, D. A., & Poroikov, V. V. (2018). ADVERPred–Web service for prediction of adverse effects of drugs. *Journal of Chemical Information and Modeling*, *58*(1), 8–11. https://doi.org/10.1021/acs.jcim.7b00568

Khanal, P., Zargari, F., Far, B. F., Kumar, D., R, M., Mahdi, Y. K., Jubair, N. K., Saraf, S. K., Bansal, P., Singh, R., Selvaraja, M., & Dey, Y. N. (2021). Integration of system biology tools to investigate huperzine A as an anti-Alzheimer agent. *Frontiers in Pharmacology*, *12*, 785964. https://doi.org/10.3389/fphar.2021.785964

Khanal, P., Patil, V. S., Bhandare, V. V., Patil, P. P., Patil, B. M., Dwivedi, P. S. R., Bhattacharya, K., Harish, D. R., & Roy, S. (2022). Systems and *in vitro* pharmacology profiling of diosgenin against breast cancer. *Frontiers in Pharmacology*, *13*, 1052849. https://doi.org/10.3389/fphar.2022.1052849

Kumari, R., Kumar, R., & Lynn, A. (2014). G-Mmpbsa -A GROMACS tool for high-throughput MM-PBSA calculations. *Journal of Chemical Information and Modeling*, *54*(7), 1951–1962. https://doi.org/10.1021/ci500020m

Lagunin, A., Ivanov, S., Rudik, A., Filimonov, D., & Poroikov, V. (2013). DIGEP-Pred: Web service for in silico prediction of drug-induced gene expression profiles based on structural formula. *Bioinformatics (Oxford, England)*, *29*(16), 2062–2063. https://doi.org/10.1093/bioinformatics/btt322

Leyon, P. V., & Kuttan, G. (2004). Inhibitory effect of a polysaccharide from *Tinospora cordifolia* on experimental metastasis. *Journal of Ethnopharmacology*, *90*(2-3), 233–237. https://doi.org/10.1016/j.jep.2003.09.046

Lim, S. Y., Menzies, A. M., & Rizos, H. (2017). Mechanisms and strategies to overcome resistance to molecularly targeted therapy for melanoma. *Cancer*, *123*(S11), 2118–2129. https://doi.org/10.1002/cncr.30435

Mitra, D., Luo, X., Morgan, A., Wang, J., Hoang, M. P., Lo, J., Guerrero, C. R., Lennerz, J. K., Mihm, M. C., Wargo, J. A., Robinson, K. C., Devi, S. P., Vanover, J. C., D'Orazio, J. A., McMahon, M., Bosenberg, M. W., Haigis, K. M., Haber, D. A., Wang, Y., & Fisher, D. E. (2012). An Ultraviolet-radiation-independent pathway to melanoma carcinogenesis in the red hair/fair skin background. *Nature*, 2012, *491*(7424), 449–453. https://doi.org/10.1038/nature11624

Moharana, M., Pattanayak, S. K., & Khan, F. (2022). Bioactive compounds from Pandanous fascicularis as potential therapeutic candidate to tackle hepatitis a inhibition: Docking and molecular dynamics simulation study. *Journal of Biomolecular Structure and Dynamics*, 1–17. https://doi.org/10.1080/07391102.2022.2158940

Morgan, A. M., Lo, J., & Fisher, D. E. (2013). How does pheomelanin synthesis contribute to melanomagenesis?: Two distinct mechanisms could explain the carcinogenicity of pheomelanin synthesis. *BioEssays: News and Reviews in Molecular, Cellular and Developmental Biology*, *35*(8), 672–676. https://doi.org/10.1002/bies.201300020

Morris, G. M., Ruth, H., Lindstrom, W., Sanner, M. F., Belew, R. K., Goodsell, D. S., & Olson, A. J. (2009). Software News and Updates AutoDock4 and AutoDockTools4: Automated Docking with Selective Receptor Flexibility. *Journal of Computational Chemistry*, *30*(16), 2785–2791. https://doi.org/10.1002/jcc.21256

Niland, S., Riscanevo, A. X., & Eble, J. A. (2022). Matrix Metalloproteinases Shape the Tumor Microenvironment in Cancer Progression. *International Journal of Molecular Sciences*. *23*(1), 146. https://doi.org/10.3390/ijms23010146

Patil, A., Dwivedi, P. S. R., Gaonkar, S. N., Kumbhar, V., Shankar, M. V., Khanal, P., & Patil, B. M. (2022a). GLUT-2 mediated glucose uptake analysis of *Duranta repens*: *In-silico* and *In-vitro* approach. *Journal of Diabetes and Metabolic Disorders*, *21*(1), 419–427. https://doi.org/10.1007/s40200-022-00988-3

Patil, V. S., Harish, D. R., Vetrivel, U., Deshpande, S. H., Khanal, P., Hegde, H. V., Roy, S., & Jalalpure, S. S. (2022b). Pharmacoinformatics analysis reveals flavonoids and diterpenoids from *Andrographis paniculata* and *Thespesia populnea* to target hepatocellular carcinoma induced by hepatitis B virus. *Applied Sciences*, *12*(21), 10691. https://doi.org/10.3390/app122110691

Pike, L. J. (2006). Rafts Defined: A Report on the Keystone Symposium on Lipid Rafts and Cell Function. *Journal of Lipid Research*, *47*(7), 1597–1598. https://doi.org/10.1194/jlr.E600002-JLR200

Piñero, J., Bravo, Á., Queralt-Rosinach, N., Gutiérrez-Sacristán, A., Deu-Pons, J., Centeno, E., García-García, J., Sanz, F., & Furlong, L. I. (2017). DisGeNET: A Comprehensive Platform Integrating Information on Human Disease-Associated Genes and Variants. *Nucleic Acids Research*, *45*(D1), D833–D839. https://doi.org/10.1093/nar/gkw943

Phienwej, H., Swasdichira, I. S., Amnuoypol, S., Pavasant, P., & Sumrejkanchanakij, P. (2015). *Tinospora crispa* extract inhibits MMP-13 and migration of head and neck squamous cell carcinoma cell lines. *Asian Pacific Journal of Tropical Biomedicine*, *5*(9), 738–743. https://doi.org/10.1016/j.apjtb.2015.07.001

Robles-Espinoza, C. D., Roberts, N. D., Chen, S., Leacy, F. P., Alexandrov, L. B., Pornputtapong, N., Halaban, R., Krauthammer, M., Cui, R., Timothy Bishop, D., & Adams, D. J. (2016). Germline MC1R Status Influences Somatic Mutation Burden in Melanoma. *Nature Communications*, 2016, *7*(1), 1–7. https://doi.org/10.1038/ncomms12064

Rotte, A., & Bhandaru, M. (2016). *Immunotherapy of Melanoma: Towards Clinical Application*. ISBN 9783319480657, https://doi.org/10.1007/978-3-319-48066-4_1

Ruan, C. T., Lam, S. H., Chi, T. C., Lee, S. S., & Su, M. J. (2012). Borapetoside C from Tinospora crispa improves insulin sensitivity in diabetic mice. *Phytomedicine : International Journal of Phytotherapy and Phytopharmacology*, *19*(8-9), 719–724. https://doi.org/10.1016/j.phymed.2012.03.009

Salve, B., Tripathi, R., Petare, A., Raut, A., & Rege, N. (2015). Effect of Tinospora Cordifolia on Physical and Cardiovascular Performance Induced by Physical Stress in Healthy Human Volunteers. *AYU (an Int. Q. J. Res. Ayurveda)*, *36*(3), 265–270. https://doi.org/10.4103/0974-8520.182751

Sample, A., & He, Y. Y. (2018). Mechanisms and Prevention of UV-Induced Melanoma. *Photodermatology, Photoimmunology & Photomedicine*, *34*(1), 13–24. https://doi.org/10.1111/phpp.12329

Seiberg, M. (2001). Keratinocyte-Melanocyte Interactions during Melanosome Transfer. *Pigment Cell Research*, *14*(4), 236–242. https://doi.org/10.1034/j.1600-0749.2001.140402.x

Shannon, P., Markiel, A., Ozier, O., Baliga, N. S., Wang, J. T., Ramage, D., Amin, N., Schwikowski, B., & Ideker, T. (2003). Cytoscape: A Software Environment for Integrated Models. *Genome Research*, *13*(11), 2498–2504. https://doi.org/10.1101/gr.1239303.metabolite

Sharma, P., Dwivedee, B. P., Bisht, D., Dash, A. K., & Kumar, D. (2019). The Chemical Constituents and Diverse Pharmacological Importance of Tinospora Cordifolia. *Heliyon*, *5*(9), e02437. https://doi.org/10.1016/j.heliyon.2019.e02437

Sinnya, S., & De'Ambrosis, B. (2013). Stress and Melanoma: Increasing the Evidence towards a Causal Basis. *Archives of Dermatological Research*, *305*(9), 851–856. https://doi.org/10.1007/s00403-013-1373-2

Snel, B., Lehmann, G., Bork, P., & Huynen, M. A. (2000). String: A Web-Server to Retrieve and Display the Repeatedly Occurring Neighbourhood of a Gene. *Nucleic Acids Research*, *28*(18), 3442–3444. https://doi.org/10.1093/nar/28.18.3442

Sunshine, J. C., Kim, D., Zhang, B., Compres, E. V., Khan, A. U., Busam, K. J., & Gerami, P. (2020). Melanocytic Neoplasms With MAP2K1 in Frame Deletions and Spitz Morphology. *The American Journal of Dermatopathology*, *42*(12), 923–931. https://doi.org/10.1097/DAD.0000000000001795

Van Der Spoel, D., Lindahl, E., Hess, B., Groenhof, G., Mark, A. E., & Berendsen, H. J. C. (2005). GROMACS: Fast, Flexible, and Free. *Journal of Computational Chemistry*, *26*(16), 1701–1718. https://doi.org/10.1002/jcc.20291

Velho, T. R. (2012). Metastatic Melanoma - A Review of Current and Future Drugs. *Drugs in Context*, *2012*, 212242. https://doi.org/10.7573/dic.212242

Vidal, L., Tsao, M. S., Pond, G. R., Cohen, E. E. W., Cohen, R. B., Chen, E. X., Agulnik, M., Hotte, S., Winquist, E., Laurie, S., Hayes, D. N., Ho, J., Dancey, J., & Siu, L. L. (2009). Fluorescence in Situ Hybridization Gene Amplification Analysis of EGFR and HER2 in Patients with Malignant Salivary Gland Tumors Treated with Lapatinib. *Head & Neck*, *31*(8), 1006–1012. https://doi.org/10.1002/hed.21052

Williams, P. F., Olsen, C. M., Hayward, N. K., & Whiteman, D. C. (2011). Melanocortin 1 Receptor and Risk of Cutaneous Melanoma: A Meta-Analysis and Estimates of Population Burden. *International Journal of Cancer*, *129*(7), 1730–1740. https://doi.org/10.1002/ijc.25804

Zulkhairi, A., Jr., Abdah, M. A., M Kamal, N. H., Nursakinah, I., Moklas, M. A., Hasnah, B., Fazali, F., Khairunnur, F. A., Kamilah, K. A., Zamree, M. S., & Shahidan, M. M. (2008). Biological Properties of *Tinospora crispa* (Akar Patawali) and Its Antiproliferative Activities on Selected Human Cancer Cell Lines. *Malays J Nutr*, *14*(2), 173–187.